UNIVERSITY OF CALIFORNIA
RIVERSIDE

Elucidating the Mechanisms of TFAM in Mitochondrial DNA Maintenance: Studies Towards Understanding its Molecular Functions

A Dissertation submitted in partial satisfaction
of the requirements for the degree of

Doctor of Philosophy

in

Chemistry

by

Wenxin Zhao

September 2024

Dissertation Committee:
Dr. Linlin Zhao, Chairperson
Dr. Chia-En Chang
Dr. Joey Genereux

The Dissertation of Wenxin Zhao is approved:

_____

_____

_____

Committee Chairperson

University of California, Riverside

ACKNOWLEDGEMENTS

I am deeply grateful to everyone who played a pivotal role in the completion of my dissertation. My utmost thanks go to my graduate advisor, Dr. Linlin Zhao, whose guidance and mentorship were invaluable throughout my research journey. Dr. Zhao's deep expertise, constant encouragement, and dedication to scientific excellence have profoundly influenced and inspired me.

I would also like to thank my dissertation committee members, Dr. Joey Genereux and Dr. Chia-En Chang, for their insightful feedback and constructive criticism, which have significantly enhanced my work.

A special thank you goes to the postdoctoral fellows in our lab, particularly former postdoctoral fellow Dr. Wenyan Xu, for his expertise and collaborative spirit, Dr. Anal Jana, whose insights into organic chemistry were crucial, and Dr. Shane Kennedy, whose problem-solving skills were always timely and appreciated. Their humor and talent greatly lightened the load of my PhD journey. I am equally grateful to Kathleen Urrutia, a steadfast companion during those late-night protein purifications and early morning experiments.

I am also thankful to my fellow graduate peers, Dr. Jin Tang, Yu-Hsuan Chen, Jacob Parkins, Matthew Tippin, Martin Esparza Sanchez, Briana Hojo, Seanmory Sothy and Lael Cardinal, for their support, engaging discussions, and friendship throughout this challenging but rewarding journey.

In addition to the individuals mentioned above, I would like to extend my heartfelt appreciation to my friends Linbo Li, Dr. Zi Gao, Dr. Ziting Gao, Dr. Xiaomei He, Dr. Siyi Ge, Dr. Zhisheng Hu, Dr. Yi Huang, and not to forget Huahua, Oxy and Enigma. Your trust, friendship, support, and motivation have been pillars of strength for me. The moments of relief you provided have helped make both the tough times manageable and the achievements even more joyful.

Finally, my eternal gratitude goes to my mom, whose unconditional love and unwavering belief in my capabilities have been the bedrock of my endeavors. Her continuous support and encouragement have been fundamental to my journey.

To each of you mentioned and to the many others who have touched my life both academically and personally, I offer my profound gratitude. This dissertation is not just a reflection of my efforts but a testament to your collective influence on my journey. Your support has shaped not only this work but also the person I have become. I am deeply thankful for every word of encouragement, every moment of support, and every bit of advice you have provided. From the bottom of my heart, thank you all for being such an integral part of my story. Your impact is immeasurable and cherished deeply.

COPYRIGHT ACKNOWLEDGEMENTS

The text and figures, in part or full, are a reprint of the material as they appear in the following publication:

Chapter 2: Zhao, W., Xu, W., Tang, J., Kaushik, S., Chang, C.-E. A., & Zhao, L. (2023). Key Amino Acid Residues of Mitochondrial Transcription Factor A Synergize with Abasic (AP) Site Dynamics To Facilitate AP-Lyase Reactions. *ACS Chemical Biology*, 18(5), 1168–1179. https://doi.org/10.1021/acschembio.3c00047

Chapter 3: Zhao, W., Hussen, A. S., Freudenthal, B. D., Suo, Z., & Zhao, L. (2024). Mitochondrial transcription factor A (TFAM) has 5′-deoxyribose phosphate lyase activity in vitro. *DNA Repair*, 137, 103666. https://doi.org/10.1016/j.dnarep.2024.103666

DEDICATION

To my best friend Dr. Zi Gao
To my mother Chunxia Cao

ABSTRACT OF THE DISSERTATION

Elucidating the Mechanisms of TFAM in Mitochondrial DNA Maintenance: Studies Towards Understanding its Molecular Functions

by

Wenxin Zhao

Doctor of Philosophy, Graduate Program in Chemistry
University of California, Riverside, September 2024
Dr. Linlin Zhao, Chairperson

This study enhances our understanding of mitochondrial transcription factor A (TFAM) and its pivotal roles in maintaining mitochondrial DNA (mtDNA) integrity through a series of investigations. First, we focused on Glutamic acid 187 (E187) in the β-elimination reaction, which is an essential step in mtDNA repair. Using kinetic analyses and comprehensive computer simulations, we demonstrated how E187 accelerates the reaction rates quantitatively, providing critical insights into the molecular mechanisms that facilitate DNA repair within mitochondria.

Next, our study has demonstrated the intrinsic 5'dRp lyase activity of TFAM, observed through in vitro experiments. The activity rate is comparable with that of polymerase β, implying TFAM's vital role in the mitochondrial Base Excision Repair (BER) pathway. Such functionality is particularly significant since it indicates TFAM can

reduce the accumulation of toxic DNA repair intermediates. These intermediates if unrepaired, could lead to mitochondrial dysfunction, thus highlighting the broader implications of TFAM in maintaining cellular health and preventing disease progression.

Finally, my final work is focusing on developing an innovative mass spectrometry method to detect TFAM-DNA-protein complexes (DPCs) with lambda (λ) DNA as a proxy for mtDNA. This novel method aims to provide structural insights into how TFAM interacts with damaged DNA and allow us to identify other protein candidates that are binding with AP-DNA under physiological condition. Thus far, I have first streamlined the process of generating TFAM DPC with defined mass adduct, simplifying the mass spectrometry search process compared to scanning for various adducts. Additionally, I optimized the TFAM DPC extraction method using λ DNA as a mimic for mitochondrial DNA and confirmed successful TFAM DPC extraction and enrichment using ELISA. Building upon these results, in the near future, the extraction and enrichment of TFAM DPCs can be applied to cellular mtDNA. The development of this technique represents an important step towards elucidating the intricate dynamics of mtDNA-protein interactions within mitochondria.

Taken together, the above projects help with our understanding of TFAM's molecular interactions and regulatory roles and broaden our knowledge of mtDNA stability. By elucidating the mechanisms that protect mtDNA integrity, our research contributes to the broader scientific understanding of mitochondrial function and its impact on cellular health.

TABLE OF CONTENTS

Chapter 1: Introduction

1.1 Overview of Mitochondrial Function and mtDNA

1.1.1 Mitochondrial Roles and Structure

Mitochondria, often referred to as the powerhouses of the cell, are indispensable for various cellular functions, including ATP production, regulation of metabolic pathways, and the initiation of apoptosis. These organelles are unique due to their double-membrane structure and their own genetic material, mitochondrial DNA (mtDNA). Mitochondria play a critical role in cellular energy metabolism. The majority of cellular ATP is generated through oxidative phosphorylation (OXPHOS) within the mitochondrial inner membrane. During OXPHOS, electrons are transferred through a series of complexes (I-IV) in the electron transport chain (ETC), leading to the generation of a proton gradient that drives ATP synthesis by ATP synthase. This process is not only essential for energy production but also for the regulation of key metabolic intermediates[1].

Mitochondria are also central to the regulation of programmed cell death or apoptosis. They release pro-apoptotic factors like cytochrome c in response to cellular stress, which activate downstream caspases, leading to cell death. This function is crucial for maintaining cellular homeostasis and preventing the proliferation of damaged cells[2]. Additionally, mtDNA is more than just a repository of genetic material; it also acts as a signaling molecule that influences cellular responses to stress. This dual role underscores

the importance of mtDNA in both metabolic regulation and the activation of cellular defense mechanisms[3].

Mitochondria contain their own circular DNA (mtDNA), distinct from the nuclear genome. The mtDNA encodes 37 genes essential for mitochondrial function, including 13 proteins involved in the ETC, 22 transfer RNAs (tRNAs), and 2 ribosomal RNAs (rRNAs). Unlike nuclear DNA, mtDNA lacks protective histones and is located close to the inner mitochondrial membrane, where reactive oxygen species (ROS) are continuously produced as byproducts of the ETC. This proximity makes mtDNA particularly vulnerable to oxidative damage. Reactive oxygen species generated during OXPHOS can induce mutations and structural alterations in mtDNA. Research has shown that damaged mtDNA can be released into the cytosol, where it acts as a danger-associated molecular pattern (DAMP) to trigger innate immune responses. This signaling function highlights the broader role of mtDNA in cellular responses to stress and damage, beyond its traditional role in encoding mitochondrial proteins[4].

1.1.2 Significance of mtDNA Integrity

The maintenance of mtDNA integrity is essential for mitochondrial function and, by extension, cellular health (Fig. 1.1). Damage to mtDNA is implicated in aging and various diseases, including neurodegenerative disorders and cancer. Controlled mitochondrial-nuclear interactions are crucial in modulating the cellular response to mtDNA damage, underscoring the complex interplay between mitochondrial and nuclear genomes.

Mitochondrial DNA integrity is crucial for maintaining cellular function and overall health, as it plays a pivotal role in energy production through oxidative phosphorylation. Damage to mtDNA can lead to a cascade of cellular dysfunctions, including impaired energy production, increased oxidative stress, and activation of apoptotic pathways. These issues are particularly significant in high-energy-demanding tissues such as the brain, heart, and muscles. Research has shown that mtDNA damage accumulates with age, contributing to the aging process and age-related diseases[5]. This highlights the importance of mechanisms that maintain mtDNA integrity to ensure cellular homeostasis and longevity.

In the context of disease, compromised mtDNA integrity has been linked to various pathological conditions. For instance, in osteoarthritis (OA) chondrocytes, diminished mtDNA repair capacity and increased mtDNA damage have been observed, suggesting that mtDNA integrity is essential for maintaining cartilage health and function[6]. Similarly, in sperm from infertile men, reduced mtDNA integrity and altered mtDNA copy numbers have been associated with poor sperm quality and reduced fertility, underscoring the critical role of mtDNA in reproductive health[7,8]. These findings indicate that maintaining mtDNA integrity is vital for preventing and managing diseases that involve mitochondrial dysfunction.

Moreover, environmental factors can also impact mtDNA integrity. Exposure to pollutants has been shown to negatively affect mtDNA integrity and copy number in sperm, which could have implications for reproductive health and offspring development[9]. The repair and maintenance of mtDNA involve various enzymes and

pathways that protect against oxidative damage and ensure the accuracy of mtDNA replication. Understanding these mechanisms is crucial for developing therapeutic strategies to mitigate the effects of mtDNA damage in diseases and improve health outcomes[10,11].

1.2 Types and Sources of mtDNA Damage

1.2.1. Endogenous Damage

A major source of damage to mitochondrial DNA (mtDNA) comes from within the cell itself. Specifically, reactive oxygen species (ROS), which are byproducts of the normal energy production process in mitochondria, play a significant role. As mitochondria generate ATP through oxidative phosphorylation (OXPHOS), they also produce ROS like superoxide anions, hydrogen peroxide, and hydroxyl radicals. These reactive molecules can damage mtDNA, causing lesions such as 8-oxoguanine and strand breaks. This damage can interfere with mtDNA's ability to function properly, affecting its role in encoding essential proteins for mitochondrial function. The location of mtDNA, close to the inner mitochondrial membrane where ROS are produced, and its lack of protective histones make it particularly vulnerable[12].

Additionally, errors that occur during mtDNA replication are another significant source of mutations. As new mtDNA molecules are synthesized, replication errors can happen and accumulate over time. These errors can lead to point mutations, which are closely associated with aging and the development of various diseases, including neurodegenerative disorders and metabolic syndromes[13]. This accumulation of mutations

highlights the critical need for accurate mtDNA replication and robust repair mechanisms to correct these errors and maintain mitochondrial health.

1.2.2 Exogenous Damage

External factors also contribute significantly to mtDNA damage. Environmental toxins, ultraviolet (UV) light, and lifestyle choices all play a part. UV light and chemical pollutants can induce oxidative stress in cells, leading to the production of ROS and subsequent damage to mtDNA (Fig. 1.2). Lifestyle choices, such as diet and exposure to environmental pollutants, also affect mtDNA integrity. Studies have shown that poor dietary habits and exposure to environmental toxins can increase oxidative stress and lead to higher levels of mtDNA damage[14].

The impact of environmental pollutants on mtDNA is particularly concerning in the context of reproductive health. Research has found that pollutants can damage mtDNA in sperm, affecting both its integrity and copy number. This can have significant implications for fertility and the health of offspring[15]. These findings underscore the broader effects of environmental and lifestyle factors on mitochondrial health and the potential for transgenerational consequences of mtDNA damage.

Understanding where mtDNA damage comes from and the types of damage it can incur is crucial for developing strategies to protect and preserve mitochondrial function. The next chapter will explore how mtDNA repairs itself, counteracting the damage caused by both internal and external factors. By delving into these repair mechanisms, we can gain a deeper understanding of the relationship between mtDNA integrity and overall

cellular health, paving the way for potential therapeutic approaches to support mitochondrial function.

1.3 Mechanisms of mtDNA Repair

1.3.1 Base Excision Repair (BER) Pathway in Mitochondria

The Base Excision Repair (BER) pathway is essential for maintaining genomic integrity by repairing small base modifications such as oxidative damage, alkylation, and deamination. This is particularly important in mitochondria due to the high levels of reactive oxygen species (ROS) generated during oxidative phosphorylation (OXPHOS). These ROS frequently cause oxidative damage to mitochondrial DNA (mtDNA). The BER process includes several steps: recognizing and removing the damaged base, cleaving the DNA backbone, inserting the correct nucleotide, and ligating the DNA to restore its integrity[16].

Recent studies have provided deeper insights into the BER pathway in mitochondria, highlighting its critical role in routine repair processes and in protecting against age-related mitochondrial dysfunction and diseases. The significance of mitochondrial BER is further emphasized by findings linking deficiencies in this pathway to neurodegenerative diseases and other mitochondrial disorders. Efficient BER in mitochondria is crucial for preventing the accumulation of mtDNA mutations, which can lead to mitochondrial diseases and contribute to the aging process[17].

1.3.2 Key Proteins in Mitochondrial BER

DNA Glycosylases

DNA glycosylases are the first enzymes to act in the BER pathway. They recognize and excise damaged bases, creating an abasic site. In mitochondria, several glycosylases, such as OGG1 (8-oxoguanine DNA glycosylase) and NTH1 (endonuclease III-like protein 1), play critical roles in identifying and removing oxidized bases like 8-oxoguanine and thymine glycol. These enzymes ensure the initial steps of BER are accurately executed, preventing mutagenesis[17].

AP Endonucleases

After the damaged base is removed by DNA glycosylases, an apurinic/apyrimidinic (AP) site is formed. AP endonucleases, such as APE1, cleave the DNA backbone at these sites, creating a single-strand break. APE1, crucial for mitochondrial DNA repair, harbors a unique targeting sequence essential for its mitochondrial function[18]. Additionally, APE1 influences mitochondrial activity and is regulated by Parkin under stress conditions[19]. APE1 also has RNA phosphatase and exoribonuclease activities[20], and its nuclear localization in neurons depends on ATP levels[21].

DNA Polymerase γ

DNA polymerase γ (POLG) is the primary enzyme responsible for synthesizing new DNA in mitochondria. During the BER process, POLG inserts the correct nucleotide at the site of the cleaved DNA. POLG's high fidelity and proofreading activity are

essential for maintaining mtDNA integrity. Mutations in POLG can lead to mitochondrial diseases, highlighting its critical role in mitochondrial DNA maintenance[22].

DNA Ligase III

The final step of the BER pathway involves sealing the nick in the DNA backbone. DNA ligase III, along with its cofactor XRCC1 (X-ray repair cross-complementing protein 1), completes this step in the mitochondria. This ligase is specifically adapted to function in the mitochondrial environment, ensuring the completion of the repair process and the restoration of mtDNA integrity[14].

1.3.3. Regulation of BER in Mitochondria

The regulation of Base Excision Repair (BER) in mitochondria is a complex process that involves various post-translational modifications (PTMs) and interactions with other mitochondrial processes. These PTMs, such as phosphorylation, acetylation, and ubiquitination, are crucial for modulating the activity, stability, and interactions of BER proteins. For example, APE1, a key enzyme in the BER pathway, undergoes acetylation which influences its localization and function within mitochondria. Research has shown that SIRT3, a mitochondrial deacetylase, regulates the deacetylation of APE1, thereby modulating its activity in response to oxidative stress[23].

Mitochondrial dynamics, including changes in membrane potential and the processes of mitochondrial fusion and fission, also play significant roles in regulating BER activity. The mitochondrial membrane potential is essential for the import of nuclear-encoded DNA repair proteins into mitochondria. When this membrane potential is disrupted, as often seen in various pathological conditions, the import of BER proteins

is impaired, leading to reduced efficiency in mtDNA repair. Additionally, mitochondrial fusion and fission are critical for maintaining mitochondrial function and the proper distribution of mtDNA, which is necessary for efficient repair and replication. Recent studies indicate that proteins involved in these dynamic processes, such as DRP1 and MFN1, are themselves regulated by PTMs, which can indirectly influence BER efficiency[24].

Understanding the complex regulation of BER in mitochondria is crucial for comprehending how cells maintain mtDNA integrity under different physiological and pathological conditions. These insights pave the way for potential therapeutic strategies aimed at enhancing BER activity, thereby improving mitochondrial function and overall cellular health.

1.3.4. Alternative Repair Mechanisms

Mismatch Repair (MMR)

Mismatch Repair (MMR) is another crucial DNA repair mechanism that corrects base mismatches and insertion-deletion loops arising during DNA replication and recombination. While MMR is well-characterized in the nuclear genome, its presence and role in mitochondria are still being explored. Recent research suggests that mitochondrial MMR proteins, such as MutS homologs (MSH) and MutL homologs (MLH), are present in mitochondria and contribute to maintaining mtDNA integrity. These proteins identify and repair mismatched bases, preventing the spread of mutations that could lead to mitochondrial dysfunction[25].

Interestingly, MMR in mitochondria appears to be highly regulated and responsive to oxidative stress. The recruitment and activity of MMR proteins can be influenced by mitochondrial membrane potential and redox status. Studies have shown that oxidative damage can induce the expression and activation of mitochondrial MMR proteins, enhancing the repair of mismatches and protecting against mtDNA mutations. This suggests a sophisticated regulatory network that ensures the fidelity of mtDNA replication and repair under varying cellular conditions[14].

Double-Strand Break Repair (DSBR)

Double-Strand Break Repair (DSBR) is essential for addressing severe forms of DNA damage where both strands of the DNA double helix are broken. In mitochondria, DSBR mechanisms include homologous recombination (HR) and non-homologous end joining (NHEJ). HR is more accurate, using a homologous sequence as a template for repair, while NHEJ is quicker but more error-prone, joining the broken DNA ends directly. Recent findings highlight the presence of key HR proteins, such as RAD51 and BRCA1, in mitochondria, indicating a more significant role for HR in mtDNA maintenance than previously recognized[22].

DSBR in mitochondria is also influenced by mitochondrial dynamics and PTMs. Proteins involved in DSBR are regulated through phosphorylation and acetylation, which can modify their activity and interaction with other repair proteins. For example, the phosphorylation of RAD51 by ATM kinase in response to DNA damage enhances its capacity to facilitate homologous recombination. Similarly, acetylation of mitochondrial proteins can affect their stability and function in the DSBR process. These regulatory

mechanisms ensure a coordinated response to DNA damage and the maintenance of mtDNA integrity under stress conditions[17].

1.4 mtDNA Degradation Mechanisms

1.4.1. Necessity of mtDNA Degradation

Degrading damaged mitochondrial DNA (mtDNA) is vital for preventing the accumulation of mutations and maintaining mitochondrial quality. Accumulated mtDNA mutations can lead to mitochondrial dysfunction, which is linked to various diseases, including neurodegenerative disorders and metabolic syndromes. Recent studies highlight that selectively degrading defective mtDNA is a crucial part of mitochondrial quality control. This process ensures that only intact and functional mtDNA remains within the mitochondria, which is essential for optimal cellular function[12].

Moreover, the necessity of mtDNA degradation is emphasized by its role in preventing the transmission of harmful mutations to daughter cells. During cellular division, the selective removal of damaged mtDNA helps maintain the integrity of the mitochondrial genome, thereby preventing the inheritance of dysfunctional mitochondria. This is especially important in tissues with high cellular turnover and in germ cells, where the fidelity of mtDNA is critical for the health of offspring[26].

1.4.2. Processes Involved in mtDNA Degradation

Several recent studies have provided deeper insights into the enzymes and mechanisms involved in mtDNA degradation, highlighting the importance of this process in preventing the accumulation of mutations and ensuring cellular health.

Nucleases and Exonucleases

Nucleases and exonucleases play pivotal roles in the degradation of damaged mtDNA. Key enzymes include Endonuclease G (EndoG) and Exonuclease G (EXOG). EndoG is known for its role in apoptosis, where it translocates from the mitochondria to the nucleus to degrade chromosomal DNA. Within mitochondria, EndoG is involved in degrading damaged or unnecessary mtDNA. Recent research suggests that EndoG not only facilitates mtDNA degradation but also has regulatory functions in apoptosis and mitochondrial turnover, indicating a broader role in cellular homeostasis[27].

EXOG, another critical enzyme, primarily participates in the repair and degradation of single-stranded DNA breaks within the mitochondria. EXOG's activity ensures that only mtDNA that cannot be repaired is targeted for degradation, maintaining mitochondrial integrity. Studies have shown that EXOG's function is crucial for mitochondrial DNA stability, particularly under conditions of oxidative stress[13].

1.4.3. Mitochondrial Quality Control Mechanisms

Mitochondrial quality control involves identifying and removing severely damaged mtDNA to maintain mitochondrial function. This process is regulated through mitochondrial dynamics such as fission and fusion, which help segregate damaged mtDNA for degradation. Mitochondrial fission, mediated by proteins like DRP1, plays a crucial role in isolating damaged sections of the mitochondria. These damaged sections can then be targeted for mitophagy, a process where defective mitochondria are degraded by autophagosomes[28].

Fusion processes, mediated by proteins such as MFN1 and MFN2, help mix the contents within different mitochondria, crucial for maintaining mitochondrial function by allowing the exchange of mitochondrial DNA (mtDNA) and other components, thus preventing the accumulation of damaged mtDNA and promoting overall cellular health. Recent findings highlight that MFN2 is essential for maintaining mitochondrial membrane potential and is critical for the interaction between mitochondria and the endoplasmic reticulum, impacting lipid metabolism and cellular stress responses[29]. Additionally, MFN2 plays a unique role in brown adipose tissue function, influencing energy homeostasis and protecting against high-fat diet-induced insulin resistance[30].

1.4.4. Regulation of mtDNA Degradation

The degradation of mtDNA is tightly regulated by various factors, including mitochondrial membrane potential and signaling pathways that respond to cellular stress. This regulation is crucial for adapting to changing cellular conditions and preventing the propagation of damaged mtDNA. A decrease in mitochondrial membrane potential can trigger the selective degradation of damaged mtDNA, ensuring that only functional mitochondria are retained. This process is often mediated by PTEN-induced putative kinase 1 (PINK1) and the E3 ubiquitin ligase Parkin, which mark damaged mitochondria for degradation through mitophagy[31] .

Signaling pathways, such as those involving AMP-activated protein kinase (AMPK), also play a role in regulating mtDNA degradation. AMPK activation under conditions of cellular stress promotes mitochondrial biogenesis and the degradation of

damaged mtDNA. This helps adapt the mitochondrial network to changing cellular conditions and prevents the propagation of damaged mtDNA[32].

Recent research has highlighted the role of mitochondrial transcription factor A (TFAM) in regulating mtDNA degradation. TFAM binds to mtDNA and helps signal its degradation when it is extensively damaged. This process involves modulating autophagy and immune responses, with TFAM binding to cytoplasmic mtDNA to limit inflammation.

1.4.5. Recent Advances in Understanding mtDNA Degradation

Significant progress has been made in uncovering the regulatory mechanisms that control mtDNA degradation, revealing the involvement of mitochondrial-specific stress responses and autophagy-related pathways. The role of mitophagy in selectively degrading damaged mtDNA has been further clarified, emphasizing the importance of autophagic pathways in maintaining mitochondrial health[28].

Moreover, research has identified specific proteins and signaling molecules crucial for mtDNA degradation (Fig 1.3). For example, mitochondrial transcription factor A (TFAM) not only stabilizes mtDNA but also plays a role in signaling its degradation when it becomes extensively damaged. These findings provide a deeper understanding of the molecular mechanisms governing mtDNA degradation and highlight potential targets for therapeutic interventions in diseases associated with mitochondrial dysfunction[33,34].

1.5 Mitochondrial Dynamics: Fission, Fusion, and Mitophagy

Mitochondrial dynamics, which include fission, fusion, and mitophagy, are essential for maintaining the health of mitochondria and cells. These processes allow mitochondria to separate damaged parts and mix their contents, which helps dilute any damage and maintain cellular balance. Because mitochondria are highly dynamic, they can quickly adapt to changes in metabolic demands and stress, playing crucial roles in energy production, programmed cell death (apoptosis), and regulating various metabolic pathways[35–37].

1.5.1. Mitochondrial Fission

Mitochondrial fission is the process where a single mitochondrion splits into two or more smaller ones. This is important not only for distributing mitochondria during cell division but also for removing damaged mitochondria through a process called mitophagy. The main protein involved in this splitting is Dynamin-related protein 1 (DRP1). DRP1 gathers on the outer mitochondrial membrane and helps pinch it to create separate mitochondria. This splitting helps isolate damaged parts of mitochondria, which can then be broken down and removed, preventing the build-up of dysfunctional mitochondria[38].

DRP1 is regulated in a very complex way, involving various post-translational modifications like phosphorylation, sumoylation, and ubiquitination. These modifications affect DRP1's activity, stability, and localization within the cell. For example, when DRP1 is phosphorylated by kinases such as CDK1 during cell division, its activity

increases, ensuring that mitochondria split correctly and are properly distributed[39]. However, if DRP1 activity is not properly regulated, it can lead to excessive fission, causing mitochondria to fragment too much. This excessive fragmentation is linked to various diseases, including neurodegenerative disorders and heart diseases[40].

1.5.2. Mitochondrial Fusion

Mitochondrial fusion is the process where two or more mitochondria merge to form a single, larger mitochondrion. This merging is vital for maintaining mitochondrial function by mixing the contents of damaged mitochondria, which helps dilute localized damage and allows for the sharing of mitochondrial DNA (mtDNA) mutations. Fusion is primarily driven by Mitofusins (MFN1 and MFN2) on the outer mitochondrial membrane and Optic Atrophy 1 (OPA1) on the inner mitochondrial membrane[41].

Research shows that mitochondrial fusion is closely regulated by the cell's energy status and stress responses. For example, OPA1 activity is controlled by proteolytic cleavage, which is influenced by the mitochondrial membrane potential and stress signals. When the membrane potential is low, OPA1 is cleaved, which inhibits fusion and promotes fission. This helps isolate damaged mitochondria for removal. This adaptive response is crucial for maintaining mitochondrial quality and preventing the build-up of dysfunctional mitochondria, which can lead to cellular energy deficits and increased oxidative stress[42].

Additionally, enhancing mitochondrial fusion has been shown to mitigate some effects of mitochondrial dysfunction in diseases such as muscular dystrophy and metabolic syndromes[43].

1.5.3. Mitophagy

Mitophagy is the selective degradation of mitochondria by autophagy. It acts as a quality control mechanism to remove damaged or dysfunctional mitochondria, thereby maintaining a healthy mitochondrial population. The process begins with the accumulation of the PINK1 protein on the outer membrane of damaged mitochondria. This, in turn, recruits the E3 ubiquitin ligase Parkin, which ubiquitinates various mitochondrial outer membrane proteins, marking the mitochondrion for degradation by autophagosomes[44].

Recent advancements have highlighted the intricate regulation of mitophagy and its critical role in disease prevention. Studies have shown that impaired mitophagy leads to the accumulation of damaged mitochondria, contributing to neurodegenerative diseases such as Parkinson's and Alzheimer's. Enhancing mitophagy has been proposed as a therapeutic strategy to mitigate mitochondrial dysfunction in these diseases[45]. Efficient mitophagy requires a balance between fission and fusion processes to effectively isolate and degrade dysfunctional mitochondria.

Furthermore, discoveries in 2021 have uncovered new regulatory mechanisms and potential therapeutic targets for enhancing mitophagy. For example, inhibition of CDK9 has been shown to block PINK1-PRKN-mediated mitophagy by regulating the SIRT1-FOXO3-BNIP3 axis, offering promising pathways for intervention in mitochondrial diseases[46].

1.6 Mitochondrial Dynamics and mtDNA Signaling

1.6.1. Mitochondrial DNA Signaling

Mitochondrial dynamics, including fission and fusion, are closely linked to mtDNA signaling. Mitochondria contain their own genome, and any disruption in their dynamics can lead to the release of mtDNA into the cytoplasm. This release can act as a danger-associated molecular pattern (DAMP), triggering innate immune responses. It has been shown that mtDNA release during mitochondrial stress or damage can activate the cGAS-STING pathway, leading to the production of type I interferons and other pro-inflammatory cytokines. This pathway is crucial for antiviral responses and the overall immune defense mechanism[47].

Furthermore, mitochondrial fusion helps maintain mtDNA integrity by allowing the mixing of mtDNA from different mitochondria, thereby diluting mutations and maintaining genetic stability. Conversely, mitochondrial fission facilitates the segregation of damaged mtDNA, which can then be targeted for degradation through mitophagy. This dynamic balance ensures that mtDNA remains intact and functional, preventing the propagation of damaged mtDNA and maintaining cellular homeostasis[48].

In-depth investigations have elucidated the role of mtDNA signaling in cellular health. For example, the interaction between mitochondrial dynamics and mtDNA integrity is crucial for the cellular stress response. Disrupted mitochondrial fusion or fission can lead to chronic inflammatory states, which are implicated in various diseases, including autoimmune disorders and cancers[2,49].

1.6.2. Mitochondrial Dynamics and Immune Response

Mitochondrial dynamics also play a pivotal role in modulating the immune response. The release of mtDNA into the cytoplasm during mitochondrial stress acts as a potent activator of the innate immune system. This mtDNA-induced immune activation is crucial for the body's defense against infections and other pathological conditions. Research has shown that mitochondrial fission can enhance the immune response by promoting the release of mtDNA, which in turn activates signaling pathways such as TLR9 and the inflammasome, leading to the production of inflammatory cytokines[47].

Additionally, mitochondrial fusion can suppress excessive immune responses by maintaining mitochondrial integrity and preventing the unnecessary release of mtDNA. This regulatory mechanism ensures that the immune response is appropriately activated in the presence of genuine threats while avoiding chronic inflammation that can result from uncontrolled mtDNA release. Thus, the interplay between mitochondrial dynamics and immune signaling pathways is essential for maintaining a balanced immune response and preventing inflammatory diseases[48].

Further investigations have provided new insights into how mitochondrial dynamics influence immune responses. For instance, a study in 2023 revealed that modulating mitochondrial fission and fusion could be a therapeutic target for controlling inflammation in chronic diseases[2]. Additionally, discoveries have identified specific mitochondrial proteins that can regulate immune signaling, offering potential new avenues for therapeutic intervention in diseases characterized by excessive inflammation[50].

1.7 Interplay Between mtDNA Repair, Degradation, and Mitochondrial Dynamics

1.7.1. Integration of Mechanisms

Maintaining mitochondrial DNA (mtDNA) integrity requires a delicate balance between repair, degradation, and mitochondrial dynamics. These processes are intricately linked to ensure the optimal function of mitochondria and prevent the propagation of damaged mtDNA. Findings suggest that mtDNA repair mechanisms, such as base excision repair (BER), are closely coordinated with mitochondrial dynamics, including fission and fusion. These dynamics allow for the segregation of damaged mtDNA, facilitating its repair or degradation – currently, it is known that damage in mitochondrial DNA rarely get bypass or repair but prefer to depredate[51].

Mitochondrial fission, driven by proteins like DRP1, not only aids in distributing mitochondria during cell division but also isolates damaged mtDNA. Fusion processes, mediated by mitofusins (MFN1 and MFN2) and OPA1, mix mtDNA from different mitochondria, diluting mutations and enhancing genetic stability. Additionally, mitophagy—the process of degrading dysfunctional mitochondria—ensures that severely damaged mtDNA is removed from the cell. This interplay between repair, degradation, and mitochondrial dynamics is crucial for maintaining mitochondrial quality and function[52].

Over the past few years, additional insights have been gained into these mechanisms. Studies from 2022 to 2024 have highlighted how BER efficiency is modulated by mitochondrial dynamics, showing that changes in mitochondrial

morphology can enhance the accessibility and repair of mtDNA lesions (Schreier et al., 2022). Furthermore, novel proteins involved in coordinating mtDNA repair with fission and fusion processes have been identified, offering new targets for therapeutic intervention[53].

1.7.2. Implications for Cellular and Organismal Health

Maintaining mtDNA integrity is essential for cellular health and longevity. Disruptions in the balance of mtDNA repair, degradation, and mitochondrial dynamics can lead to a cascade of mitochondrial dysfunctions, contributing to various diseases. For instance, impaired mtDNA repair or defective mitophagy can result in the accumulation of damaged mtDNA, which has been linked to neurodegenerative diseases, cardiovascular disorders, and metabolic syndromes[5].

Enhancing mitochondrial quality control mechanisms has significant therapeutic potential. Targeting pathways that regulate mtDNA repair and degradation or modulating mitochondrial dynamics may help mitigate the effects of mitochondrial dysfunction in diseases. For example, promoting mitophagy to remove damaged mitochondria or enhancing the efficiency of mtDNA repair mechanisms can improve mitochondrial function and reduce disease progression. Research from 2022 to 2024 has shown promising results in animal models, where enhancing mitophagy or repair pathways ameliorated symptoms of neurodegenerative diseases and improved metabolic health[2,9].

Understanding these intricate mechanisms opens new avenues for developing treatments aimed at maintaining mitochondrial health and improving overall cellular and

organismal health. Continued exploration in this area holds the potential to translate these findings into effective therapies for a range of mitochondrial-related diseases[54].

1.8 Conclusion

Summary of Key Points

Maintaining the integrity of mitochondrial DNA (mtDNA) is essential for cellular health and function. This is due to its critical role in energy production, regulation of metabolic pathways, and initiation of apoptosis. This discussion focuses on recent insights into the Base Excision Repair (BER) pathway, mtDNA degradation mechanisms, and mitochondrial dynamics, including fission, fusion, and mitophagy.

Mitochondria produce ATP through oxidative phosphorylation (OXPHOS), a process that also generates reactive oxygen species (ROS). These ROS can damage mtDNA, leading to mutations and mitochondrial dysfunction. The BER pathway is crucial for repairing oxidative damage, involving key enzymes such as DNA glycosylases, APE1, DNA polymerase γ, and DNA ligase III[55]. Degrading damaged mtDNA with enzymes like EndoG and EXOG helps prevent the accumulation of mutations[56]. Mitochondrial dynamics, including fission and fusion, assist in segregating and repairing damaged mtDNA, while mitophagy removes severely damaged mitochondria to maintain a healthy mitochondrial population[52].

The interaction between these processes is vital for preventing the spread of damaged mtDNA and ensuring mitochondrial function. Disruptions in mtDNA repair, degradation, or mitochondrial dynamics are associated with various diseases, including neurodegenerative disorders, cardiovascular diseases, and metabolic syndromes.

Understanding these mechanisms is fundamental for developing therapeutic strategies to address mitochondrial dysfunction and improve health outcomes[2,5,9].

Future Directions

Future research should delve deeper into the molecular mechanisms that underpin mtDNA maintenance, especially the specific roles of various proteins involved in these processes. A comprehensive understanding of how post-translational modifications regulate BER pathway enzymes and how mitochondrial dynamics impact mtDNA repair and degradation is essential. This knowledge could pave the way for novel therapeutic interventions aimed at enhancing mitochondrial function and treating diseases associated with mitochondrial dysfunction.

One intriguing area to explore is the role of abasic (AP) sites and mitochondrial transcription factor A (TFAM) in maintaining mtDNA integrity. AP sites play a crucial part in the BER pathway, and their interactions with other repair proteins could shed light on the regulation of mtDNA repair. TFAM not only stabilizes mtDNA but also signals its degradation when the DNA is extensively damaged. Understanding the dual role of TFAM in both repair and degradation could lead to new therapeutic targets[57,58].

Another promising field of study is DNA-protein crosslinks (DPCs) within mitochondria. These crosslinks can disrupt DNA replication and transcription, and the mechanisms by which mitochondria detect and repair DPCs remain largely unknown. Investigating these processes could provide valuable insights into mitochondrial quality control and its overall impact on cellular health[59].

Expanding our knowledge of these molecular mechanisms is crucial for developing strategies to enhance mitochondrial function and address diseases associated with mitochondrial dysfunction. This research has the potential to lead to targeted therapies that can mitigate the effects of mitochondrial diseases, improving patient outcomes. Integrating these findings with broader studies on mitochondrial biology will be essential for translating basic science discoveries into clinical applications. By adopting this holistic approach, the scientific community can create effective therapies for a range of mitochondrial-related diseases, significantly impacting public health and longevity.

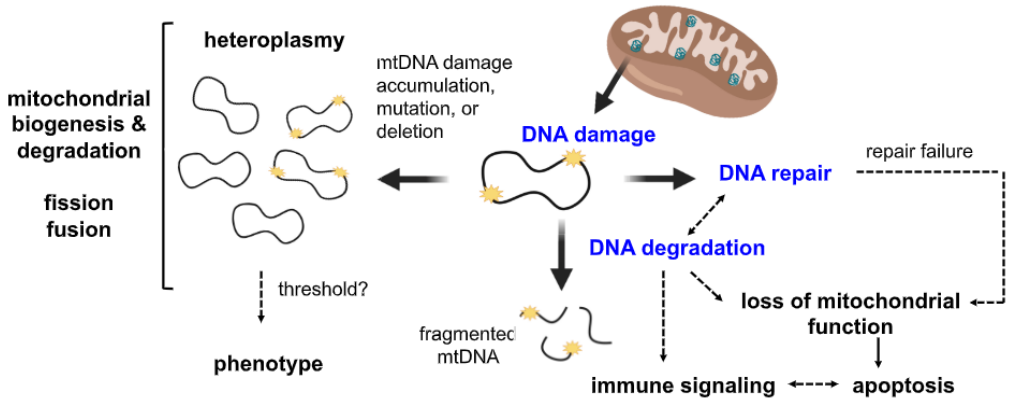

Figure 1.1. Scheme demonstrating the overall pathway of mitochondrial responds upon mtDNA damage. This includes mechanisms involved in the mtDNA repair pathway, and phenotypical change if damaged mtDNA accumulates, taking advantage of the fission and fusion property of the mitochondria. (Adopted from Ref 14)

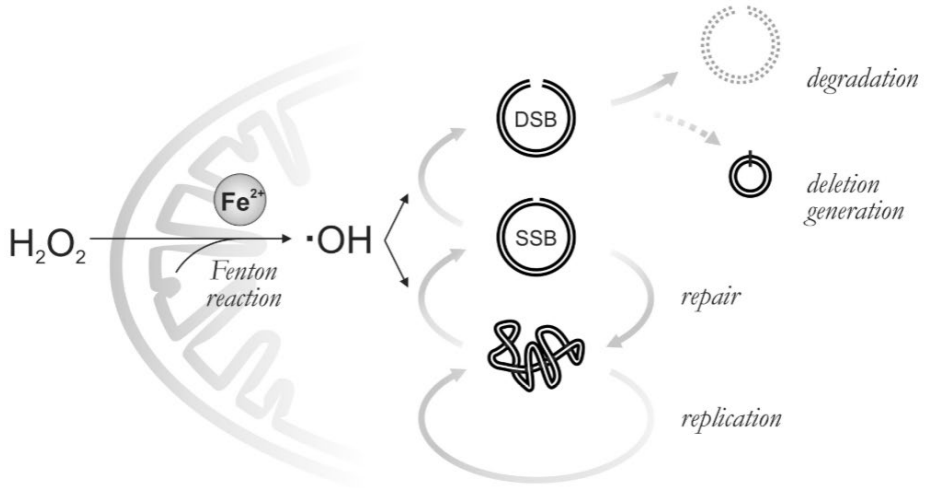

Figure 1.2. Scheme representing the fate of mtDNA after oxidative attack using H2O2. mtDNA upon attach forms molecules containing single strand breaks, then turning into linearized mtDNA molecules. These molecules are quickly degraded. (Adopted from Ref 51)

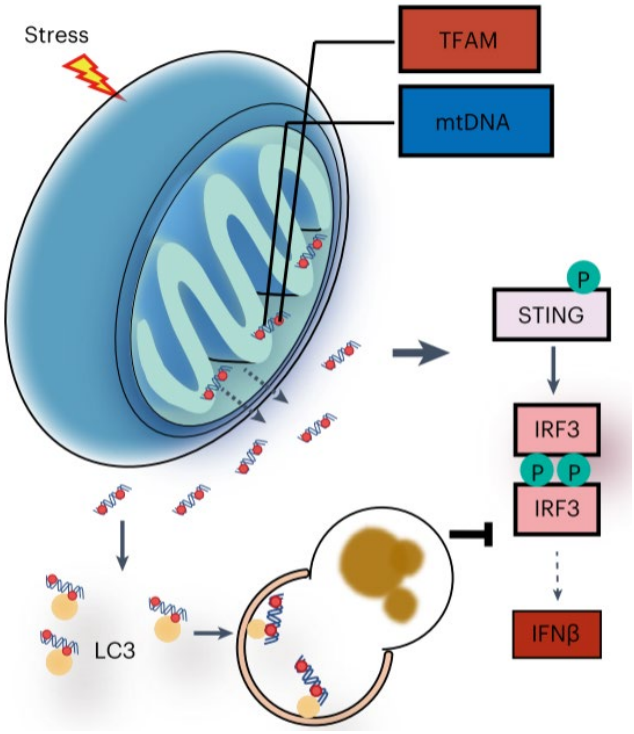

Figure 1.3. A proposed working model of TFAM-mediated nucleoid-phagy mitigating the cGAS–STING inflammatory pathway. (Adopted from Ref 33)

References

(1) Romesberg, A.; Van Houten, B. Targeting Mitochondrial Function with Chemoptogenetics. *Biomedicines*. 2022. DIO. 10.3390/biomedicines10102459.

(2) Liu, H.; Zhu, Z.; Xue, Q.; Yang, F.; Li, Z.; Xue, Z.; Cao, W.; He, J.; Guo, J.; Liu, X.; Shaw, A. E.; King, D. P.; Zheng, H. Innate Sensing of Picornavirus Infection Involves CGAS-STING-Mediated Antiviral Responses Triggered by Mitochondrial DNA Release. *PLoS Pathog* **2023**, *19* (2). DIO. 10.1371/journal.ppat.1011132.

(3) Xu, W.; Tang, J.; Zhao, L. DNA–Protein Cross-Links between Abasic DNA Damage and Mitochondrial Transcription Factor A (TFAM). *Nucleic Acids Res* **2023**, *51* (1), 41–53. DIO. 10.1093/nar/gkac1214.

(4) Newman, L. E.; Tadepalle, N.; Novak, S. W.; Schiavon, C. R.; Rojas, G. R.; Chevez, J. A.; Lemersal, I.; Medina, M.; Rocha, S.; Towers, C. G.; Grotjahn, D. A.; Manor, U.; Shadel, G. S. *Endosomal Removal and Disposal of Dysfunctional, Immunostimulatory Mitochondrial DNA*; 2022.

(5) Shang, D.; Huang, M.; Wang, B.; Yan, X.; Wu, Z.; Zhang, X. MtDNA Maintenance and Alterations in the Pathogenesis of Neurodegenerative Diseases. *Curr Neuropharmacol* **2022**, *21* (3). DIO. 10.2174/1570159x20666220810114644.

(6) Grishko, V. I.; Ho, R.; Wilson, G. L.; Pearsall IV, A. W. Diminished Mitochondrial DNA Integrity and Repair Capacity in OA Chondrocytes. *Osteoarthritis Cartilage* **2009**, *17* (1). DIO. 10.1016/j.joca.2008.05.009.

(7) Song, G. J.; Lewis, V. Mitochondrial DNA Integrity and Copy Number in Sperm from Infertile Men. *Fertil Steril* **2008**, *90* (6). DIO. 10.1016/j.fertnstert.2007.10.059.

(8) Zhunina, O. A.; Yabbarov, N. G.; Grechko, A. V.; Yet, S.-F.; Sobenin, I. A.; Orekhov, A. N. Neurodegenerative Diseases Associated with Mitochondrial DNA Mutations. *Curr Pharm Des* **2019**, *26* (1). DIO. 10.2174/1381612825666191122091320.

(9) Todosenko, N.; Khaziakhmatova, O.; Malashchenko, V.; Yurova, K.; Bograya, M.; Beletskaya, M.; Vulf, M.; Gazatova, N.; Litvinova, L. Mitochondrial Dysfunction Associated with MtDNA in Metabolic Syndrome and Obesity. *International Journal of Molecular Sciences*. 2023. DIO. 10.3390/ijms241512012.

(10) Kang, D.; Hamasaki, N. Maintenance of Mitochondrial DNA Integrity: Repair and Degradation. *Current Genetics*. 2002. DIO. 10.1007/s00294-002-0312-0.

(11) Yuzefovych, L. V.; Kahn, A. G.; Schuler, M. A.; Eide, L.; Arora, R.; Wilson, G. L.; Tan, M.; Rachek, L. I. Mitochondrial DNA Repair through OGG1 Activity Attenuates Breast Cancer Progression and Metastasis. *Cancer Res* **2016**, *76* (1). DIO. 10.1158/0008-5472.CAN-15-0692.

(12) Pinto, M.; Moraes, C. T. Mechanisms Linking MtDNA Damage and Aging. *Free Radical Biology and Medicine*. 2015. DIO. 10.1016/j.freeradbiomed.2015.05.005.

(13) Kazachkova, N.; Ramos, A.; Santos, C.; Lima, M. Mitochondrial DNA Damage Patterns and Aging: Revising the Evidences for Humans and Mice. *Aging and Disease*. 2013. DIO. 10.14336/AD.2013.0400337.

(14) Zhao, L.; Sumberaz, P. Mitochondrial DNA Damage: Prevalence, Biological Consequence, and Emerging Pathways. *Chemical Research in Toxicology*. American Chemical Society October 19, 2020, pp 2491–2502. DIO. 10.1021/acs.chemrestox.0c00083.

(15) Zhang, G.; Jiang, F.; Chen, Q.; Yang, H.; Zhou, N.; Sun, L.; Zou, P.; Yang, W.; Cao, J.; Zhou, Z.; Ao, L. Associations of Ambient Air Pollutant Exposure with Seminal Plasma MDA, Sperm MtDNA Copy Number, and MtDNA Integrity. *Environ Int* **2020**, *136*. DIO. 10.1016/j.envint.2020.105483.

(16) Herrmann, G. K.; Yin, Y. W. The Role of Poly(ADP-Ribose) Polymerase 1 in Nuclear and Mitochondrial Base Excision Repair. *Biomolecules*. 2023. DIO. 10.3390/biom13081195.

(17) SenGupta, T.; Palikaras, K.; Esbensen, Y. Q.; Konstantinidis, G.; Galindo, F. J. N.; Achanta, K.; Kassahun, H.; Stavgiannoudaki, I.; Bohr, V. A.; Akbari, M.; Gaare, J.; Tzoulis, C.; Tavernarakis, N.; Nilsen, H. Base Excision Repair Causes Age-Dependent Accumulation of Single-Stranded DNA Breaks That Contribute to Parkinson Disease Pathology. *Cell Rep* **2021**, *36* (10). DIO. 10.1016/j.celrep.2021.109668.

(18) Li, M.; Zhong, Z.; Zhu, J.; Xiang, D.; Dai, N.; Cao, X.; Qing, Y.; Yang, Z.; Xie, J.; Li, Z.; Baugh, L.; Wang, G.; Wang, D. Identification and Characterization of Mitochondrial Targeting Sequence of Human Apurinic/Apyrimidinic Endonuclease 1. *J Biol Chem* **2010**, *285* (20), 14871–14881. DIO. 10.1074/JBC.M109.069591.

(19) Scott, T. L.; Wicker, C. A.; Suganya, R.; Dhar, B.; Pittman, T.; Horbinski, C.; Izumi, T. Polyubiquitination of Apurinic/Apyrimidinic Endonuclease 1 by Parkin. *Mol Carcinog* **2017**, *56* (2). DIO. 10.1002/mc.22495.

(20) Chohan, M.; Mackedenski, S.; Li, W. M.; Lee, C. H. Human Apurinic/Apyrimidinic Endonuclease 1 (APE1) Has 3′ RNA Phosphatase and 3′ Exoribonuclease Activities. *J Mol Biol* **2015**, *427* (2). DIO. 10.1016/j.jmb.2014.12.001.

(21) Singh, S.; Englander, E. W. Nuclear Depletion of Apurinic/Apyrimidinic Endonuclease 1 (Ape1/Ref-1) Is an Indicator of Energy Disruption in Neurons. *Free Radic Biol Med* **2012**, *53* (9). DIO. 10.1016/j.freeradbiomed.2012.07.025.

(22) Gredilla, R.; Sánchez-Román, I.; Gómez, A.; López-Torres, M.; Barja, G. Mitochondrial Base Excision Repair Positively Correlates with Longevity in the Liver and Heart of Mammals. *Geroscience* **2020**, *42* (2). DIO. 10.1007/s11357-020-00158-4.

(23) Allkanjari, K.; Baldock, R. A. Beyond Base Excision Repair: An Evolving Picture of Mitochondrial DNA Repair. *Bioscience Reports*. 2021. DIO. 10.1042/BSR20211320.

(24) Sharma, N.; Pasala, M. S.; Prakash, A. Mitochondrial DNA: Epigenetics and Environment. *Environ Mol Mutagen* **2019**, *60* (8), 668–682. DIO. 10.1002/EM.22319.

(25) Chakraborty, A.; Tapryal, N.; Islam, A.; Mitra, S.; Hazra, T. Transcription Coupled Base Excision Repair in Mammalian Cells: So Little Is Known and so Much to Uncover. *DNA Repair (Amst)* **2021**, *107*. DIO. 10.1016/j.dnarep.2021.103204.

(26) Stewart, J. B.; Freyer, C.; Elson, J. L.; Larsson, N. G. Purifying Selection of MtDNA and Its Implications for Understanding Evolution and Mitochondrial Disease. *Nature Reviews Genetics*. 2008. DIO. 10.1038/nrg2396.

(27) Kozhukhar, N.; Spadafora, D.; Fayzulin, R.; Shokolenko, I. N.; Alexeyev, M. The Efficiency of the Translesion Synthesis across Abasic Sites by Mitochondrial DNA Polymerase Is Low in Mitochondria of 3T3 Cells. *Mitochondrial DNA Part A* **2016**, *27* (6), 4390–4396. DIO. 10.3109/19401736.2015.1089539.

(28) Youle, R. J.; Van Der Bliek, A. M. Mitochondrial Fission, Fusion, and Stress. *Science*. 2012. DIO. 10.1126/science.1219855.

(29) Lloberas, J.; Muñoz, J. P.; Hernández-Álvarez, M. I.; Cardona, P. J.; Zorzano, A.; Celada, A. Macrophage Mitochondrial MFN2 (Mitofusin 2) Links Immune Stress and Immune Response through Reactive Oxygen Species (ROS) Production. *Autophagy*. 2020. DIO. 10.1080/15548627.2020.1839191.

(30) Boutant, M.; Kulkarni, S. S.; Joffraud, M.; Ratajczak, J.; Valera-Alberni, M.; Combe, R.; Zorzano, A.; Cantó, C. Mfn2 Is Critical for Brown Adipose Tissue Thermogenic Function. *EMBO J* **2017**, *36* (11). DIO. 10.15252/embj.201694914.

(31) Ge, P.; Dawson, V. L.; Dawson, T. M. PINK1 and Parkin Mitochondrial Quality Control: A Source of Regional Vulnerability in Parkinson's Disease. *Molecular Neurodegeneration*. 2020. DIO. 10.1186/s13024-020-00367-7.

(32) Jiang, S.; Park, D. W.; Gao, Y.; Ravi, S.; Darley-Usmar, V.; Abraham, E.; Zmijewski, J. W. Participation of Proteasome-Ubiquitin Protein Degradation in Autophagy and the Activation of AMP-Activated Protein Kinase. *Cell Signal* **2015**, *27* (6). DIO. 10.1016/j.cellsig.2015.02.024.

(33) Liu, H.; Zhen, C.; Xie, J.; Luo, Z.; Zeng, L.; Zhao, G.; Lu, S.; Zhuang, H.; Fan, H.; Li, X.; Liu, Z.; Lin, S.; Jiang, H.; Chen, Y.; Cheng, J.; Cao, Z.; Dai, K.; Shi, J.; Wang, Z.; Hu, Y.; Meng, T.; Zhou, C.; Han, Z.; Huang, H.; Zhou, Q.; He, P.; Feng, D. TFAM Is an Autophagy Receptor That Limits Inflammation by Binding to Cytoplasmic Mitochondrial DNA. *Nat Cell Biol* **2024**. DIO. 10.1038/s41556-024-01419-6.

(34) Newman, L. E.; Weiser Novak, S.; Rojas, G. R.; Tadepalle, N.; Schiavon, C. R.; Grotjahn, D. A.; Towers, C. G.; Tremblay, M. È.; Donnelly, M. P.; Ghosh, S.; Medina, M.; Rocha, S.; Rodriguez-Enriquez, R.; Chevez, J. A.; Lemersal, I.; Manor, U.; Shadel, G. S. Mitochondrial DNA Replication Stress Triggers a Pro-Inflammatory Endosomal Pathway of Nucleoid Disposal. *Nat Cell Biol* **2024**, *26* (2), 194–206. DIO. 10.1038/s41556-023-01343-1.

(35) Lin, J.; Duan, J.; Wang, Q.; Xu, S.; Zhou, S.; Yao, K. Mitochondrial Dynamics and Mitophagy in Cardiometabolic Disease. *Frontiers in Cardiovascular Medicine*. 2022. DIO. 10.3389/fcvm.2022.917135.

(36) Adebayo, M.; Singh, S.; Singh, A. P.; Dasgupta, S. Mitochondrial Fusion and Fission: The Fine-Tune Balance for Cellular Homeostasis. *FASEB Journal*. 2021. DIO. 10.1096/fj.202100067R.

(37) Kasahara, A.; Scorrano, L. Mitochondria: From Cell Death Executioners to Regulators of Cell Differentiation. *Trends in Cell Biology*. 2014. DIO. 10.1016/j.tcb.2014.08.005.

(38) Jin, J. yu; Wei, X. xiang; Zhi, X. ling; Wang, X. hong; Meng, D. Drp1-Dependent Mitochondrial Fission in Cardiovascular Disease. *Acta Pharmacologica Sinica*. 2021. DIO. 10.1038/s41401-020-00518-y.

(39) Cho, B.; Kim, H.; Cho, H. M.; Kim, H. J.; Jeong, J.; Park, S. K.; Hwang, E. M.; Park, J. Y.; Kim, W. R.; Sun, W. CDK5-Dependent Inhibitory Phosphorylation of Drp1 during Neuronal Maturation. *Exp Mol Med* **2014**, *46* (7). DIO. 10.1038/emm.2014.36.

(40) Ji, Y.; Zhou, H.; Yang, C.; Li, J. Post-Translational Modification of Drp1 Is a Promising Target for Treating Cardiovascular Diseases. *Cardiovascular Innovations and Applications*. 2023. DIO. 10.15212/CVIA.2023.0043.

(41) Chen, Y.; Csordás, G.; Jowdy, C.; Schneider, T. G.; Csordás, N.; Wang, W.; Liu, Y.; Kohlhaas, M.; Meiser, M.; Bergem, S.; Nerbonne, J. M.; Dorn, G. W.; Maack, C. Mitofusin 2-Containing Mitochondrial-Reticular Microdomains Direct Rapid Cardiomyocyte Bioenergetic Responses via Interorganelle Ca2+ Crosstalk. *Circ Res* **2012**, *111* (7). DIO. 10.1161/CIRCRESAHA.112.266585.

(42) Hu, Y.; Chen, H.; Zhang, L.; Lin, X.; Li, X.; Zhuang, H.; Fan, H.; Meng, T.; He, Z.; Huang, H.; Gong, Q.; Zhu, D.; Xu, Y.; He, P.; Li, L.; Feng, D. The AMPK-MFN2 Axis Regulates MAM Dynamics and Autophagy Induced by Energy Stresses. *Autophagy* **2021**, *17* (5). DIO. 10.1080/15548627.2020.1749490.

(43) Burtscher, M.; Burtscher, J. MFN2: Shaping Mitochondria and Cardiac Adaptations to Hypoxia. *Acta Physiologica*. 2023. DIO. 10.1111/apha.14026.

(44) Nguyen, T. N.; Padman, B. S.; Lazarou, M. Deciphering the Molecular Signals of PINK1/Parkin Mitophagy. *Trends in Cell Biology*. 2016. DIO. 10.1016/j.tcb.2016.05.008.

(45) Quinn, P. M. J.; Moreira, P. I.; Ambrósio, A. F.; Alves, C. H. PINK1/PARKIN Signalling in Neurodegeneration and Neuroinflammation. *Acta neuropathologica communications*. 2020. DIO. 10.1186/s40478-020-01062-w.

(46) Yao, J.; Wang, J.; Xu, Y.; Guo, Q.; Sun, Y.; Liu, J.; Li, S.; Guo, Y.; Wei, L. CDK9 Inhibition Blocks the Initiation of PINK1-PRKN-Mediated Mitophagy by Regulating the SIRT1-FOXO3-BNIP3 Axis and Enhances the Therapeutic Effects Involving Mitochondrial Dysfunction in Hepatocellular Carcinoma. *Autophagy* **2022**, *18* (8). DIO. 10.1080/15548627.2021.2007027.

(47) Maekawa, H.; Inoue, T.; Ouchi, H.; Jao, T. M.; Inoue, R.; Nishi, H.; Fujii, R.; Ishidate, F.; Tanaka, T.; Tanaka, Y.; Hirokawa, N.; Nangaku, M.; Inagi, R. Mitochondrial Damage Causes Inflammation via CGAS-STING Signaling in Acute Kidney Injury. *Cell Rep* **2019**, *29* (5). DIO. 10.1016/j.celrep.2019.09.050.

(48) Li, Y.; Chen, H.; Yang, Q.; Wan, L.; Zhao, J.; Wu, Y.; Wang, J.; Yang, Y.; Niu, M.; Liu, H.; Liu, J.; Yang, H.; Wang, Y.; Wan, S.; Bao, D. Mitochondrial Fission-

Induced MtDNA Stress Promotes ESCC Progression by CGAS-STING Mediated Autophagy. **2021**. DIO. 10.21203/RS.3.RS-961546/V1.

(49) Bai, J.; Cervantes, C.; Liu, J.; He, S.; Zhou, H.; Zhang, B.; Cai, H.; Yin, D.; Hu, D.; Li, Z.; Chen, H.; Gao, X.; Wang, F.; O'Connor, J. C.; Xu, Y.; Liu, M.; Dong, L. Q.; Liu, F. DsbA-L Prevents Obesity-Induced Inflammation and Insulin Resistance by Suppressing the MtDNA Release-Activated CGAS-CGAMP-STING Pathway. *Proc Natl Acad Sci U S A* **2017**, *114* (46). DIO. 10.1073/pnas.1708744114.

(50) Wang, L.; Li, X.; Hanada, Y.; Hasuzawa, N.; Moriyama, Y.; Nomura, M.; Yamamoto, K. Dynamin-Related Protein 1 Deficiency Accelerates Lipopolysaccharide-Induced Acute Liver Injury and Inflammation in Mice. *Commun Biol* **2021**, *4* (1). DIO. 10.1038/s42003-021-02413-6.

(51) Trombly, G.; Said, A. M.; Kudin, A. P.; Peeva, V.; Altmüller, J.; Becker, K.; Köhrer, K.; Zsurka, G.; Kunz, W. S. The Fate of Oxidative Strand Breaks in Mitochondrial DNA. *Antioxidants* **2023**, *12* (5). DIO. 10.3390/antiox12051087.

(52) de Bovi Pontes, C.; Jefferys, C.; Bedwan, M.; Ciesielska, E. J.; Ciesielski, G. L. Implications of DNA Polymerase Gamma in the Repair of the Mitochondrial Genome. *The FASEB Journal* **2022**, *36* (S1). DIO. 10.1096/fasebj.2022.36.s1.r4339.

(53) Baek, L. M.; Lee, J.; Barrish, J. P.; Lim, B.; Chang, J. T.; Lorenzi, P. L.; Porter, W.; Echeverria, G. V. Abstract P4-01-08: Morphological and Functional Plasticity of Mitochondria in Chemoresistant Triple Negative Breast Cancer. *Cancer Res* **2022**, *82* (4_Supplement). DIO. 10.1158/1538-7445.sabcs21-p4-01-08.

(54) Boschetti, E.; Caporali, L.; D'Angelo, R.; Malagelada, C.; Accarino, A.; Dotti, M. T.; Costa, R.; Cenacchi, G.; Pironi, L.; Rinaldi, R.; Stanghellini, V.; Ratti, S.; Manzoli, L.; Carelli, V.; De Giorgio, R. Anatomical Laser Microdissection of the Ileum Reveals MtDNA Depletion Recovery in A Mitochondrial Neuro-Gastrointestinal Encephalomyopathy (MNGIE) Patient Receiving Liver Transplant. *Int J Mol Sci* **2022**, *23* (15). DIO. 10.3390/ijms23158792.

(55) Kumar, A.; Reed, A. J.; Zahurancik, W. J.; Daskalova, S. M.; Hecht, S. M.; Suo, Z. Interlocking Activities of DNA Polymerase β in the Base Excision Repair Pathway. *Proceedings of the National Academy of Sciences* **2022**, *119* (10). DIO. 10.1073/pnas.2118940119.

(56) Szymanski, M. R.; Karlowicz, A.; Herrmann, G. K.; Cen, Y.; Yin, Y. W. Human EXOG Possesses Strong AP Hydrolysis Activity: Implication on Mitochondrial DNA Base Excision Repair. *J Am Chem Soc* **2022**. DIO. 10.1021/jacs.2c10558.

(57) Zhao, W.; Xu, W.; Tang, J.; Kaushik, S.; Chang, C.-E. A.; Zhao, L. Key Amino Acid Residues of Mitochondrial Transcription Factor A Synergize with Abasic (AP) Site Dynamics To Facilitate AP-Lyase Reactions. *ACS Chem Biol* **2023**, *18* (5), 1168–1179. DIO. 10.1021/acschembio.3c00047.

(58) Liu, C.; Le, B. H.; Xu, W.; Yang, C. H.; Chen, Y. H.; Zhao, L. Dual Chemical Labeling Enables Nucleotide-Resolution Mapping of DNA Abasic Sites and Common Alkylation Damage in Human Mitochondrial DNA. *Nucleic Acids Res* **2023**, *51* (13). DIO. 10.1093/nar/gkad502.

(59) Platz, K. R.; Rudisel, E. J.; Paluch, K. V.; Laurin, T. R.; Dittenhafer-Reed, K. E. Assessing the Role of Post-Translational Modifications of Mitochondrial RNA Polymerase. *Int J Mol Sci* **2023**, *24* (22). DIO. 10.3390/ijms242216050.

Chapter 2: The Key Amino Acid Residues of Mitochondrial Transcription Factor A (TFAM) Synergize with Abasic (AP) Site Dynamics to Facilitate AP-Lyase Reactions

2.1 Introduction

In higher eukaryotes, mitochondria are essential subcellular organelles for energy production, metabolism, and signaling.[1] Mitochondrial DNA (mtDNA) encodes 13 protein subunits of the oxidative phosphorylation system and a set of tRNAs and rRNAs. Compared to nuclear DNA (nDNA), mtDNA is more susceptible to chemical modifications by endogenous and exogenous factors partly due to its proximity to the oxidative phosphorylation system and the lack of certain DNA repair pathways.[2–4] Unrepaired DNA lesions, point mutations, and deletions in the mitochondrial genome contribute to the heterogeneity of mtDNA, also known as mtDNA heteroplasmy, which has been implicated in mitochondrial diseases, neurodegeneration, and cancer.[5,6] mtDNA damage is counteracted by a robust mitochondrial base excision repair system, its multi-copy *characteristic*, and rapid mtDNA turnover,[2,7,8] which occur in the context of mitochondrial dynamics and mitophagy.[9] The systems to protect mtDNA also include scavengers of reactive oxygen species, such as superoxide dismutase and mitochondrial glutathione peroxidase 1.[10] Notably, when cultured cells or experimental animals are exposed to genotoxic chemicals, damaged mtDNA molecules are quickly degraded upon genotoxic stress without an increase in the mutation load.[9,11,12] Even under unstressed

conditions, the half-life of mtDNA is only in a matter of days.[13] The mtDNA copy number fluctuates in a given tissue and varies considerably based on the cell and tissue types.[7] Furthermore, the degraded mtDNA fragments are known to translocate to the cytoplasm and trigger immunological pathways.[3,14,15] Together, the rapid turnover of mtDNA, its susceptibility to damage, and the functional importance of released mtDNA in immune responses have led to the proposed role of mtDNA as a cellular genotoxic stress sensor.[3]

Mechanistically, how damaged mtDNA molecules are degraded remains partially understood. A few enzymes have been shown to be involved in mtDNA degradation, including the exonuclease domain of DNA polymerase (pol) γ[16,17], genome maintenance exonuclease 1 (MGME1)[16,18] with controversies,[15,19] and flap endonuclease 1 (FEN1).[15] Pol γ and MGME1 process mtDNA containing induced double-strand breaks into shorter fragments in mammalian cells and mouse models.[16–18] FEN1 has been implicated in promoting mtDNA fragment release into cytoplasm on the basis of reduced cytosolic mtDNA fragments upon silencing Fen1.[15] In addition, mitochondrial transcription factor A (TFAM) has emerged as a new player in mtDNA turnover.[20–22] As a key mtDNA-packaging protein, TFAM organizes mtDNA into DNA-protein complexes known as nucleoids.[23] Besides, TFAM is an essential factor in mtDNA transcription activation.[24,25] Recently, TFAM has been shown to cleave DNA molecules containing abasic (AP) sites in vitro and in cells,[20,21] arguing its role in damaged mtDNA turnover. AP sites are one of the most abundant DNA lesions in mtDNA and nDNA, present at a level of 1 AP lesion/10^5-10^6 nt.[26]

Key to the AP lyase activity of TFAM is its high Lys content (15% of the amino acid residues in the mature TFAM). A proximal Lys activates an AP lesion for β-elimination via Schiff-base chemistry to form single-strand breaks (SSBs).[20, 21] A body of literature in the DNA repair field has shown that for DNA glycosylases, the β-elimination step can be catalyzed by carboxylate-containing Glu or Asp residues (e.g., T4 endonuclease V[27]), primary or secondary amines (e.g., NEIL1[28], also reviewed in ref. [29]). Similarly, pol β uses E71 to perform a water-assisted H-abstraction at the C2′ position to achieve its dRp-lyase activity.[30] Historically, the effects of carboxylate-containing amino acid residues on the Schiff base intermediates have been extensively studied with rhodopsin systems.[31] Remarkably, the abundance of Glu (12%) in TFAM is much higher than its average abundance (6.9%) in the human proteome (Table 2.1), and such a high frequency is conserved in TFAM homologs from different species (Table 2.2). Intriguingly, more than half of these Glu residues in TFAM are present in KE clusters (Fig. 2.1B). Considering that multiple Lys residues can be involved in Schiff base formation with AP sites, a proximal Glu would be able to facilitate β-elimination by the deprotonating the 2′ carbon atom of the sugar ring, or serving as a Schiff base counterion, or both. Yet, the potential contribution of the highly abundantly Glu residues to the AP-lyase activity of TFAM has not been explored.

Herein, we clarify the role of a Glu residue (E187) in TFAM-mediated AP-DNA cleavage using wet-lab experiments and computer simulations. E187 is chosen given its proximity to the hotspot K186 in TFAM-facilitated AP-lyase reactions.[20,21,32] We demonstrate that E187 facilitates β-elimination through detailed kinetic analysis and

molecular dynamics (MD) simulations. Our kinetic assays and simulations show that TFAM E187A variant has a reduced rate of β-elimination. MD simulations revealed that AP sites in the TFAM-DNA complex exhibits both intrahelical and extrahelical conformations with the latter facilitating the Schiff base formation. Collectively, our data shed light on the importance of E187 in the TFAM-mediated AP-lyase reactions and provide a basis for understanding the high abundance of Glu in TFAM homologs and their role in mtDNA maintenance.

2.2 Materials and Methods

Reagents

Unless specified otherwise, chemicals were from Sigma Aldrich (St. Louis, MO) or Fisher Scientific and were of the highest grade. MS grade trypsin was from Fisher Scientific. *E. coli* BL21 (DE3) competent cells and uracil DNA glycosylase (UDG) were from New England Biolabs (Cat. No M0280S, Ipswich, MA). Pronase E was from MedChemExpress (Monmouth Junction, NJ, Cat. No HY-114158). The pET28a vectors expressing the mature form of human TFAM (amino acid 43-246) variants were constructed by GenScript (Piscataway, NJ). Human TFAM cDNA was inserted at the restriction enzyme site Nde I. Constructs expressing TFAM variants were created by site-directed mutagenesis by GenScript. Oligodeoxynucleotides were synthesized and HPLC-purified by Integrated DNA Technologies (Coralville, IA).

Electrophoretic mobility shift assay

The reaction solution contains 20 mM HEPES (pH 7.4), 90 mM NaCl, 20 mM EDTA, 4 μM DNA substrate (dU-containing duplex), and increasing concentrations TFAM. All reactions were prepared on ice and mixed with a loading buffer containing glycerol with bromophenol and xylene-cyanol. Electrophoresis was carried out on a 6% polyacrylamide (acrylamide/bis-acrylamide) gel in 0.35X TBE (Tris-Borate-EDTA) buffer at 100 V and 4 °C. The gel was imaged with a Typhoon imager (Cytiva, previously GE Healthcare Life Sciences) and quantified using ImageQuant software (Cytiva). Data were graphed using GraphPad Prism (v8.0).

Reactions of TFAM with AP-DNA

TFAM and AP-DNA reactions were conducted and analyzed similarly to the previous procedures with modifications [20]. Briefly, wild-type (wt) TFAM or variants were incubated with AP-DNA to monitor the rates of strand scission and SSB and DPC formation. Reactions contained 4 μM AP-DNA, 8 μM TFAM (wt or variant), 20 mM HEPES (pH 7.4), 90 mM NaCl, and 20 mM EDTA, with or without 25 mM $NaBH_3CN$. Reactions under pH 6.2 were in 50 mM of MES (2-(*N*-morpholino)ethanesulfonic acid) buffer, and reactions under pH 8.7 were in 50 mM sodium carbonate-bicarbonate buffer. Reactions were carried out at 37 °C with aliquots taken at varying times and quenched by adding an equal volume of 0.2 M $NaBH_4$, followed by rapid cooling on ice. Samples were stored at -80 °C until electrophoretic analysis. To analyze the DPCs without enzymatic digestion, SDS-urea polyacrylamide gel electrophoresis (PAGE) was used. Samples were mixed with a gel-loading solution containing 95 % (v/v) formamide, 50

mM EDTA and 1% SDS, and analyzed on an 8 cm × 10 cm SDS-urea (7 M) PAGE (4% - 16%). To analyze the DPCs by denaturing PAGE, DPCs were digested with pronase E (0.5 mg/mL, 41 °C overnight), followed by mixing with a 1.5-volume of loading solution containing 95 % (v/v) formamide and 50 mM EDTA for electrophoresis (16% polyacrylamide/bis-acrylamide (19:1), 7 M urea, 38 cm × 30 cm). Gel images were acquired and analyzed as described above. The apparent DNA disappearance rate was obtained by fitting the percent yield of intact DNA to a single-exponential function as described [20]. Percent yields of DPCs and SSBs were fitted to a one-phase decay single-exponential function with 100% set as the initial value.

Thermostability and half-life of TFAM-DPCs

The stability and half-life of DPCs under different temperatures were examined by incubating DPC products resulting from a 15-h reaction of TFAM and AP-DNA under pH 7.4 in the absence of $NaBH_3CN$. The reaction products were then incubated in a dry bath incubator for 1 h under varying temperatures (40°C, 61°C, 66°C, 76°C, 85°C) and quenched with 0.1 M $NaBH_4$. Control reactions were quenched with $NaBH_4$ before heating. The resulting products were quantified without protease digestion by using a gradient (4%-16%) SDS-urea-PAGE gel (7.5 ×10 cm). The half-life of TFAM DPCs was analyzed by incubating the reaction products at 37 °C with an aliquot taken at varying times for SDS-urea-PAGE analysis. The percent yields of DPCs (based on intensity ratios of DPCs/(DPCs+SSBs)) over time were fit to a one-phase decay single-exponential to obtain the half-life.

Half-life of AP-DNA

Without TFAM, 4 μM of AP-DNA was incubated in 20 mM HEPES (pH 7.4), 90 mM NaCl, and 20 mM EDTA under 37 °C for varying times. Reaction aliquots were quenched with an equal volume of 0.2 M $NaBH_4$, followed by rapid cooling on ice. Samples were stored at -80 °C until electrophoretic analysis.

Identification of cross-linking amino acid residues in TFAM DPCs by mass spectrometry

TFAM and AP-DNA reaction products after a 24-h reaction were digested by trypsin in 100 mM Tris-HCl pH 8.0 and 20 mM $CaCl_2$ at 37°C for 12 to 14 h. Samples were purified and analyzed by tandem mass spectrometry according to published procedures [21].

Kinetic simulations

Data from TFAM-mediated AP-DNA cleavage reactions under pH 6.2, 7.4 and 8.7 were fit globally into a multi-step kinetic model (Fig. 2.14A) using KinTek Explorer 7 33. The imported data were concentrations of products (remaining AP-DNA, DPC_{in}, DPC_{cl}, and SSBs) as a function of the reaction time. Initial reactant concentrations were 4 μM for DNA (D+DH in Fig. 2.14A) and 8 μM for TFAM in a 12-h reaction. The observed SSB concentration was defined as the sum of SSB and the SSBH (Fig. 2.14A). Individual rate constants were allowed to fluctuate. FitSpace 34 calculation was used to determine the reliability of the fit, and the lower and upper bounds were obtained by setting the threshold at bound as 0.95. FitSpace confidence contours analysis was used to evaluate whether the simulated data were unique and well-constrained. FitSpace results

were computed for 0.6 Chi^2 threshold limit. The boundary of kinetic parameters was calculated when the Chi^2 threshold was set as 0.95.

MD simulations

Conventional MD simulations (200 ns) were carried out with two systems of TFAM-DNA complexes with a ring-closed AP site or a Schiff base intermediate. The 3D coordinates of TFAM-DNA complexes were obtained from the crystal structure of PDB ID 3TQ6 [45]. XLeap editor was used to remove the nucleobase at the AP_{17} lesion position, build a covalent bond between the lesion and lysine, modify partial charges and generate input files for MD simulations. MD simulations were performed using the Amber18 package with GPU implementation[33]. The protein was parameterized by using Amber Force Field FF14SB and DNA by AMBER bsc1[33–35]. Antechamber was used to calculate the partial charge of the Schiff base intermediate in the system using General Amber Force Field (GAFF)[36]. Both systems were minimized in three steps, hydrogen, side chains, and the entire system. The systems were explicitly solvated using TIP3P water model in a rectangular box of periodic boundaries at 12 Å from any atom and 27 positive counter ions (Na^+) were added to neutralize the overall system charge.

The solvated systems were then minimized, followed by isothermic-isobaric (NPT) ensemble equilibration in 25 K increments from 50 to 298 K, first for water only and then for the entire system, for 200 ps at each temperature. MD trajectories were from over 200 ns at a 1-ps interval with a 2-fs timestep under constant pressure and temperature. Particle mesh Ewald[37] and the SHAKE algorithm[38] were applied for long-range electrostatics and fixed heavy atom–hydrogen bond lengths. The trajectory output

files were processed with PTRAJ to contain 20,000 frames after stripping water molecules and ions, each representing a 0.01-ns timestep[39]. Each trajectory was aligned using the backbone of the first frame and analyzed by using Visual Molecular Dynamics (VMD)[40] and PyMOL[41].

2.3 Results

Design and validation of the Cys-null variant

We have demonstrated that Lys residues of TFAM are essential for catalyzing the DNA cleavage at AP sites via Schiff base chemistry (Fig. 2.1C).[20, 21] The resulting 3′-PUA (after β-elimination) reacts readily with C49 or C246 of TFAM to form (meta)stable DNA-protein cross-links (DPCs) via a Michael addition-type reaction.[21] To probe the role of key Lys and Glu residues without complications from Cys-derived DPCs, we prepared a Cys-null variant of TFAM (C49S/C246S, hereinafter referred to as 2CS), and verified that 2CS maintained similar properties relative to wild-type (wt) TFAM through the following experiments. In terms of DNA-binding activity, 2CS showed a slightly higher affinity with DNA, with a $K_{d,DNA}$ of 2.2 (± 0.2) nM, compared to a $K_{d,DNA}$ of 9.9 (± 1.4) nM for wt TFAM (Fig. 2.2A) based on fluorescence anisotropy measurements. Regarding the AP lyase activity, the rates of AP-DNA disappearance (k_{dis}) were 23 (± 2.3) x 10^{-5} s^{-1} and 18 (± 2.2) x 10^{-5} s^{-1} for 2CS and wt TFAM, respectively (Figs. 2.3A, 2.3B, 2.4A, 2.4B and Table 2.3). The overall percentage yield of DPCs was a bit lower for 2CS (71 %) compared to wt TFAM (83%) in a 12-h reaction. The lower yield of DPCs with 2CS is consistent with the lack of Cys-derived DPCs (Figs. 2.3A and 2.3B). We evaluated the

stability of DPCs resulting from a 15-h reaction with wt TFAM or 2CS under the physiological pH (7.4) and ionic strength conditions. Although the relative abundance of DPCs from both reactions decreased over time, a faster decrease was observed with 2CS (Figs. 2.5A and 2.5C). This can be explained by the presence of imine-based DPCs formed with 2CS, which are less stable than the Michael-type DPCs formed with wt TFAM.[21] Fitting the decrease of the DPC abundance over time to a single exponential decay function resulted in a half-life ($t_{1/2}$) of 7 h for 2CS (Fig. 2.3C) and 43 h for wt TFAM (Fig. 2.3D). Consistent with the poor thermostability of the Schiff base, DPCs derived from 2CS were more sensitive to heating (Fig. 2.5B,D). For example, the relative abundance of DPCs from 2CS was approximately 8% at 61 ºC (Fig. 2.3E), whereas the relative abundance was approximately 20% for wt TFAM (Fig. 2.3F).

To verify that 2CS maintains the local interactions near the AP lesion in TFAM-DNA complexes, we identified amino acid residues of TFAM cross-linked to the AP lesion using tandem mass spectrometry (Fig. 2.6, Tables 2.4 and 2.5). Under *in situ* trapping by $NaBH_3CN$, the Schiff base intermediates formed between the AP lesion and a proximal Lys were captured. Mass spectrometry data show that the AP lesion cross-links primarily with K186 of 2CS. The relative abundance of K186-conjugated DPCs was 87% on the basis of semi-quantification using integrated peak areas. The abundance correlates nicely with an abundance of 85% with wt TFAM.[21] In the absence of $NaBH_3CN$, the AP lesion was cross-linked to a number of Lys residues, including K111 (36% relative abundance), K76 (26%), and K69 (15%). Interestingly, K111 also locates in a K111/E112 cluster in the primary sequence, as shown in Figure 2.1B. These results do not abrogate

the importance of K186 because reactions in the presence of $NaBH_3CN$ should capture the predominant conformation in the initial phase of the reaction, whereas reaction products in the absence of $NaBH_3CN$ may represent thermodynamically stable products after reversible reactions with K186. The observed products are consistent with the conformational dynamics of TFAM-DNA complexes reported by others[42] and us.[32] For example, the TFAM-bound complex can undergo butterfly-like motions with the two HMG domains.[33] Together, these data confirm that similar local interactions were maintained with 2CS relative to wt TFAM and that 2CS is a suitable variant to probe the role of Glu in TFAM-mediated AP lyase reactions.

Probing the role of Glu using TFAM variants

The high abundance of Glu residues and their proximity to Lys residues prompted us to investigate their roles in TFAM-mediated DNA strand scission at AP sites. We intended to characterize the formation time course of DPC_{in} and DPC_{cl} using 2CS variants with and without a Glu residue. DPC_{in} denotes DNA-protein cross-links (DPCs) with the intact DNA oligomer; DPC_{cl} denotes DPCs with a cleaved DNA oligomer. To quantify DPC_{in} and DPC_{cl}, we optimized the protease digestion procedures and separated two types of DPCs using denaturing PAGE (Fig. 2.7). Using Pronase E, which contains a mixture of proteolytic enzymes from *Streptomyces griseus*, we were able to separate DPCs based on their migration relative to the AP-DNA substrate. Peptide-DNA cross-links migrating slower than AP-DNA corresponded to DPC_{in}, and products migrating faster than AP-DNA but slower than SSB corresponded to DPC_{cl}, as shown in Figure 2.7.

The separation of the two types of DPCs allowed us to follow the time-course formation of DPC_{in} and DPC_{cl} unambiguously.

Given the importance of K186 in TFAM-catalyzed AP-DNA cleavage, we chose to investigate the role of E187 in the reaction. We hypothesized that E187 could promote β-elimination by abstracting the α-H as a general base (directly or via a water molecule, as shown in Figure 2.1C), stabilizing the Schiff base, or both. To test this, we prepared the TFAM 2CS/E187A (2CSEA) variant and compared product yields and reaction rates with those from 2CS in TFAM-mediated AP-DNA scission under physiology pH and ionic strength conditions. In the presence of $NaBH_3CN$ (N reactions), DPC_{in} and DPC_{cl} were trapped due to the rapid reduction of imines under near neutral pH,[43] as observed in Figures 2.4B and S2C (left panels). The relative abundance of DPC_{in} and DPC_{cl} depends on the rate of β-elimination relative to the reduction of imine. As summarized in Table 2.3, although the total yields of DPCs (DPC_{in} and DPC_{cl}) were nearly identical in a 12-h reaction, 2CSEA resulted in a higher yield of DPC_{in} (89 % for 2CSEA vs. 76% for 2CS) and a lower yield of DPC_{cl} (11% for 2CSEA vs. 23% for 2CS), supporting a role of E187 in promoting β-elimination. The increased accumulation of DPC_{in} was evident with 2CSEA in gel electrophoretic analysis (compare the left panels of Figs. 2.4B and 2.4C). In the absence of $NaBH_3CN$ (X reactions), reactions undergo steps 1 through 3 (Fig. 2.1C), generating DPC_{in}, DPC_{cl}, and SSBs. With both 2CS and 2CSEA, the formation of DPC_{in} peaked at the first 10 min of the reaction (Fig. 2.8A), followed by conversion to DPC_{cl} and SSBs (Figs. S2B and S2C, right panels). Notably, compared to 2CS, a clear increase in the accumulation of DPC_{in} was observed in gel electrophoresis analysis with

2CSEA (Figs. 2.4B and 2.4C, right panels). The accumulation of DPC_{in} was more apparent when comparing the ratios of relative abundance of DPC_{in}/DPC_{cl} between 2CS and 2CSEA (Fig. 2.8A). Overall, these data demonstrate that E187 facilitates β-elimination in AP-DNA cleavage.

Further, the role of E187 in β-elimination was implicated when the rates of AP-DNA disappearance (k_{dis}) and DPC formation were compared. k_{dis} is a comprehensive rate constant encompassing contribution from all steps in the reaction (Fig. 2.1C), whereas the rate of DPC formation reflects the kinetics of several sub-steps. In the presence of $NaBH_3CN$, $k_{dis,N}$ is contributed primarily by steps 1 and 4 and, to a lesser extent, by steps 2, 3, and 5. As shown in Table 2.3 and Figure 2.9, 2CS yielded a $k_{dis,N}$ of 23 ± 2.3 ($\times 10^{-5}$ s^{-1}), and 2CSEA yielded a $k_{dis,N}$ of 44 ± 2.2 ($\times 10^{-5}$ s^{-1}). Considering that β-elimination promotes the forward equilibrium, the 2-fold higher k_{dis} with 2CSEA can be partly attributed to a compromised β-elimination reaction. Because the ratio of $k_{dis,N}/k_{dis,X}$ contains contributions from steps after the Schiff base formation in the denominator, a slower β-elimination step would result in a higher $k_{dis,N}/k_{dis,X}$ ratio. Indeed, the ratios were 4.3 for 2CS and 8.6 for 2CSEA (Table 2.6, pH 7.4), in keeping with slower β-elimination in the absence of E187. Regarding the formation rate of DPC_{in} ($k_{f,in}$) it contains mainly kinetic contributions from steps 1 and 4. Compared to 2CS, a 2-fold faster $k_{f,in}$ was observed with 2CSEA (Table 2.7, 2CS and 2CSEA with AP_{17}). With both 2CS and 2CSEA, the formation rates of DPC_{in} are comparable to k_{dis}, indicating the *in situ* trapping of DPCs by $NaBH_3CN$ was efficient (Table 2.7, 2CS and 2CSEA with AP_{17}). DPC_{cl} was a major product in the absence of $NaBH_3CN$, whereas only a minimal

level of DPC_{cl} formed in the presence of $NaBH_3CN$. Therefore, we reason that Schiff base formation is relatively slow and β-elimination is relatively fast (but slower than reductive amination). This notion is supported by published kinetic data regarding the Schiff base formation[44] and $NaBH_3CN$-catalyzed reductive amination in aqueous solutions.[34]

To verify these observations were indeed due to specific TFAM-DNA interactions, we carried out a control experiment with a different substrate (AP_{20}, sequence shown in Fig. 2.1D) containing the AP lesion 3 nt away from (5′ of) that of AP_{17}. Because the AP position in AP_{20} is away from the K186/E187 cluster in TFAM-DNA complexes, it is anticipated that the catalytic effects of these residues would diminish. As shown in Table 2.7 and Figures 2.10 and 2.11, in the presence of $NaBH_3CN$, $k_{dis,N}$ was much lower with AP_{20} than that of AP_{17}, with both 2CS and 2CSEA, consistent with the important roles of K186 and E187 in TFAM-mediated AP-DNA cleavage. Unlike the 5- and 9-fold difference between $k_{dis,N}$ and $k_{dis,X}$ with AP_{17} and 2CS and 2CSEA, $k_{dis,N}$ and $k_{dis,X}$ obtained with AP_{20} were nearly identical with both TFAM variants. These observations reaffirm the catalytic role of the K186/E187 cluster in TFAM-mediated AP-cleavage reactions. Importantly, unlike the 2-fold greater $k_{dis,N}$ for AP_{17} with 2CSEA as compared to that of 2CS, k_{dis} values obtained with AP_{20} were comparable (2CSEA vs. 2CS, with or without $NaBH_3CN$), reinforcing the role of E187 in β-elimination. Taken together, these experiments with site-specific AP-DNA substrates and TFAM variants demonstrate the role of E187 unequivocally in promoting the β-elimination step of the TFAM-assisted AP-lyase reaction.

AP-DNA cleavage under different pH conditions

Considering that pH could affect the protonation of solvent-exposed K186 and E187, as well as the Schiff base intermediates, we obtained reaction rates under two additional pH conditions (6.2 and 8.7) with AP_{17}. Although the physiological pH is approximately 8 in the mitochondria matrix,[45] the local pH could vary inside the nucleoid. In spite of the varying $K_{d,DNA}$ of TFAM under different pH conditions (Fig. 2.12C), AP_{17} was saturated by TFAM completely under the current assay conditions (4 μM of DNA and 8 μM of TFAM) based on calculations using a quadratic equation.[46] Even with the highest $K_{d,DNA}$ (~400 nM) under pH 8.7, the calculated TFAM-bound AP_{17} was greater than 92% of the total DNA in the assay. Therefore, the impact of DNA binding on the reaction rates was negligible. In terms of k_{dis} of AP_{17} (with or without $NaBH_3CN$), the rate increased with pH with both 2CS and 2CSEA (Table 2.6), likely due in part to the greater extent of deprotonation of key lysine residues under basic conditions, which enhances the nucleophilicity of Lys. When comparing $k_{dis,N}/k_{dis,X}$ between 2CS and 2CSEA under different pH conditions (Fig. 2.13A), we observed higher $k_{dis,N}/k_{dis,X}$ ratios under pH 6.2 for 2CSEA, similar to that observed at pH 7.4. However, under pH 8.7, the $k_{dis,N}/k_{dis,X}$ ratios were comparable between 2CS and 2CSEA, mainly due to the dramatic increase of $k_{dis,X}$ with both TFAM variants. The drastic increase of $k_{dis,X}$ under pH 8.7 suggest an acceleration of the rate-determining step, presumably Schiff base formation. In addition, under pH 6.2 and 7.4, 2CS and 2CSEA yielded comparable $k_{dis,X}$ values in the absence of $NaBH_3CN$ (Table 2.6, Fig. 2.13B). By contrast,

under pH 8.7, a 4-fold difference in $k_{dis,X}$ was observed between 2CS and 2CSEA, indicating that other factors contributing factors may compensate for the loss of Glu (e.g., the fraction of the deprotonated Schiff base).

Because pH affects the rate of spontaneous β-elimination of AP sites (Fig. 2.12A and 2.12B), we compared the half-life of naked AP_{17} with that of TFAM-complexed AP_{17} under different pH conditions. The fold reduction in $t_{1/2}$ reflects the net effect of TFAM variants on the stability of AP sites. As shown in Table 2.8, $t_{1/2}$ of AP sites in free DNA decreased at higher pH conditions, consistent with faster β-elimination under basic environments. When AP_{17} was complexed with TFAM, $t_{1/2}$ was reduced by 2 orders of magnitude, with the highest fold reduction (173-fold) at pH 8.7 and approximately 100-fold at pH 6.2 and 7.4. Although the spontaneous β-elimination occurs faster under basic pH, the 173-fold reduction in $t_{1/2}$ of AP argues for a catalytic effect of TFAM. The faster reaction under basic pH could arise from an increase in the fraction of deprotonated Lys side chains.

Regarding the overall DPC yields and the relative abundance of DPC_{in} and DPC_{cl}, product profiles under pH 6.2 were comparable to those under pH 7.4 (Table 2.9). Under pH 8.7, a number of differences were observed. First, in the presence of $NaBH_3CN$, a significant increase in the yield of DPC_{cl} was observed, compared to those observed under pH 7.4 or 6.2. Under this condition, 2CSEA led to an increase in the DPC_{in} and a decrease in the yield of DPC_{cl}. Second, in the absence of $NaBH_3CN$, compared to 2CS, a dramatic increase in the yield of DPC_{cl} was observed. This is in contrast to the basal level of DPC_{cl} produced without $NaBH_3CN$ in the case of both 2CS and 2CSEA under pH 6.4

or pH 7.4. The yields of DPC_{cl} were 56% for 2CS vs. 29% for 2CSEA, in keeping with the role of E187 in β-elimination. The overall faster reaction under pH 8.7 could be partly owing to faster Schiff base formation due to an increased amount of deprotonated form of Lys under pH 8.7. Assuming the pKa of the solvent-exposed Lys is near 10, shifting pH from 7.4 to 8.7 would increase the fraction of the deprotonated Lys side chains by approximately 100-fold. On the other hand, E187 likely remained predominantly in the deprotonated form, and had not a significant impact on the reaction rates under the current conditions. Overall, the difference in kinetic parameters and product profiles under different pH conditions support the importance of Lys residues in these reactions.

Kinetic simulations support the role of E187 in β-elimination

To compare the rate constants of the β-elimination step between 2CS and 2CSEA directly, we fit data under three pH conditions to a simplified kinetic model using KinTek Explorer software.[47] Kinetic simulations have been shown to be useful in extracting individual rate constants, which would otherwise be difficult to isolate experimentally.[46–48] Because of the lack of data to constrain the noncovalent binding and dissociation of TFAM-DNA complexes, these steps were embedded in the Schiff base formation (Fig. 2.14A, step 1) and the dissociation from DPC_{cl} (Fig. 2.14A, step 6). On the basis of the reported on-rate of TFAM-DNA interactions, the rate of step 1 should not be limited by noncovalent binding or sliding.[49] The simplified kinetic model of reactions in the presence of $NaBH_3CN$ is shown in Figure 2.14A. The kinetic model in the absence of $NaBH_3CN$ is the same as that in Figure 2.14A, except without steps 8 and 9. Global data

fitting demonstrates that the proposed kinetic model correlates largely with our experimental data (Fig. 2.14B and Fig. 2.15). As summarized in Table 5 and Table S6, although not all the rate constants were well constrained due to the lack of data to define all the sub-steps, kinetic parameters of several key steps were well defined, i.e., steps 1, 4 and 6 (Fig. 2.14A). Overall, the Schiff base formation was rate-limiting for both 2CS and 2CSEA, supporting our earlier conclusion. In the presence of $NaBH_3CN$, β-elimination occurred faster than the Schiff base formation with a rate constant comparable to that of the reverse rate of step 1 (Table 2.10). In the absence of $NaBH_3CN$, the reverse rate constants of Schiff base formation and β-elimination were extremely small, indicating that the forward reactions of both steps were favored. Although the reverse rate constants of β-elimination were greater in the presence of $NaBH_3CN$, the rapid reduction by $NaBH_3CN$ offset the effect and drove the equilibrium forward, as evidenced by a k_6 (8500 – 9600 h^{-1}) that is 2-orders of magnitude higher than k_{-4} (58 – 59 h^{-1}).

Importantly, the rate constants of β-elimination for 2CSEA are several folds lower than that of 2CS (4-fold with $NaBH_3CN$ and 2-fold without $NaBH_3CN$) based on their best-fit values, supporting the role of E187 in β-elimination. Further, we carried out confidence contour analysis to estimate the errors associated with simulations and to reveal complex relationships between the simulated parameters[50]. The resulting confidence contours showed that the simulated rate constants were well constrained by the data in general, especially for steps 1, 4 and 6 (see lower and upper bounds in Table 2.10 and Table 2.11). With or without $NaBH_3CN$, the range of simulated data for β-elimination with 2CS is greater than that of 2CSEA (compare lower and upper bounds in

Table 2.10), affirming a faster β-elimination with 2CS. Overall, kinetic simulations allowed the direct comparison of rate constants with 2CS and 2CSEA. The data support the role of E187 in facilitating β-elimination and demonstrate that Schiff base formation is rate-limiting in TFAM-mediated AP lyase reactions.

Conformational dynamics of the AP sites and E187 in TFAM-DNA complexes

The dynamic conformations of AP sites in duplex DNA and protein-bound complexes have been well documented by web-lab approaches[51,52] and MD simulations.[53] The AP lesion can adopt an intrahelical or extrahelical conformation, depending on the local sequence, its complementary nucleobase, and the associated protein (see [43] and references therein). To probe the conformational dynamics of AP sites in TFAM-DNA complexes for steps 1 and 2 of the proposed mechanism (Fig. 2.1C), we carried out MD simulations using modified models based on the TFAM-DNA co-crystal structure (PDB: 3TQ6).[54] We built the AP lesion in AP_{17} as a closed 5-membered sugar ring based on its favored closed ring structure. We started the MD simulations with the AP lesion in its intrahelical conformation (Fig. 2.10A). The motion of the AP lesion was evident in the output trajectory (Fig. 2.17A). Although the intrahelical conformation of the AP site was maintained for the first 90 ns of 200 ns simulations, an extrahelical conformation was adopted for the remaining time (approximately 55% of the time). The rotation of the AP lesion outside the duplex structure likely facilitates the Schiff base formation by shortening the distance between the carbonyl group and the ε-amino group of K186 with a few occasions that the distance was as short as approximately 4.0 Å (Fig. 2.17B). L182,

one of the two intercalating residues (the other being L58) in TFAM-DNA complexes [45], maintained its position in the complex (data not shown), which may help stabilize the conformation with the moiety rotated outside the helical structure. Therefore, our results demonstrate that the AP site maintains its dynamic characteristics in TFAM-DNA complexes and the transition to the extrahelical conformation likely facilitates the Schiff base formation.

To explore the interactions between E187 and the Schiff base, we built a model containing the covalently linked Schiff base intermediate formed between the C1′ atom of the AP lesion and the ε-N atom of K186 using a frame from a previous trajectory when the AP ring is proximal to K186. We carried out MD simulations using this system and observed the conformational flexibility of E187 and the Schiff base intermediate. The side chain of E187 was very flexible and observed to move towards the intermediate multiple times over the trajectory (Fig. 2.18). The farthest distance between the proximal O atom of the E187 side chain and the C1′ hydrogen was approximately 15.2 Å (Fig. 2.16B), and the closest distance was 6.9 Å (Fig. 2.16B). Such distances were too far for direct hydrogen abstraction by the carboxylate group to occur, it is likely that the reaction is mediated by a water molecule as proposed in Figure 2.1C. Together, data from MD simulations support the proposed mechanism and provide important insights into the conformational flexibility of AP sites and E187 in TFAM-DNA complexes.

2.4 Discussion

Critical to the repair of ubiquitous AP sites or other nucleobase modifications are the enzymes with AP-lyase activities. AP endonucleases are best-studied enzymes specific to AP sites, incising the DNA backbone at the 5′-side of the deoxyribose group and leaving a 5′-deoxyribose phosphate (dRp) moiety on one of the cleaved strands.[55] AP endonucleases function with monofunctional glycosylases in base excision repair (BER).[56] Equally important are bifunctional DNA glycosylases with both DNA glycosylase and AP-lyase activities. These enzymes catalyze the β-elimination reaction of AP sites upon the enzymatic cleavage of damaged nucleobases.[47] Importantly, the AP-lyase activity is not limited to these well-studied enzymes. A body of work by the Greenberg and Gates laboratories has shown that free amino groups in DNA-binding proteins and nucleobases can catalyze similar reactions.[57–60]For example, Greenberg and associates have demonstrated that Lys residues of histone tails can promote strand scission at AP sites in reconstituted nucleosome particles.[48, 49] Gates and associates have shown that *in vitro* amino groups of the nucleoside 3′ or 5′ of the nucleoside opposing the AP lesion can catalyze similar reactions in duplex DNA substrates with a variety of DNA sequence contexts, and that biological amines, such as spermine, can accelerate the reaction.[59–62]

Similarly, we have demonstrated that, *in vitro* and *in cellulo*, TFAM, a key DNA-packaging factor in mitochondria, promotes AP-DNA scission via Schiff base chemistry.[20, 21] The activity differs from the APE1-catalyzed AP-DNA cleavage and likely complement APE1 repair given the high abundance of TFAM. Besides, the TFAM-

mediated cleavage also forms TFAM-DPCs involving Cys residues (Michael-type adduct) and Lys residues (Schiff base).[21] Given the heterogeneous characteristics of TFAM-DPCs, we prepared the Cys-null variant of TFAM to probe the role of key Lys and Glu residues and the properties of resulting DPCs without interference from Cys-derived DPCs. Our kinetic and mass spectrometric analyses demonstrate that, compared to wt TFAM, 2CS maintains similar interactions with AP-DNA and is a suitable variant for our experimental purposes. Besides, mass spectrometry data revealed additional Lys residues (e.g., K111) that can participate in the reaction after the AP lesion reacts reversibly with K186. By contrast, wt TFAM cross-links with AP-DNA primarily at C49. Stability analysis of 2CS-derived DPCs allowed comparison with other imine-based DPCs directly. 2CS-DPCs have a $t_{1/2}$ of 7 h under physiological conditions, comparable to a $t_{1/2}$ of 10-14 h of AP-DNA-peptide cross-links derived from histone H2 and H4 proteins,[63] and much more stable than 5-formylcytosine-histone DPC ($t_{1/2}$ = ~1.8 h)[64] and 5-formyluracil-histone DPC ($t_{1/2}$ = ~28 min).[65] By contrast, wt TFAM-DPCs formed predominantly via Michael-additions have a $t_{1/2}$ of 43 h, even more stable than histone-DPCs. The biological significance of the relatively stable TFAM-DCPs warrants further investigation.

Intriguingly, TFAM has a higher abundance of Glu compared to its average abundance in the human proteome. In addition, more than half of the Glu residues are clustered with Lys residues in TFAM, making them prime candidates as a general base for H-abstraction at the C2′ carbon directly or via a water molecule, or acting as a counterion of the protonated Schiff base. These roles of carboxylate side chains have

been documented for key residues in bifunctional glycosylases and other DNA repair enzymes. For example, E23 of T4 endonuclease V stabilizes the Schiff base intermediate and also potentially participates in β-elimination.[27] T4 endonuclease V is a bifunctional glycosylase from bacteriophage T4 that removes the pyrimidine dimer DNA adduct. On the other hand, histone H2B and H4 tails catalyze AP-lyase reactions despite the lack of Glu, Asp, and His residues, which results in a rate-limiting β-elimination step.[66] The introduction of Glu, Asp, and His proximal to key Lys residues increases the overall rate of the AP-DNA scission.[57] On the contrary, the high abundance of Glu in TFAM likely results in a fast β-elimination step, rendering Schiff base formation rate-limiting. Although further studies are needed to clarify the effects of other Glu on the aforementioned steps, our data demonstrate unambiguously that E187 facilitates β-elimination with defined AP-DNA substrates.

Aside from the amino acid compositions of TFAM, the dynamics of AP lesions contribute to the kinetics of the AP-lyase reaction. On the basis of MD simulation data, the extrahelical conformations were observed in the second half of the trajectory, suggesting that the conformational change may partially limit the Schiff base formation. The extrahelical conformation of AP sites has been observed in co-crystal structures of several other repair enzymes, including uracil-DNA glycosylase,[67] alkylated-base glycosylase AlkA,[68] and APE1.[69] The conformational flexibility of AP sites may be enhanced by L182, one of the two intercalating residues (the other being L58) in TFAM-DNA complexes. These intercalating residues play a major role in facilitating a U-turn DNA structure for transcription initiation and DNA compaction.[45] L182 may promote the

conformational flexibilities of the AP lesion by stabilizing the local duplex DNA structure, analogous to DNA-intercalating residues in other base-flipping glycosylases.[70,71] In addition, the conformational flexibility of the E187 side chain may facilitate the reaction by shortening the distance between E187 and the C2′ position.

mtDNA is turned over rapidly compared to nuclear DNA, with a reported half-life in a matter of days.[13] Recently, mtDNA degradation has also emerged as an important DNA damage response mechanism.[2, 4, 7, 8]. The induction of AP sites in mitochondria leads to a rapid decline in mtDNA copy number without increasing the mutation load.[72] The high abundance of Lys and Glu residues in TFAM supports the role of TFAM in facilitating strand scission at ubiquitous AP sites. Although the observed rate of AP-DNA cleavage is much slower than other DNA repair enzymes, the abundance of TFAM in nucleoids and our detection of elevated TFAM-DPCs upon inducing mitochondrial AP sites in HeLa and HEK293 cells[21, 22] argue the involvement TFAM in processing AP sites in mitochondria. The strand scission at AP sites converts AP lesions to more deleterious "roadblocks" in the forms of DPCs and SSBs to various mtDNA transactions, which could potentially serve as signals for recruiting additional factors (e.g., DNA nucleases) or for purifying selection against damaged mtDNA molecules. The rapid AP-DNA degradation supports the disposable characteristic of mtDNA[7] and a proposed role of mtDNA as a cellular genotoxic stress sentinel.[3]

In sum, we have demonstrated the role of E187 in facilitating β-elimination during TFAM-mediated AP-lyase reactions. Although E187 is a representative residue proximal to a key Lys (K186), the abundance of Glu in TFAM and the large fraction of

Glu clustered with Lys suggest a general role of Glu in facilitating AP-lyase reactions. Unlike specific Glu located in the enzyme active site, the extent of contribution of different Glu residues likely varies based on the local interactions and the conformational dynamics of the AP lesion in a given sequence context in TFAM-DNA complexes.

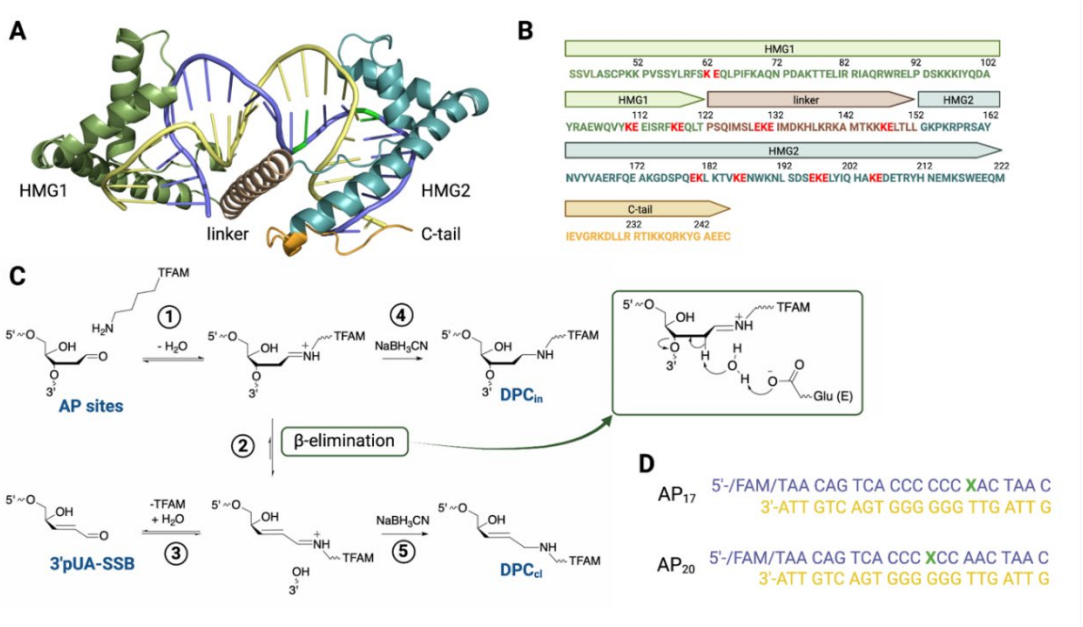

Figure 2.1. Structural basis and proposed mechanism of TFAM-facilitated AP-DNA strand scission. (**A**) The crystal structure of TFAM (PDB:3TQ6) complexed with a DNA duplex substrate containing the light-strand promoter (LSP) sequence. Two high-mobility group (HMG) domains are in green (HMG1) and cyan (HMG2); the linker region is in light pink; the C-terminal tail is in yellow; two abasic site positions are in green (DNA sequences in D). (**B**) The primary sequence of TFAM with Glu-Lys clusters is highlighted in red. (**C**) Proposed mechanisms of TFAM-facilitated AP-DNA strand scission and the role of Glu acting as a general base to abstract the α-proton of the Schiff base in the β-elimination step (an optional water molecule is included). Alternately, Glu can also serve as a counter ion to stabilize the Schiff base (not shown). Major products are labeled in blue. DPC_{in} denotes DNA-protein cross-links (DPCs) with the intact DNA oligomer; DPC_{cl} denotes DPCs with a cleaved DNA oligomer; 3′pUA-SSB denotes the DNA single-strand break product with 3′-phospho-α,β-unsaturated aldehyde residue. (**D**) AP-DNA substrates (AP_{17} and AP_{20}) containing a site-specific modification. X indicates an AP lesion, converted from a deoxyuridine (dU) precursor using UDG.

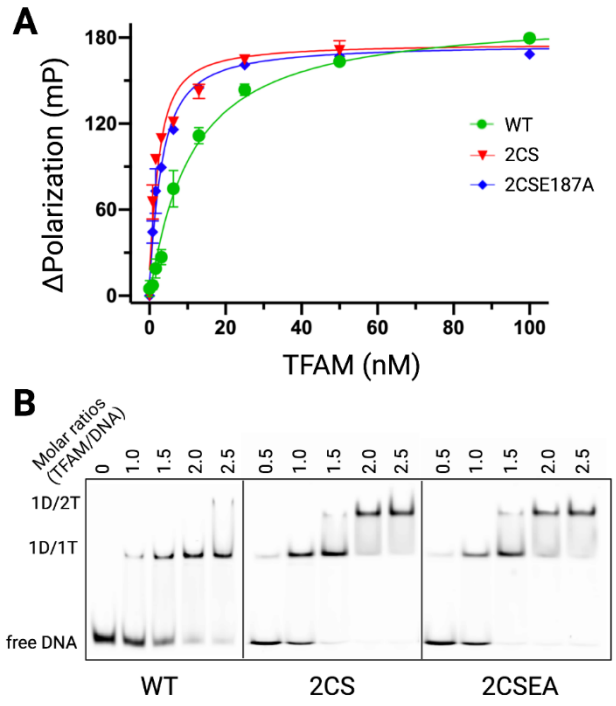

Figure 2.2. TFAM-DNA binding activities from fluorescence polarization and electrophoretic mobility shift assays (EMSA). (**A**) fluorescence polarization assays equilibrium to determine the dissociation constant ($K_{d,DNA}$) for TFAM variants with AP_{17}. $K_{d,DNA}$ was 9.9 (± 1.4) nM for wt TFAM, 1.5 (± 0.1 nM) for 2CS, and 2.2 (± 0.2) nM for 2CSEA. Data were average values, and errors were the standard deviation (n=3). (**B**) Representative gel images from EMSA. Assays contained 20 mM HEPES (pH 7.4), 90 mM NaCl, 20 mM EDTA, 4 μM duplex AP_{17} precursor substrate with dU, and varying concentrations TFAM. D, DNA; T, TFAM.

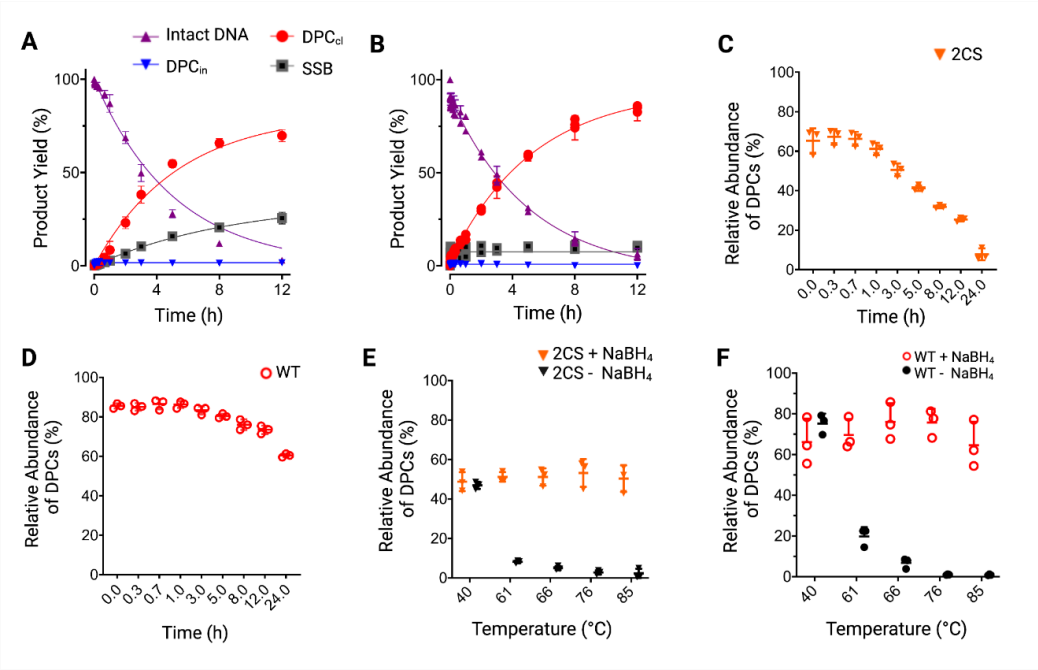

Figure 2.3. Comparison of wt TFAM and 2CS in AP-DNA cleavage reactions and the stability of the resulting DPCs. Quantification of AP-DNA, DPC, and SSB in TFAM-mediated AP-DNA strand scission reactions with (**A**) 2CS and (**B**) wt TFAM. Representative gel images are shown in Fig. 2.4. The stability of TFAM-DPCs with (**C**) 2CS and (**D**) wt TFAM. Fitting the change of relative abundance of DPCs with time to a single exponential decay equation resulted in a half-life of 7 h for 2CS and 43 h for wt TFAM. The relative abundance is calculated based on the intensities of DPCs divided by the sum of the intensities of DPCs and SSBs. The thermostability of DPCs formed in reactions with (**E**) 2CS or (**F**) wt TFAM. DPCs used in (C) through (F) were from a 15-h reaction with TFAM and AP-DNA without $NaBH_3CN$. Representative gel images are shown in Fig. 2.5.

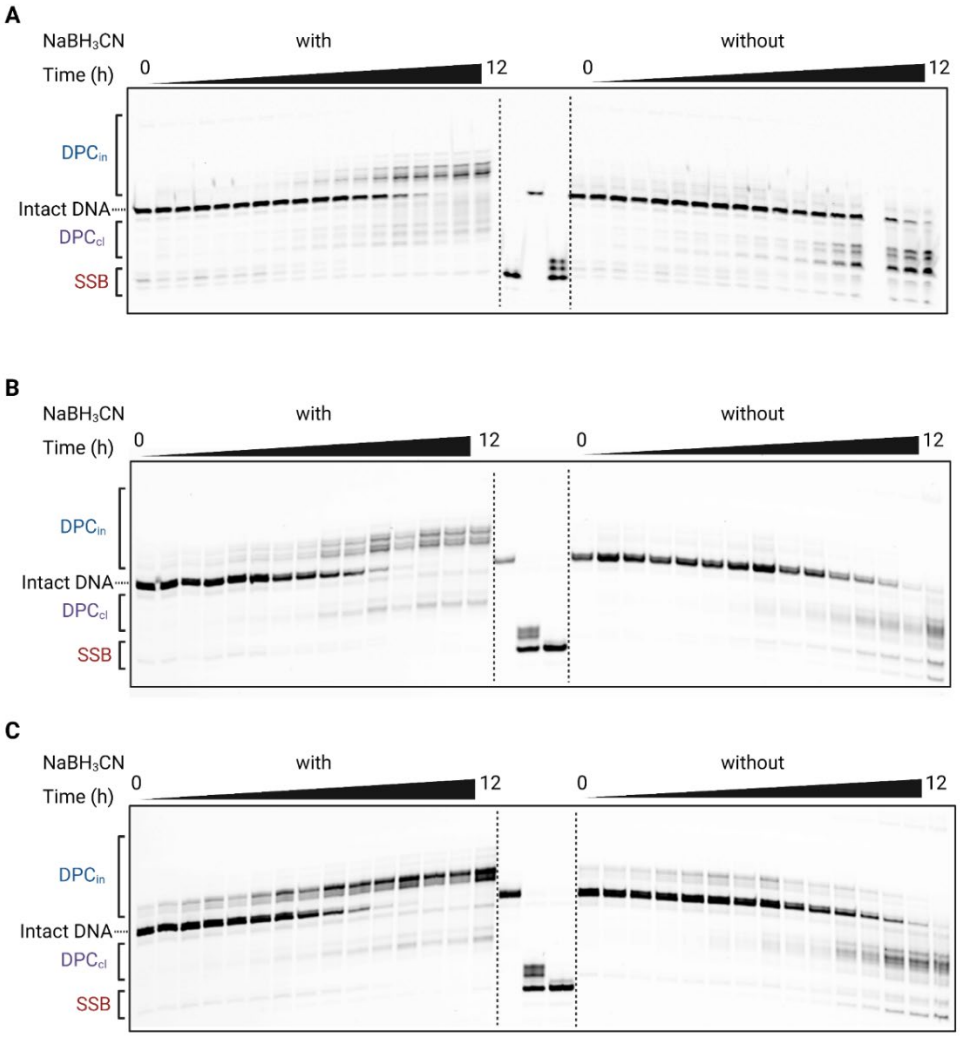

Figure 2.4. Representative gel images of TFAM-induced DPCs and SSBs formation with AP_{17}. DPC was converted to peptide-DNA cross-links using pronase E digestion before electrophoretic analysis. Reactions contained 4 μM AP_{17}, 8 μM TFAM, 20 mM HEPES (pH 7.4), 90 mM NaCl, and 20 mM EDTA at 37 °C. An aliquot was quenched with an equal volume of 0.2 M $NaBH_4$ at varying times. The quenched samples were digested by Pronase E (0.5 mg/mL) at 41 °C for 12 h and then mixed with 95 % (v/v) formamide/50 mM EDTA solution for gel electrophoresis. (**A**) AP_{17} with wt TFAM. (**B**) AP_{17} with 2CS. (**C**) AP_{17} with 2CSEA.

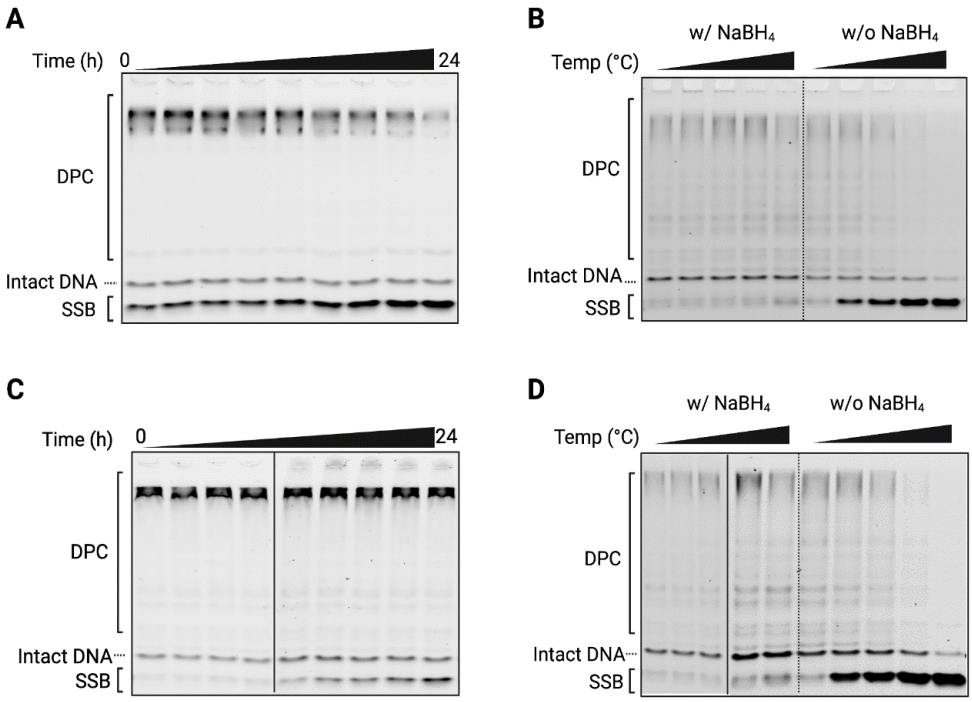

Figure 2.5. Representative gel images for the characterizations of the half-life and thermostability of TFAM-DPCs with 2CS and wt TFAM. DPCs were prepared from 15-h reactions containing 4 μM AP_{17}, 8 μM TFAM, 20 mM HEPES (pH 7.4), 90 mM NaCl, and 20 mM EDTA at 37°C. (**A**) and (**C**) are gel images for the characterization of the half-life and 2CS and wt TFAM, respectively. Reaction products were incubated at 37°C for varying times and then treated with $NaBH_4$ before gel electrophoresis. (**B**) and (**D**) are thermostability assays for 2CS (**B**) and wt TFAM (**D**). DPC products were treated with or without $NaBH_4$, and then each set of samples was incubated at 40, 61, 66, 76, and 85°C for 1 h. All samples were quenched with $NaBH_4$ followed by mixing with the gel loading solution containing 95 % (v/v) formamide, 50 mM EDTA and 1% SDS. Samples were analyzed by 8 × 10 cm SDS-urea (7 M) PAGE (4% -16%).

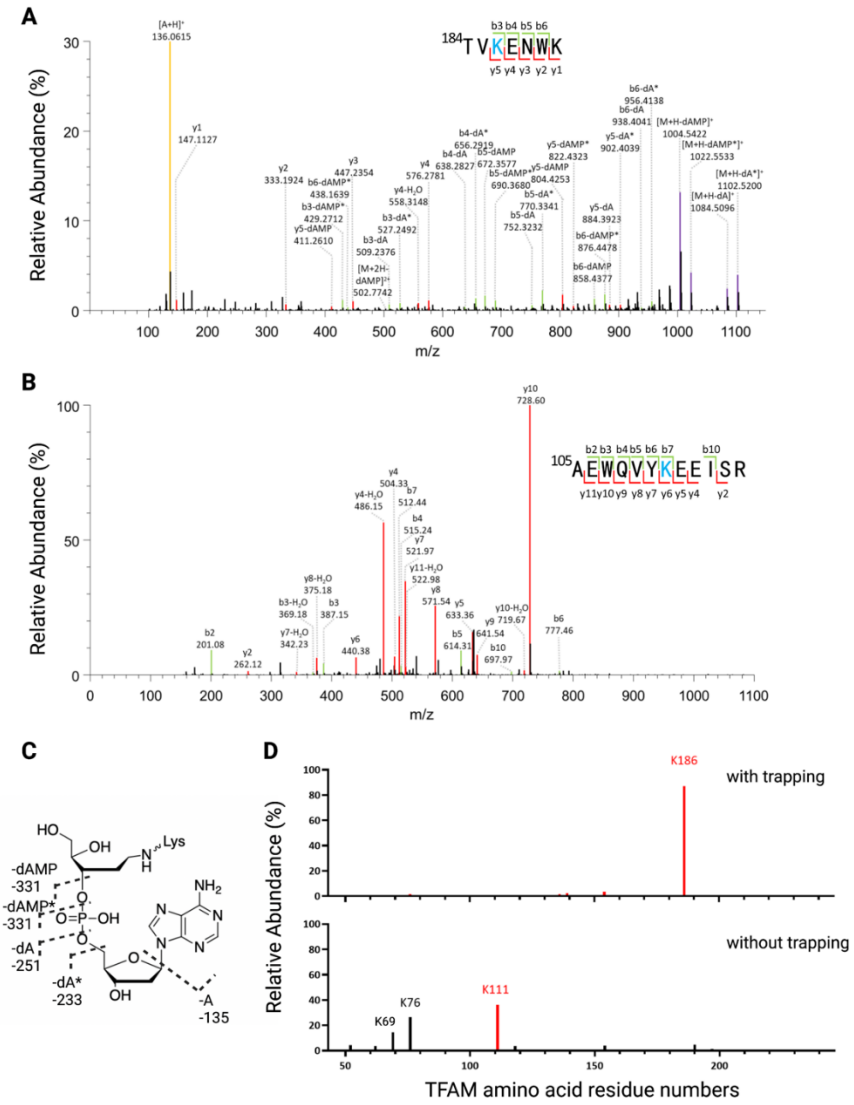

Figure 2.6. Identification of cross-linked amino acid residues in TFAM-DPCs by tandem mass spectrometry. (**A**) MS2 spectrum of a representative TFAM 2CS peptide with K186 cross-linked via a reduced Schiff base with an AP residue in the presence of $NaBH_3CN$. Precursor ion, m/z 445.8757, z=3. Peptide sequence TV<u>K</u>ENWK (the underlined K contains a mass adduct 431 from the AP moiety and a neighboring dA residue). (**B**) MS2 spectrum of a representative TFAM 2CS peptide cross-linked at K111 in the absence of $NaBH_3CN$. Precursor ion, m/z 552.6135, n=3. Peptide, AEWQVY<u>K</u>EEISR (the underlined K contains a mass adduct 118 from the AP residue after β-elimination). (**C**) Proposed fragmentation pattern of mass adduct 431. (D) Relative abundance of observed cross-linked residues of TFAM 2CS with AP_{17}. Major residues were K186 (87%) in the presence of chemical trapping and K111(36%), K76 (26%) and K69 (15%) without trapping. Complete lists of observed peptides are in Tables 2.4 and 2.5.

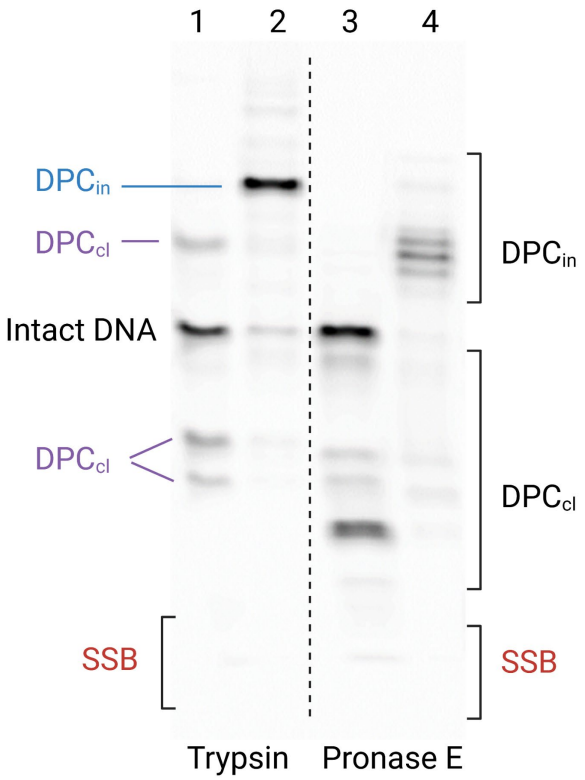

Figure 2.7. Representative gel image from trypsin and pronase E digestion of TFAM-DPCs from AP_{17} reactions. Lanes 1 and 3 were from reactions in the absence of $NaBH_3CN$. Lanes 2 and 4 were from reactions in the presence of $NaBH_3CN$. The assignment of DPC_{cl} and DPC_{in} was achieved by a trypsin-proteinase K cocktail, as discussed in ref. 23 of the main text. In the presence of $NaBH_3CN$ (compare lanes 1 and 3), pronase E digestion converted DPCs to peptide-DNA cross-links migrating faster than the substrate, with no product bands migrating slower than the substrate. In the absence of $NaBH_3CN$ (compare lanes 2 and 4), pronase E digestion converted DPCs to peptide-DNA cross-links migrating slower than the substrate. Therefore, for pronase E treated samples, bands above the intact DNA were assigned as DPC_{in}, and bands below the intact DNA were assigned as DPC_{cl}.

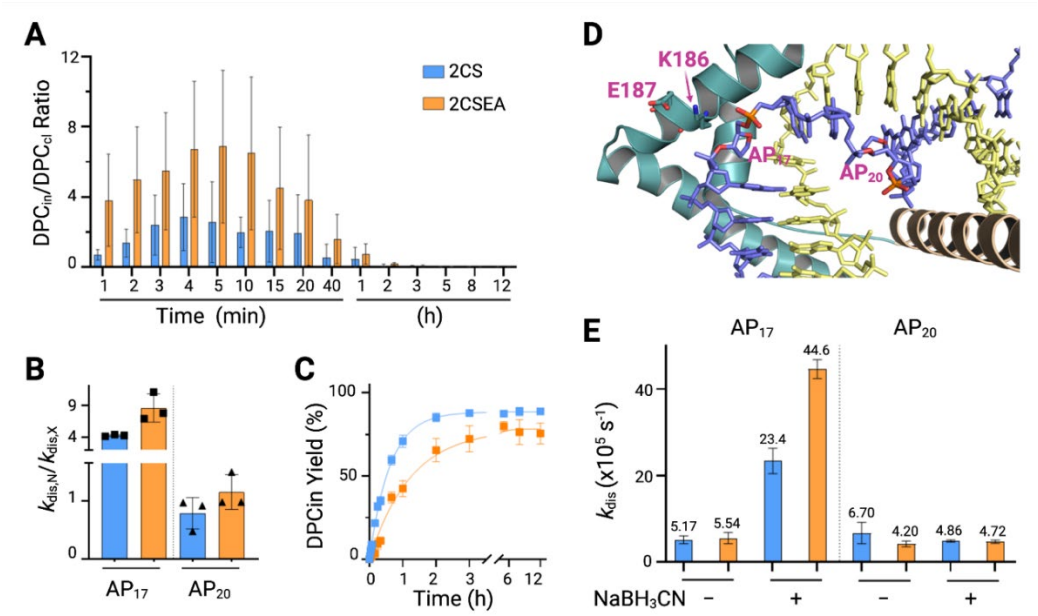

Figure 2.8. Involvement of E187 in β-elimination demonstrated using reactions of TFAM variants (blue for 2CS and orange for 2CSEA) with different AP-DNA substrates (AP_{17} and AP_{20}). (**A**) Instantaneous ratios of the yield of DPCs (DPC_{in}/DPC_{cl}) in a 12-h reaction without $NaBH_3CN$. The accumulation of DPC_{in} was apparent within 1 h for 2CSEA. (**B**) Ratios of the rate of AP-DNA disappearance in the presence of $NaBH_3CN$ ($k_{dis,N}$) and without $NaBH_3CN$ ($k_{dis,X}$). (**C**) Formation rates of DPC_{in} in the presence of $NaBH_3CN$. (**D**) Zoom-in view of the locations of E187, K186, and two AP sites in the crystal structure of TFAM (PDB:3TQ6). For comparison, two AP positions were shown in the same crystal structure. € Comparison of k_{dis} under different reaction conditions with AP_{17} or AP_{20}. Data were averages with S.D. (n=3).

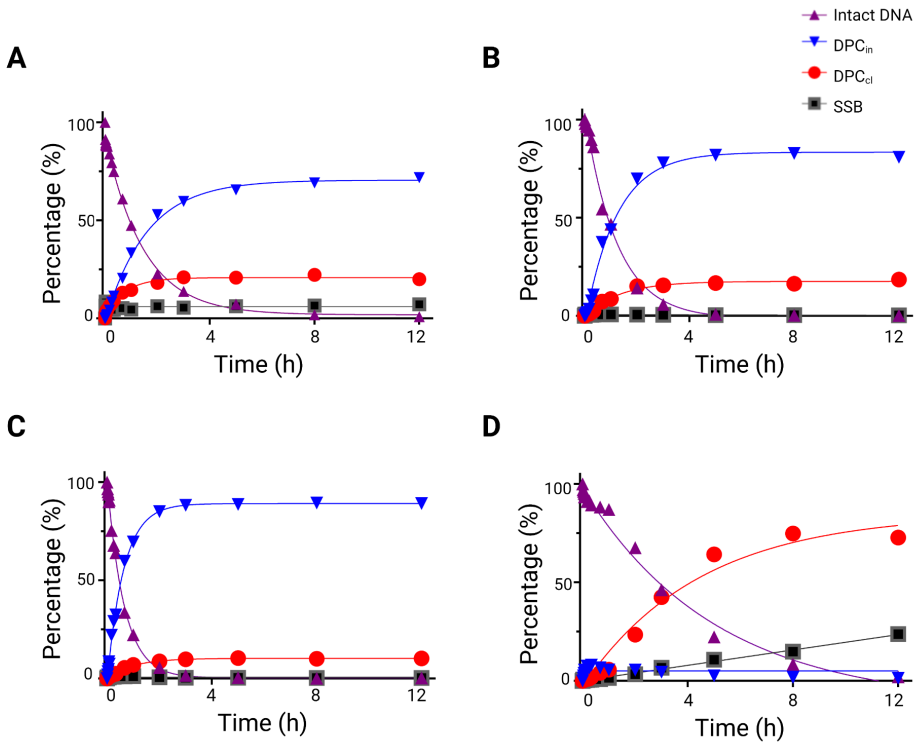

Figure 2.9. Quantification of products formed in TFAM-facilitated AP-DNA cleavage from Fig. S2. (A) wt TFAM with $NaBH_3CN$. (B) 2CS with $NaBH_3CN$. (C) 2CSEA with $NaBH_3CN$. (D) 2CSEA without $NaBH_3CN$.

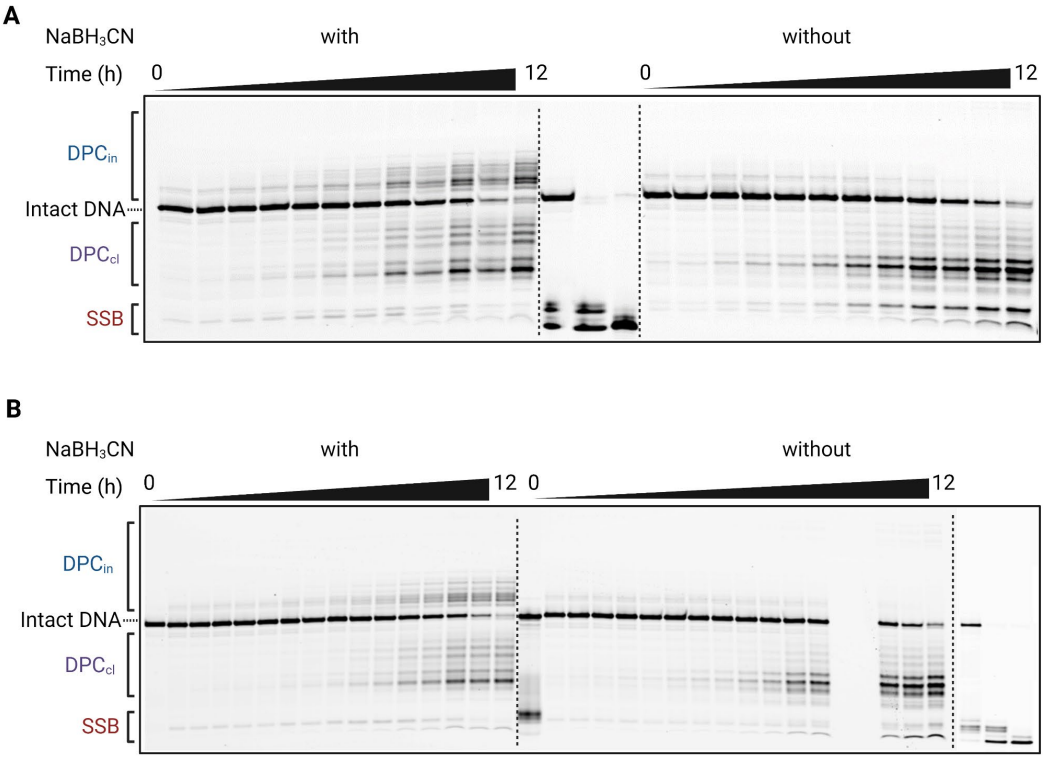

Figure 2.10. Representative gel images of reaction with AP_{20} and TFAM. Reactions contained 4 μM AP_{20}, 8 μM TFAM, 20 mM HEPES (pH 7.4), 90 mM NaCl, and 20 mM EDTA at 37 °C. An aliquot was quenched with an equal volume of 0.2 M NaBH4 at varying times. The quenched samples were digested by pronase E (0.5 mg/mL) at 41 °C for 12 h and then mixed with 95 % (v/v) formamide/50 mM EDTA solution for gel electrophoresis. (a) AP_{20} with 2CS. (b) AP_{20} with 2CSEA

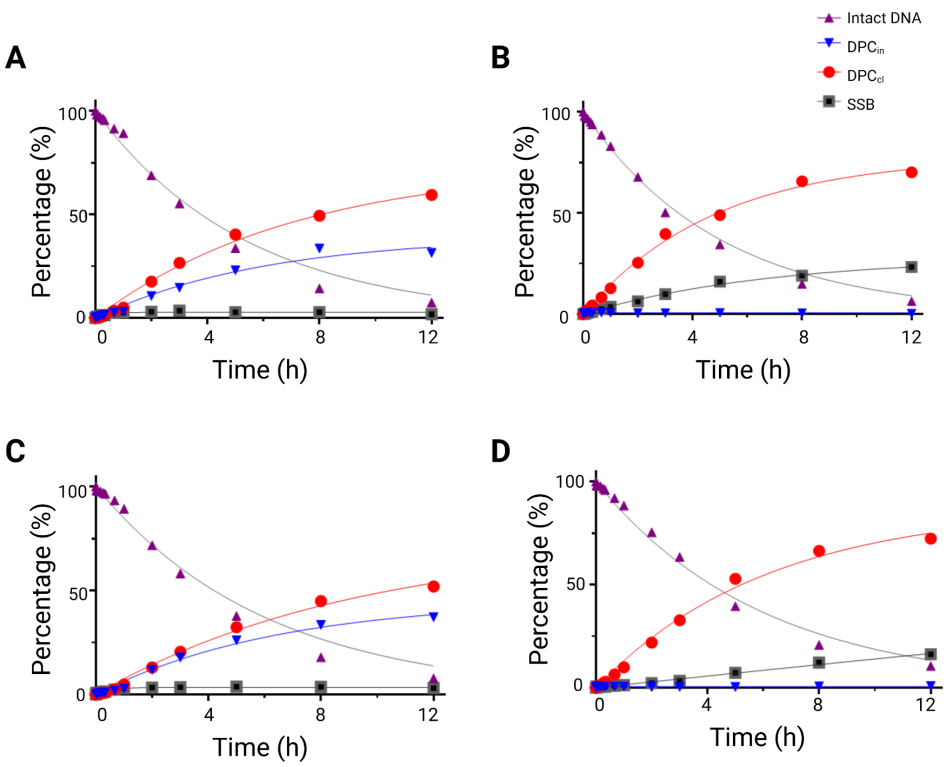

Figure 2.11. Quantification of products formed in TFAM-facilitated AP-DNA cleavage from Fig. S7. (A) AP_{20} and 2CS in the presence of $NaBH_3CN$. (B) AP_{20} and 2CS in the absence of $NaBH_3CN$. (C) AP_{20} and 2CSEA in the presence of $NaBH_3CN$. (D) AP_{20} and 2CSEA in the absence of $NaBH_3CN$.

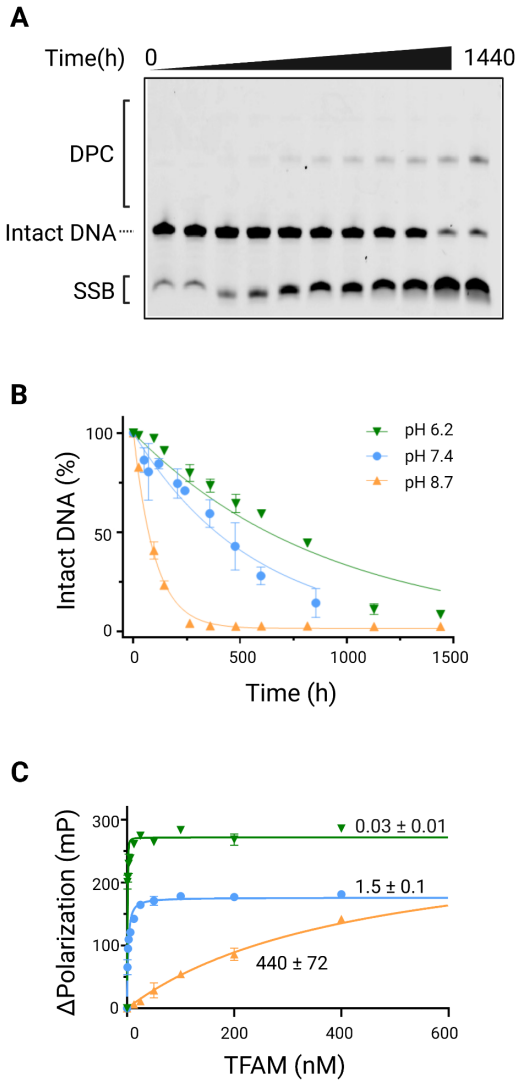

Figure 2.12. Spontaneous cleavage of AP_{17} under different pH conditions. (A) Representative gel image of AP_{17} under pH 6.2. 4 μM AP_{17} was incubated in a 50 mM MES buffer (pH 6.2) containing 90 mM NaCl and 20 mM EDTA at 37 °C. An aliquot was quenched with an equal volume of 0.2 M $NaBH_4$ at varying times. (B) Fitting the percent yield of AP_{17} to an exponential decay function resulted in a half-life of 630 h (± 27) at pH 6.2, 394 h (± 78) at pH 7.4, and 69 h (± 5) at pH 8.7. Data from pH 7.4 were from three independent experiments; errors were S.D. Data from pH 6.2 and pH 8.7 were from two independent experiments; errors were the ranges of data. (C) The equilibrium dissociation constant ($K_{d,DNA}$) of TFAM from fluorescence polarization assays. Data were fit to a quadratic equation to yield a $K_{d,DNA}$ of 0.03 nM (± 0.01) at pH 6.2, 1.5 nM (± 0.1) at pH 7.4, and 440 nM (± 72) at pH 8.7. Data were from two independent experiments; errors were the ranges of data.

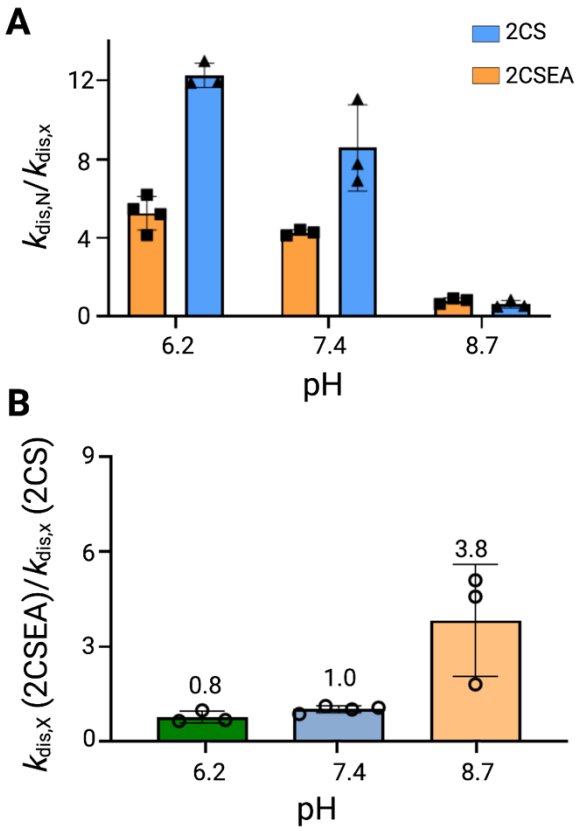

Figure 2.13. Comparison of the kinetics of AP-DNA scission by TFAM under different pH conditions. (**A**) Ratios of the rate of AP-DNA disappearance with ($k_{dis,N}$) and without NaBH3CN ($k_{dis,X}$) for 2CS and 2CSEA. (**B**) The ratios of $k_{dis,X}$ of 2CSEA divided by $k_{dis,X}$ of 2CS under different pH conditions. Data are average values. Errors are S.D. (n=3).

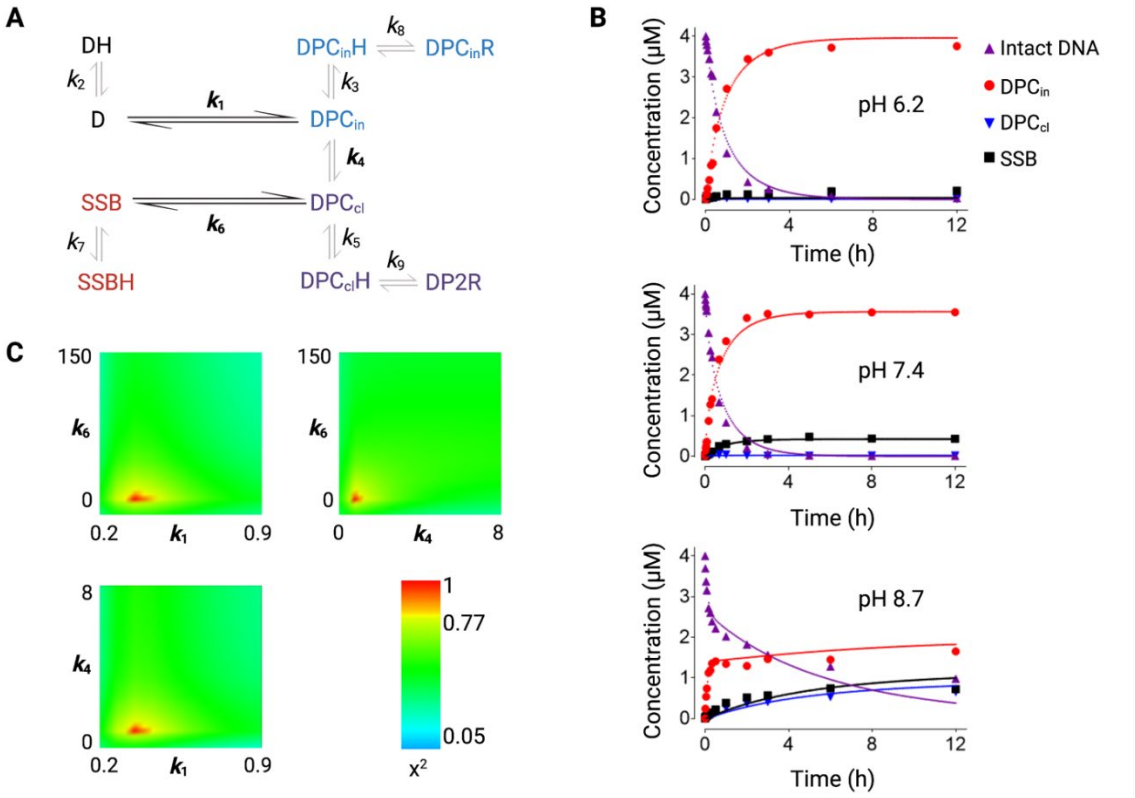

Figure 2.14. Global data analysis and kinetic simulations of TFAM-catalyzed AP-DNA strand scission under three pH conditions. (**A**) Simplified kinetic model for reactions in the presence of $NaBH_3CN$. The model for reactions in the absence of $NaBH_3CN$ contains similar steps except without steps forming DP1R (step 8) and DP2R (step 9). (**B**) Global fitting of data obtained under pH 6.2, 7.4, and 8.7. (**C**) FitSpace contour analysis demonstrates that the Schiff-base formation (k_1), β-elimination (k_4), and dissociation (k_6) were well constrained by data. Couture plots show k_1, k_4 and k_6 as a function of each other. The Chi^2 boundary of each parameter was set at 0.833.

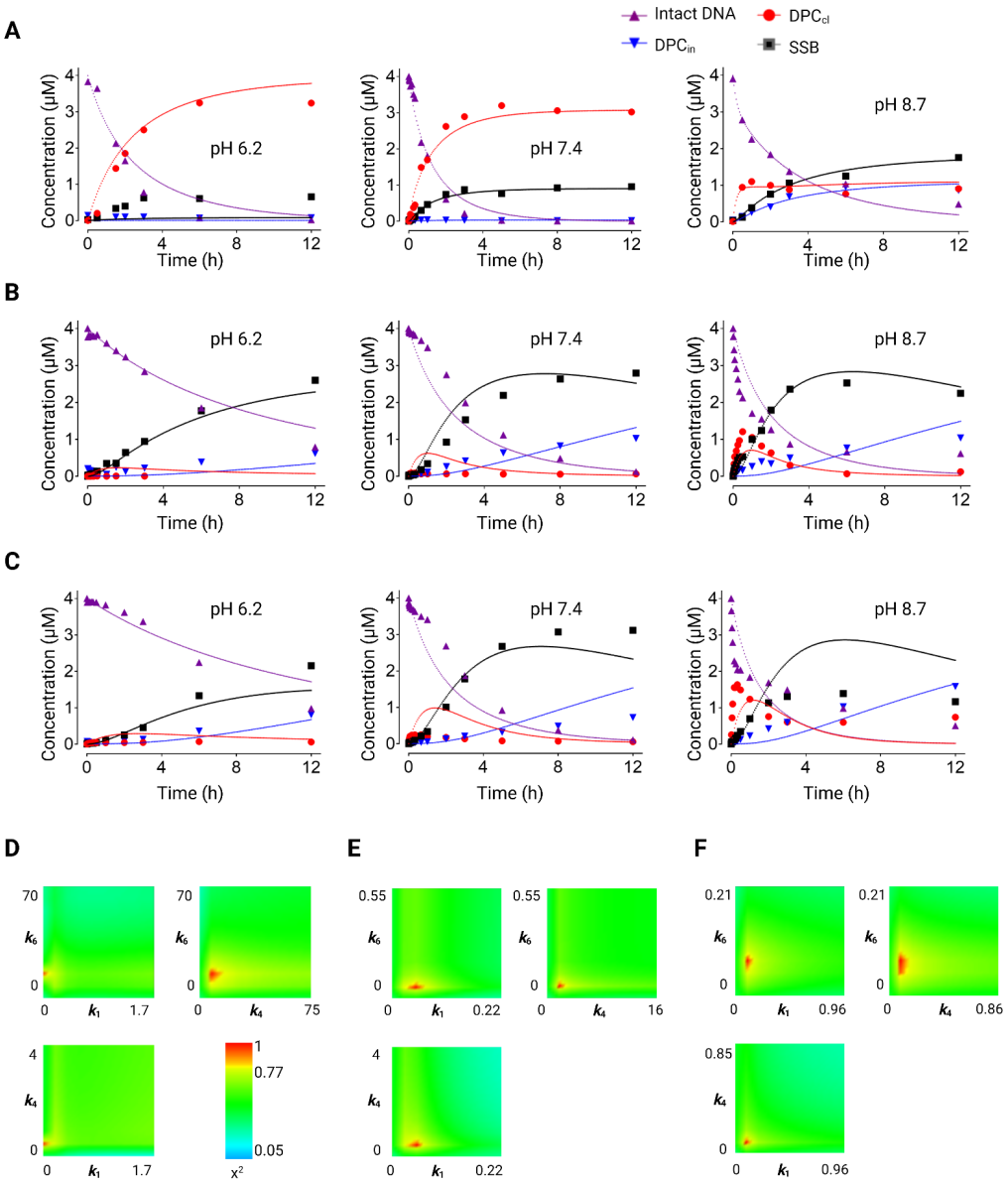

Figure 2.15. Global data fitting and simulations of TFAM catalyzed AP-DNA strand scission. (A) through (C), global fitting data from three pH conditions using KinTek Explorer. (D) through (F), FitSpace contour calculations. (A) and (D), TFAM 2CS in the presence of $NaBH_3CN$. (B) and (E), TFAM 2CS in the absence of $NaBH_3CN$. (C) and (F), TFAM 2CSEA in the absence of $NaBH_3CN$. The kinetic model in the absence of $NaBH_3CN$ is the same as that in Figure 5A, except without steps 8 and 9. Key steps, including the Schiff-base formation (k_1), β-elimination (k_4) and dissociation (k_6), were well constrained by data. Couture plots show k_1, k_4 and k_6 as a function of each other. The Chi^2 boundary for each parameter is set at 0.95.

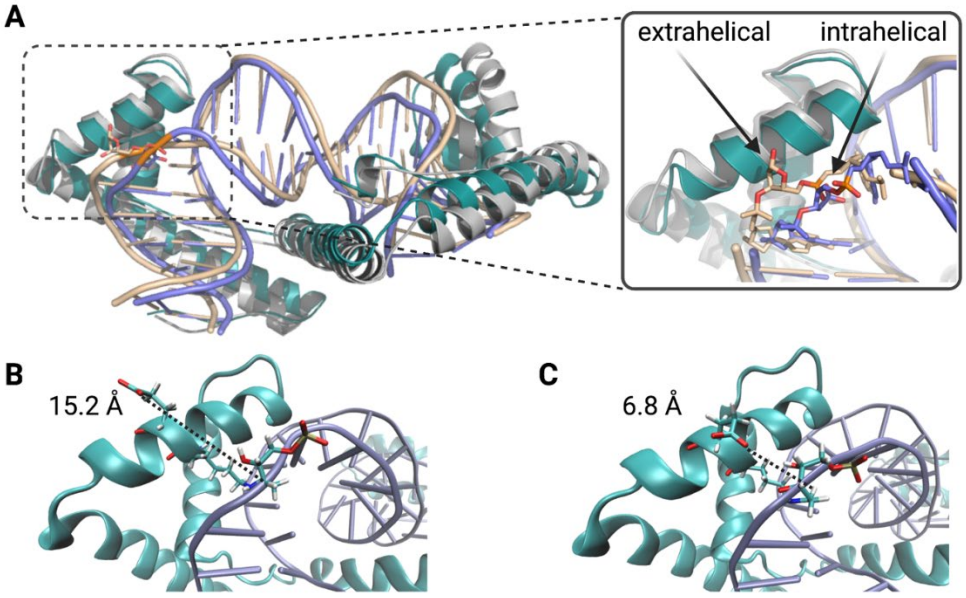

Figure 2.16. Conformational dynamics of AP sites and E187 obtained by MD simulations. (**A**) Representative intrahelical (purple) and extrahelical (wheat) conformations of the AP lesion site observed in MD simulations. In (**B**) and (**C**), the Schiff base was modeled in the TFAM-DNA complex. Two simulation frames show (**B**) the farthest distance (186 ns) and (**C**) the closest distance (163 ns) between the proximal O atom of E187 side chain and the C1′ hydrogen in angstrom.

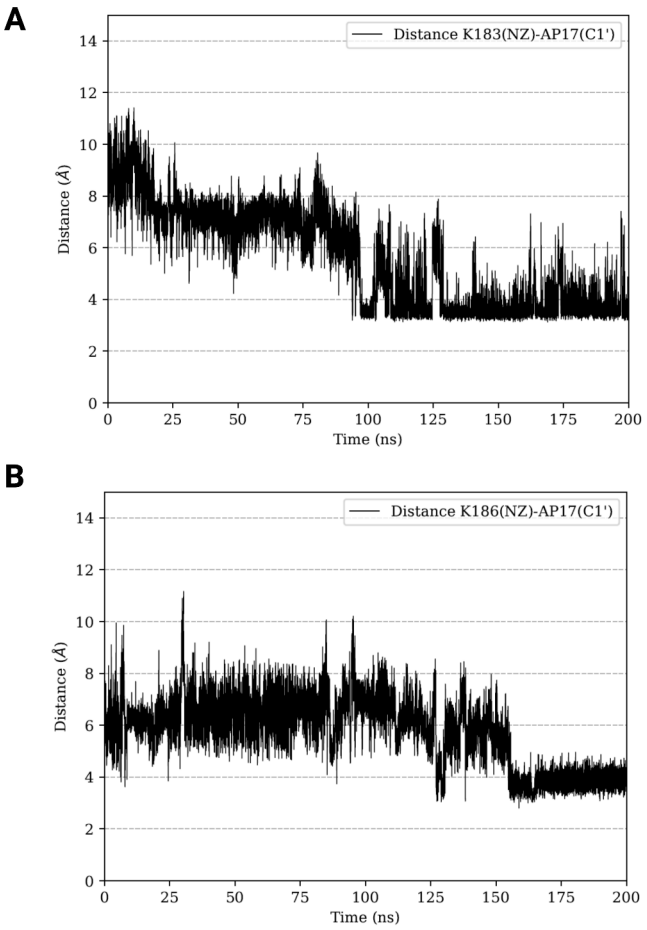

Figure 2.17. Distance between the N atom of ε-amino group and the C1' atom of the AP residue from MD Simulations. (A) Distance of the ε-N of K183 and the C1' atom of AP_{17}. At 90ns, the AP lesion rotated to the extrahelical conformation, which shortened the distance from > 6 Å to approximately 3.3 Å. (B) Distance of the ε-N of K186 and the C1' atom of AP_{17}. The rotation of AP lesion to the extrahelical conforamtion reduced the distance between the ε-N of K186 and the C1' atom. The smallest distance (~3.25 Å) was observed at 155 ns. The coordinates of the system at 155.00 ns were used to generate another system contaning the Schiff base intermediate in Fig. S12.

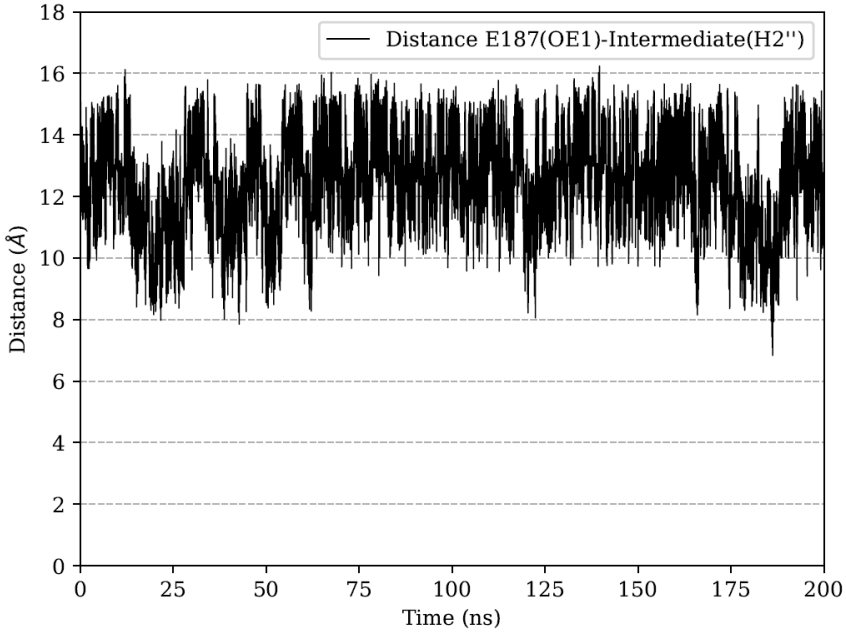

Figure 2.18. Distance between the carboxylate O atom of E187 and the H atom of C1'-H of the Schiff base intermediate. The plot shows the flexibility of E187 side chain through the wide range of distance from the attacking site of the intermediate whereby the closest distance is 6.83 Å.

Table 2.1. Comparison of the abundance (%) of Glu in TFAM with that of the human proteome and the entire proteome with all species. The mature sequence is without mitochondrial targeting sequence.

		Swiss-Prot database	Homo Sapiens	TFAM (full length)	TFAM (mature sequence)
Glutamate	Glu (E)	6.7	6.9	10.2	11.8
Aspartate	Asp (D)	5.5	4.7	3.3	3.9
His	His (H)	2.3	2.6	1.2	1.5
Lysine	Lys (K)	5.8	5.6	12.6	15.2
Arginine	Arg (R)	5.5	5.7	8.5	7.8

Table 2.2. Frequency of K, R, E, H and D in full-length TFAM across species. Data obtained and organized from Protein Data Bank.

Species, Trivial	Species Latin	GenPept	**K**	**R**	**E**	**H**	**D**
Human	Homo sapiens	NP_003192.1	12.6	8.5	10.2	1.2	3.3
Cat	Felis catus	XP_003993997	11.4	7.3	8.1	0.8	3.7
Wild boar	Sus scrofa	NP_001123683	12.2	6.9	8.9	0.4	4.1
Manatee	Trichechus manatus latirostris	XP_004369930.1	12.2	6.9	8.1	0	4.1
Pika	Ochotona curzoniae	XP_040831738	12.2	7.3	8.9	0.8	4.5
Armadillo-like	Dasypus novemcinctus	XP_004473261	13.8	7.3	5.7	0	4.9
Hedgehog	Echinops telfairi	XP_004701428	11.7	8.1	7.7	0	4.8
Elephant	Loxodonta africana	XP_003409078	12.1	7.3	6.9	0	4.4
Elephant shrew	Elephantulus edwardii	XP_006895656	11.9	7.4	7.4	0.4	3.7
Bat	Myotis lucifugus	XP_006098959	13.1	6.9	10.2	0.4	2.4
Armadillo	Dasypus novemcinctus	XP_004473258	12.7	6.1	6.9	1.2	4.5
Mouse	Mus musculus	NP_033386.1	12.8	7.8	9.5	0.8	3.7
Tasmanian devil	Sarcophilus harrisii	XP_003755126	14.3	5.9	11.4	2.2	3.3
Opossum	Monodelphis domestica	XP_007478397	13.1	9.7	8.9	0	4.6
Platypus	Ornithorhynchus anatinus	XP_001507982	13.7	8.1	8.5	0.4	3.8

Table 2.3 The rate of AP-DNA disappearance (k_{dis}) and DPC yields in TFAM-mediated AP-DNA strand scission. Reactions were carried out with AP_{17} (4 μM) and TFAM (8 μM) for 12 h with or without $NaBH_3CN$. Details are described in Experimental Procedures. Data are average values ± S.D. (n≥3).

TFAM variants	$NaBH_3CN$	AP-DNA disappearance k_{dis} (10^{-5} s^{-1})	Total DPC yield (%)	DPC_{in} yield (%)	DPC_{cl} yield (%)
WT	-	5.1 ± 0.6	83 ± 3.6	0.04 ± 0.03	85 ± 3.4
	+	18 ± 2.2	92 ± 3.9	76 ± 4.0	16 ± 3.2
2CS	-	5.2 ± 0.9	71 ± 2.7	1.6 ± 0.5	70 ± 3.2
	+	23 ± 2.3	99 ± 0.1	76 ± 6.3	24 ± 6.2
2CSEA	-	5.5 ± 1.3	80 ± 5.5	1.4 ± 0.4	79 ± 5.8
	+	44 ± 2.2	100 ± 0.1	89 ± 2.0	11 ± 2.0

Table 2.4. Observed peptides from reactions of 2CS with AP_{17} in the presence of $NaBH_3CN$. W^{OX} and M^{OX} indicate oxidized residues. Residues in blue are residues covalently linked to the AP site via the side chain. Relative intensities were based on the integrated peak areas.

Precursor ion m/z, charge state	Peak area	Starting residue	Crosslinked peptide	Charge	m/z	mass adduct	Δm (ppm)	Relative abundanc (%)
460.8956, z=3	22843659	52	KPVSSYLR	3	460.8952	431.1206	2.82	0.076
556.6128, z=3	169883571	60	FSKEQLPIFK	3	556.6128	431.1206	2.07	0.65
834.4155, z=2	26015092	60	FSKEQLPIFK	2	834.4155	431.1206	2.32	
572.9793 z=3	59109121	63	EQLPIFKAQNPDAK	3	572.9793	118.0630	3.25	0.93
858.9655, z=2	5419308	63	EQLPIFKAQNPDAK	2	858.9655	118.0630	3.78	
677.3333, z=3	200458517	63	EQLPIFKAQNPDAK	3	677.3333	431.1206	4.9	
1015.4956, z=2	14061673	63	EQLPIFKAQNPDAK	2	1015.4956	431.1206	4.48	
629.9720, z=3	470055809	70	AQNPDAKTTELIR	3	629.972	431.1206	2.29	1.69

944.4538, z=2	36721495	70	AQNPDAKTTELIR	2	944.4538	431.1206	1.98	
552.6168, z=3	12948309	105	AEWQVYKEEISK	3	552.6168	118.0630	4.36	0.23
656.9706, z=3	49075274	105	AEWQVYKEEISK	3	656.9706	431.1206	5.59	
984.9514, z=2	5650878	105	AEWQVYKEEISK	2	984.9514	431.1206	5	
377.8733, z=3	11617449	132	EIMDKHLK	3	377.8755	118.0630	2.67	1.52
566.3095, z=2	3295830	132	EIMDKHLK	2	566.3095	118.0630	2.95	
606.2928, z=2	22080641	132	EIMDKHLK	2	606.2928	198.0293	3	
482.2282, z=3	341403813	132	EIMDKHLK	3	482.2282	431.1206	2.43	
722.8387, z=2	48301978	132	EIMDKHLK	2	722.8387	431.1206	2.86	
487.5596, z=3	25824709	132	EIM^{OX}DKHLK	3	487.5596	431.1206	1.93	
730.8366, z=2	3179444	132	EIM^{OX}DKHLK	2	730.8366	431.1206	3.45	
751.389	220983	137	HLKR	1	751.389	198.029	3.74	2.26

0, z=1	87					3		
492.7444, z=2	11917679	137	HLKR	2	492.7444	431.1206	3.53	
760.3899, z=2	643082238	138	HLKRKAMTK	2	760.3899	407.1094	-6.26	
776.3643, z=1	84504962	142	AMTKK	1	776.3643	198.0293	2.52	
505.2319, z=2	118761334	142	AMTKK	2	505.2319	431.1206	2.32	0.72
513.2296, z=2	11301668	142	AM^{OX}TKK	2	513.2296	431.1206	2.77	
390.2172, z=4	8935908	147	KELTLLGKPK	4	390.2172	431.1206	3.41	
519.9537, z=3	12379920	147	KELTLLGKPK	3	519.9537	431.1206	3.48	
558.8492, z=2	9678166	148	ELTLLGKPK	2	558.8492	118.0630	2.79	3.30
477.2549, z=3	661910362	148	ELTLLGKPK	3	477.2549	431.1206	2.79	
715.3785, z=2	295524415	148	ELTLLGKPK	2	715.3785	431.1206	2.88	
510.2696, z=2	60695791	182	LKTVK	2	510.2696	431.1206	2.8	0.20
511.7812, z=2	22996205	184	TVKENWK	2	511.7812	118.0630	2.81	86.9

551.7643, z=2	100363523	184	TVKENWK	2	551.7643	198.0293	2.52	
1102.5207, z=1	14698247	184	TVKENWK	1	1102.5207	198.0293	2.46	
1134.5106, z=1	2446233	184	TVKENW^{OX}(+32)K	1	1134.5106	198.0293	-6.51	
567.7585, z=2	1701666	184	TVKENW^{OX}(+32)K	2	567.7585	198.0293	-7.77	
445.8758, z=3	1.5997E+10	184	TVKENWK	3	445.8758	431.1206	1.84	
668.3104, z=2	6280963552	184	TVKENWK	2	668.3104	431.1206	2.75	
1335.6117, z=1	59561376	184	TVKENWK	1	1335.6117	431.1206	1.8	
447.2077, z=3	141158225	184	TVKENW^{OX}(+4)K	3	447.2077	431.1206	-1.36	
670.3083, z=2	48517566	184	TVKENW^{OX}(+4)K	2	670.3083	431.1206	-0.39	
451.2078, z=3	1677595506	184	TVKENW^{OX}(+16)K	3	451.2078	431.1206	2.64	
676.3080, z=2	97315267	184	TVKENW^{OX}(+16)K	2	676.308	431.1206	2.94	
452.539	163012	184	TVKE	3	452.539	431.120	-3.87	

9, z=3	22		NW^{OX}(+20)K		9	6		
678.3068, z=2	5092523	184	TVKENW^{OX}(+20)K	2	678.3068	431.1206	-2.59	
456.5392, z=3	1156922250	184	TVKENW^{OX}(+32)K	3	456.5392	431.1206	2.08	
684.3049, z=2	379126302	184	TVKENW^{OX}(+32)K	2	684.3049	431.1206	2.1	
594.2587, z=3	106439639	187	ENWKNLSDSEK	3	594.2587	431.1206	3.74	0.45
890.8837, z=2	23470822	187	ENWKNLSDSEK	2	890.8837	431.1206	2.24	
604.9214, z=3	3872195	187	ENW^{OX}(+32)KNLSDSEK	3	604.9214	431.1206	-2.89	
906.8779, z=2	370368	187	ENW^{OX}(+32)KNLSDSEK	2	906.8779	431.1206	-3.21	
381.7411, z=2	13686499	228	KDLLR	2	381.7411	118.0630	3.12	0.22
842.4410, z=1	14879955	228	KDLLR	1	842.441	198.0293	3.22	
538.2703, z=2	38340996	228	KDLLR	2	538.2703	431.1206	2.95	

687.3707, z=1	90027500	234	TIKK	1	687.3707	198.0293	2.75	0.81
460.7349, z=2	151289838	234	TIKK	2	460.7349	431.1206	2.02	
920.4623, z=1	1502451	234	TIKK	1	920.4623	431.1206	2.38	

Table 2.5. Observed peptides from reactions of TFAM 2CS with AP_{17} in the absence of $NaBH_3CN$. W^{OX} and M^{OX} indicate oxidized residues. Residues in blue are residues covalently linked to the AP site via the side chain. Relative intensities were based on the integrated peak areas.

Ion m/z, charge state	Peak area	Starting residue	Crosslinked peptide	Charge	m/z	mass adduct	Δm (ppm)	Relative abundance (%)
534.3104, z=2	16506502	52	KPVSSYLR	2	534.3104	118.0630	3.22	4.20
587.8100, z=2	1201580	97	KIYQDAYR	2	587.8100	118.0630	1.62	0.31
415.6004, z=3	983507	147	KELTLLGKPK	3	415.6004	118.0630	2.5	0.25
583.9617, z=3	1535470	198	ELYIQHAKEDETR	3	583.9617	118.0630	2.33	0.39
558.8419, z=2	10536603	148	ELTLLGKPK	2	558.8419	118.0630	-10.27	3.77
715.3782, z=2	902441	148	ELTLLGKPK	2	715.3782	431.1206	2.46	
477.2548, z=3	3376491	148	ELTLLGKPK	3	477.2548	431.1206	2.58	
559.7612, z=2	2286843	184	TVKENW+16K	2	559.7612	198.0293	1.5	0.58
489.9044, z=3	14725495	187	ENWKNLSDSEK	3	489.9044	118.0630	0.92	4.80

734.3530, z=2	3241922	187	ENWKNLSDSEK	2	734.3530	118.0630	1.35	
500.5675, z=3	870619	187	ENW+32KNLSDSEK	3	500.5675	118.0630	0.58	
525.6177, z=3	99879762	70	AQNPDAKTTELIR	3	525.6177	118.0630	-0.63	26.4
787.9233, z=2	3643829	70	AQNPDAKTTELIR	2	787.9233	118.0630	0.22	
631.6605, z=3	4127741	191	NLSDSEKELYIQHAK	3	631.6605	118.0630	3.09	1.22
473.9965, z=4	683206	191	NLSDSEKELYIQHAK	4	473.9965	118.0630	1.33	
452.2582, z=3	13010469	60	FSKEQLPIFK	3	452.2582	118.0630	-2.01	3.37
677.8845, z=2	223283	60	FSKEQLPIFK	2	677.8845	118.0630	-0.38	
552.6135, z=3	120938724	105	AEWQVYKEEISR	3	552.6135	118.0630	-0.61	36.3
828.4169, z=2	11617960	105	AEWQVYKEEISR	2	828.4169	118.0630	-0.94	
557.9440, z=3	3335355	105	AEW+16QVYKEEIS	3	557.9440	118.0630	-3.64	

			R					
563.2784, z=3	6149504	105	AEW+32QVYKEEISR	3	563.2784	118.0630	1.31	
844.4121, z=2	351529	105	AEW+32QVYKEEISR	2	844.4121	118.0630	-0.57	
573.3110, z=3	54247334	63	EQLPIFKAQNPDAK	3	573.3110	118.0630	-4.15	14.6
858.9632, z=2	2987980	63	EQLPIFKAQNPDAK	2	858.9632	118.0630	1.11	
633.0057, z=3	12824049	117	FKEQLTPSQIMSLEK	3	633.0057	118.0630	1.45	3.36
949.0026, z=2	385467	117	FKEQLTPSQIMSLEK	2	949.0026	118.0630	-0.7	
557.3046, z=2	2006350	132	EIMDKHLK	2	557.3046	100.0524	3.71	0.51

Table 2.6. TFAM-catalyzed AP-DNA cleavage reaction with AP_{17} in 12-h reactions under different pH conditions. Data are average values ± S.D. (n≥3). $k_{dis,N}$ is the rate of AP-DNA disappearance in the presence of $NaBH_3CN$; $k_{dis,X}$ is the rate of AP-DNA disappearance in the absence of $NaBH_3CN$.

pH	TFAM	$NaBH_3CN$	$t_{1/2}$ (h)	AP-DNA disappearance k_{dis} (10^{-5} s^{-1})	$k_{dis,N}/k_{dis,X}$
6.2	2CS	+	1.1 ± 0.2	19 ± 1.5	5.6 ± 0.5
		-	5.7 ± 0.9	3.4 ± 0.5	
	2CSEA	+	0.6 ± 0	32 ± 1.6	12 ± 0.6
		-	7.5 ± 0.6	2.6 ± 0.2	
7.4	2CS	+	0.8 ± 0.1	23 ± 2.9	4.3 ± 0.1
		-	3.8 ± 0.6	5.2 ± 0.9	
	2CSEA	+	0.4 ± 0	44 ± 2.2	8.6 ± 2.2
		-	3.6 ± 0.8	5.5 ± 1.3	
8.7	2CS	+	0.6 ± 0.1	35 ± 4.5	0.8 ± 0.1
		-	0.4 ± 0.1	44 ± 6.2	
	2CSEA	+	0.2 ± 0	96 ± 15.3	0.6 ± 0.2
		-	0.1 ± 0.1	162 ± 61	

Table 2.7. Kinetic parameters of TFAM-facilitated AP-DNA cleavage reaction with AP_{17} in a 12-h reaction under pH 7.4. Summary of kinetic parameters including the half-life ($t_{1/2}$) of AP-DNA, the AP-DNA disappearance (k_{dis}) rate, and the DPC_{in} formation rate ($k_{f,in}$) intact. All data were average values ± S.D. (n≥3). $k_{f,in}$ in the absence of $NaBH_3CN$ was ambiguous due to the low abundance of DPC_{in} and was not calculated.

TFAM variants	DNA substrate	$NaBH_3CN$	$t_{1/2}$ (h)	$k_{f,in}$ (10^{-5} s^{-1})	k_{dis} (10^{-5} s^{-1})
WT	AP_{17}	-	3.8 ± 0.4		5.1 ± 0.6
	AP_{17}	+	1.1 ± 0.2	16 ± 2.1	17.9 ± 2.2
C49S	AP_{17}	-	4.2 ± 0.1		4.6 ± 0.1
	AP_{17}	+	0.9 ± 0.01	19 ± 0.3	21.0 ± 0.4
2CS	AP_{17}	-	3.8 ± 0.6		5.2 ± 0.9
	AP_{17}	+	0.8 ± 0.1	25 ± 2.5	23.4 ± 2.9
2CSEA	AP_{17}	-	3.6 ± 0.8		5.5 ± 1.3
	AP_{17}	+	0.4 ± 0.02	46 ± 2.4	44.6 ± 2.2
2CS	AP_{20}	-	3.1 ± 0.9		6.7 ± 2.4
	AP_{20}	+	4.0 ± 0.2	4.4 ± 0.5	4.9 ± 0.3
2CSEA	AP_{20}	-	4.7 ± 0.8		4.2 ± 0.7
	AP_{20}	+	4.1 ± 0.3	2.8 ± 1.4	4.7 ± 0.4

Table 2.8. Effects of TFAM variants on the half-life ($t_{1/2}$) of AP-DNA. The $t_{1/2}$ of AP-DNA was obtained under the same assay conditions as TFAM reactions except without TFAM. The fold reduction was calculated based on the ratios of $t_{1/2}$ of free AP_{17} divided by $t_{1/2}$ of AP_{17} in DNA-TFAM reactions in the absence of $NaBH_3CN$. Data under pH 7.4 are average values ± S.D. (n=3). Data obtained under pH 6.2 and pH 8.7 are average values ± range of data (n=2).

	$t_{1/2}$ (h) of free AP-DNA	Fold reduction in $t_{1/2}$ relative to 2CS	Fold reduction in $t_{1/2}$ relative to 2CSEA
pH 6.2	630 ± 37	110	84
pH 7.4	393 ± 78	103	109
pH 8.7	69 ± 7	173	690

Table 2.9. TFAM-facilitated AP-DNA cleavage with AP_{17} in a 12-h reaction under pH 6.2, 7.4 and 8.7. Summary of DPC formation comparison from kinetic parameters including DPC_{in} yield, DPC_{cl} yield, and the ratio between DPC_{in}/DPC_{cl} after 12 h. The percent yield is calculated based on the sum of remaining AP_{17}, DPC_{in}, DPC_{cl}, and SSBs. Data are average values ± S.D. ($n \geq 3$).

pH	TFAM	$NaBH_3CN$	DPC_{in} (%)	DPC_{cl} (%)	DPC_{in}/DPC_{cl}
6.2	2CS	+	80 ± 5.3	16 ± 4.2	5.3 ± 1.5
		-	0.6 ± 0.2	66 ± 1.1	0.01 ± 0.003
	2CSEA	+	94 ± 3.4	5.2 ± 3.1	29 ± 27
		-	1.4 ± 1.2	54 ± 5.3	0.03 ± 0.03
7.4	2CS	+	77 ± 4.0	24 ± 6.2	3.3 ± 1.1
		-	1.6 ± 0.5	70 ± 3.2	0.02 ± 0.01
	2CSEA	+	89 ± 1.9	11 ± 2.0	8.5 ± 1.7
		-	1.4 ± 0.4	79 ± 5.8	0.02 ± 0.01
8.7	2CS	+	27 ± 5.6	44 ± 4.0	0.6 ± 0.1
		-	2.1 ± 0.2	56 ± 3.8	0.1 ± 0.04
	2CSEA	+	41 ± 0.7	18 ± 8.8	2.9 ± 2.0
		-	12 ± 11	29 ± 7.9	0.8 ± 0.7

Table 2.10. Simulated parameters for Schiff-base formation, β-elimination and dissociation reactions with 2CS and 2CSEA and AP_{17}. Errors are S.E. from KinTek Explorer.

Steps	TFAM	$NaBH_3CN$	Lower bound	Upper bound	Best-fit values
k_1 (μM^{-1} h^{-1}) forward, Schiff-base formation	2CS	+	0.13	0.21	0.16 ± 0.04
		-	0.05	0.09	0.07 ± 0.01
	2CSEA	+	0.34	0.47	0.39 ± 0.06
		-	0.05	0.12	0.09 ± 0.03
k_{-1} (h^{-1}) reverse, Schiff base formation	2CS	+	1.3	5.6	2.5 ± 1.7
		-	2.1×10^{-9}	2.1×10^{-6}	2.1×10^{-7}
	2CSEA	+	0.34	0.47	4.3 ± 1.2
		-	4.0×10^{-9}	4.0×10^{-6}	4.0×10^{-7}
k_4 (h^{-1}) forward, β-elimination	2CS	+	1.3	5.0	2.5 ± 1.6
		-	1.3	2.5	1.6 ± 0.46
	2CSEA	+	0.50	1.2	0.78 ± 0.37
		-	0.68	1.3	0.85 ± 0.24
k_{-4} (h^{-1}) reverse, β-elimination	2CS	+	24	120	59
		-	8.1×10^{-9}	8.1×10^{-6}	8.1×10^{-7}
	2CSEA	+	24	110	58.2
		-	1.7×10^{-10}	1.7×10^{-7}	1.7×10^{-8}
k_6 (h^{-1}) forward, TFAM dissociation	2CS	+	11	17	14 ± 4
		-	0.04	0.08	0.05 ± 0.01
	2CSEA	+	10	20	16 ± 6
		-	0.05	0.07	0.06 ± 0.03
k_{-6} (h^{-1}) reverse, TFAM dissociation	2CS	+	6.9×10^{-9}	6.9×10^{-6}	6.9×10^{-7}
		-	8.9×10^{-12}	8.9×10^{-9}	8.9×10^{-10}
	2CSEA	+	1.2×10^{-10}	1.2×10^{-7}	1.2×10^{-8}
		-	6.9×10^{-10}	6.9×10^{-7}	6.9×10^{-8}

Table 2.11. Kinetic parameters from KinTek simulations continued from Table 5 for 2CS and 2CSEA under trapping and no trapping conditions with AP_{17}. Errors were the standard errors from the global fitting.

Steps	TFAM	$NaBH_3CN$	Lower bound	Upper bound	Best fit value
k_{-2} (h^{-1}) DH deprotonation	2CS	+	2.3×10^3	5.6×10^3	$(3.6 \pm 1.6) \times 10^3$
		-	1.1×10^3	2.7×10^3	$(1.8 \pm 5.9) \times 10^3$
	2CSEA	+	3.5×10^3	5.8×10^3	$(4.6 \pm 1.3) \times 10^3$
		-	4.1×10^2	2.7×10^3	$(8.0 \pm 4.0) \times 10^2$
k_{-3} (h^{-1}) $DPC_{in}H$ deprotonation	2CS	+	2.1×10^4	2.1×10^7	2.1×10^6
		-	1.9×10^{10}	1.9×10^{13}	1.2×10^{12}
	2CSEA	+	2.8×10^4	3.5×10^7	3.0×10^6
		-	4.3×10^9	4.3×10^{12}	4.4×10^{11}
k_{-5} (h^{-1}) $DPC_{cl}H$ deprotonation	2CS	+	2.3×10^{-12}	2.3×10^{-9}	
		-	320	3.8×10^4	
	2CSEA	+	2.1×10^{-9}	2.1×10^{-6}	
		-	5.0×10^8	5.0×10^{11}	
k_{-7} (h^{-1}) SSBH deprotonation	2CS	+	1.0×10^8	1.0×10^{11}	
		-	1.0×10^{10}	1.0×10^{13}	
	2CSEA	+	460	4.6×10^5	
		-	10×10^7	10×10^{10}	
k_{+8} (h^{-1}) forward, $DPC_{in}H$ reduction	2CS	+	86	1.7×10^5	8.5×10^3
		-	NA		
	2CSEA	+	84	1.1×10^5	9.6×10^3
		-	NA		

k_{-8} (h^{-1}) reverse, $DPC_{in}H$ reduction	2CS	+	1.7×10^{-6}	1.7×10^{-9}	
		-	NA		
	2CSEA	+	9.0×10^{-9}	9.0×10^{-6}	
		-	NA		
k_{+9} (h^{-1}) forward, $DPC_{cl}H$ reduction	2CS	+	85	8.5×10^{4}	8.5×10^{3}
		-	NA		
	2CSEA	+	96	9.6×10^{4}	9.6×10^{3}
		-	NA		
k_{-9} (h^{-1}) reverse, $DPC_{cl}H$ reduction	2CS	+	1.8×10^{-9}	1.8×10^{-6}	
		-	NA		
	2CSEA	+	9.5×10^{-9}	9.5×10^{-6}	
		-	NA		

References

(1) Friedman, J. R.; Nunnari, J. Mitochondrial Form and Function. *Nature*. 2014. DIO. 10.1038/nature12985.

(2) Alexeyev, M.; Shokolenko, I.; Wilson, G.; LeDoux, S. The Maintenance of Mitochondrial DNA Integrity--Critical Analysis and Update. *Cold Spring Harb Perspect Biol* **2013**, *5* (5). DIO. 10.1101/CSHPERSPECT.A012641.

(3) Wu, Z.; Sainz, A. G.; Shadel, G. S. Mitochondrial DNA: Cellular Genotoxic Stress Sentinel. *Trends Biochem Sci* **2021**, *46* (10), 812–821. DIO. 10.1016/j.tibs.2021.05.004.

(4) Zhao, L.; Sumberaz, P. Mitochondrial DNA Damage: Prevalence, Biological Consequence, and Emerging Pathways. *Chemical Research in Toxicology*. American Chemical Society October 19, 2020, pp 2491–2502. DIO. 10.1021/acs.chemrestox.0c00083.

(5) Young, M. J.; Copeland, W. C. Human Mitochondrial DNA Replication Machinery and Disease. **2016**. DIO. 10.1016/j.gde.2016.03.005.

(6) Gustafson, M. A.; Sullivan, E. D.; Copeland, W. C. Consequences of Compromised Mitochondrial Genome Integrity. *DNA Repair (Amst)* **2020**, *93*. DIO. 10.1016/J.DNAREP.2020.102916.

(7) Shokolenko, I. N.; Alexeyev, M. F. Mitochondrial DNA: A Disposable Genome? *Biochimica et Biophysica Acta - Molecular Basis of Disease*. 2015. DIO. 10.1016/j.bbadis.2015.05.016.

(8) Zhao, L. Mitochondrial DNA Degradation: A Quality Control Measure for Mitochondrial Genome Maintenance and Stress Response. *Enzymes* **2019**, *45*, 311–341. DIO. 10.1016/BS.ENZ.2019.08.004.

(9) Scheibye-Knudsen, M.; Fang, E. F.; Croteau, D. L.; Wilson, D. M.; Bohr, V. A. Protecting the Mitochondrial Powerhouse. *Trends in Cell Biology*. 2015. DIO. 10.1016/j.tcb.2014.11.002.

(10) Kauppila, T. E. S.; Kauppila, J. H. K.; Larsson, N. G. Mammalian Mitochondria and Aging: An Update. *Cell Metabolism*. 2017. DIO. 10.1016/j.cmet.2016.09.017.

(11) Valente, W. J.; Ericson, N. G.; Long, A. S.; White, P. A.; Marchetti, F.; Bielas, J. H. Mitochondrial DNA Exhibits Resistance to Induced Point and Deletion Mutations. *Nucleic Acids Res* **2016**, *44* (18). DIO. 10.1093/nar/gkw716.

(12) Leuthner, T. C.; Benzing, L.; Kohrn, B. F.; Bergemann, C. M.; Hipp, M. J.; Hershberger, K. A.; Mello, D. F.; Sokolskyi, T.; Stevenson, K.; Merutka, I. R.; Seay, S. A.; Gregory, S. G.; Kennedy, S. R.; Meyer, J. N. Resistance of Mitochondrial DNA to Cadmium and Aflatoxin B1damage-Induced Germline Mutation Accumulation in C. Elegans. *Nucleic Acids Res* **2022**, *50* (15). DIO. 10.1093/nar/gkac666.

(13) Gross, N. J.; Getz, G. S.; Rabinowitz, M. Apparent Turnover of Mitochondrial Deoxyribonucleic Acid and Mitochondrial Phospholipids in the Tissues of the Rat. *Journal of Biological Chemistry* **1969**, *244* (6). DIO. 10.1016/s0021-9258(18)91795-3.

(14) West, A. P.; Khoury-Hanold, W.; Staron, M.; Tal, M. C.; Pineda, C. M.; Lang, S. M.; Bestwick, M.; Duguay, B. A.; Raimundo, N.; MacDuff, D. A.; Kaech, S. M.; Smiley, J. R.; Means, R. E.; Iwasaki, A.; Shadel, G. S. Mitochondrial DNA Stress Primes the Antiviral Innate Immune Response. *Nature* **2015**, *520* (7548). DIO. 10.1038/nature14156.

(15) Xian, H.; Watari, K.; Sanchez-Lopez, E.; Offenberger, J.; Onyuru, J.; Sampath, H.; Ying, W.; Hoffman, H. M.; Shadel, G. S.; Karin, M. Oxidized DNA Fragments Exit Mitochondria via MPTP- and VDAC-Dependent Channels to Activate NLRP3 Inflammasome and Interferon Signaling. *Immunity* **2022**, *55* (8). DIO. 10.1016/j.immuni.2022.06.007.

(16) Peeva, V.; Blei, D.; Trombly, G.; Corsi, S.; Szukszto, M. J.; Rebelo-Guiomar, P.; Gammage, P. A.; Kudin, A. P.; Becker, C.; Altmüller, J.; Minczuk, M.; Zsurka, G.; Kunz, W. S. Linear Mitochondrial DNA Is Rapidly Degraded by Components of the Replication Machinery. *Nat Commun* **2018**, *9* (1). DIO. 10.1038/s41467-018-04131-w.

(17) Nissanka, N.; Bacman, S. R.; Plastini, M. J.; Moraes, C. T. The Mitochondrial DNA Polymerase Gamma Degrades Linear DNA Fragments Precluding the Formation of Deletions. *Nat Commun* **2018**, *9* (1). DIO. 10.1038/s41467-018-04895-1.

(18) Matic, S.; Jiang, M.; Nicholls, T. J.; Uhler, J. P.; Dirksen-Schwanenland, C.; Polosa, P. L.; Simard, M. L.; Li, X.; Atanassov, I.; Rackham, O.; Filipovska, A.; Stewart, J. B.; Falkenberg, M.; Larsson, N. G.; Milenkovic, D. Mice Lacking the Mitochondrial Exonuclease MGME1 Accumulate MtDNA Deletions without Developing Progeria. *Nat Commun* **2018**, *9* (1). DIO. 10.1038/s41467-018-03552-x.

(19) Milenkovic, D.; Sanz-Moreno, A.; Calzada-Wack, J.; Rathkolb, B.; Amarie, O. V.; Gerlini, R.; Aguilar-Pimentel, A.; Misic, J.; Simard, M. L.; Wolf, E.; Fuchs, H.; Gailus-Durner, V.; de Angelis, M. H.; Larsson, N. G. Mice Lacking the Mitochondrial Exonuclease MGME1 Develop Inflammatory Kidney Disease with Glomerular Dysfunction. *PLoS Genet* **2022**, *18* (5). DIO. 10.1371/journal.pgen.1010190.

(20) Xu, W.; Boyd, R. M.; Tree, M. O.; Samkari, F.; Zhao, L. Mitochondrial Transcription Factor A Promotes DNA Strand Cleavage at Abasic Sites. *Proceedings of the National Academy of Sciences* **2019**, *116* (36), 17792–17799. DIO. 10.1073/pnas.1911252116.

(21) Xu, W.; Tang, J.; Zhao, L. DNA–Protein Cross-Links between Abasic DNA Damage and Mitochondrial Transcription Factor A (TFAM). *Nucleic Acids Res* **2023**, *51* (1), 41–53. DIO. 10.1093/nar/gkac1214.

(22) Xu, W.; Zhao, L. An Enzyme-Linked Immunosorbent Assay for the Detection of Mitochondrial DNA–Protein Cross-Links from Mammalian Cells. *DNA* **2022**, *2* (4), 264–278. DIO. 10.3390/dna2040019.

(23) Kaufman, B. A.; Durisic, N.; Mativetsky, J. M.; Costantino, S.; Hancock, M. A.; Grutter, P.; Shoubridge, E. A. The Mitochondrial Transcription Factor TFAM Coordinates the Assembly of Multiple DNA Molecules into Nucleoid-like Structures. *Mol Biol Cell* **2007**, *18* (9). DIO. 10.1091/mbc.E07-05-0404.

(24) Hillen, H. S.; Morozov, Y. I.; Sarfallah, A.; Temiakov, D.; Cramer, P. Structural Basis of Mitochondrial Transcription Initiation. *Cell* **2017**, *171* (5), 1072.e10-1081.e10. DIO. 10.1016/J.CELL.2017.10.036.

(25) Zamudio-Ochoa, A.; Morozov, Y. I.; Sarfallah, A.; Anikin, M.; Temiakov, D. Mechanisms of Mitochondrial Promoter Recognition in Humans and Other Mammalian Species. *Nucleic Acids Res* **2022**, *50* (5). DIO. 10.1093/nar/gkac103.

(26) Swenberg, J. A.; Lu, K.; Moeller, B. C.; Gao, L.; Upton, P. B.; Nakamura, J.; Starr, T. B. Endogenous versus Exogenous DNA Adducts: Their Role in Carcinogenesis, Epidemiology, and Risk Assessment. *Toxicological Sciences*. 2011. DIO. 10.1093/toxsci/kfq371.

(27) Manuel, R. C.; Latham, K. A.; Dodson, M. L.; Lloyd, R. S. Involvement of Glutamic Acid 23 in the Catalytic Mechanism of T4 Endonuclease V. *Journal of Biological Chemistry* **1995**, *270* (6). DIO. 10.1074/jbc.270.6.2652.

(28) Vik, E. S.; Alseth, I.; Forsbring, M.; Helle, I. H.; Morland, I.; Luna, L.; Bjørås, M.; Dalhus, B. Biochemical Mapping of Human NEIL1 DNA Glycosylase and AP Lyase Activities. *DNA Repair (Amst)* **2012**, *11* (9). DIO. 10.1016/j.dnarep.2012.07.002.

(29) Li, D.; Lloyd, R. S. Complex Roles of NEIL1 and OGG1: Insights Gained from Murine Knockouts and Human Polymorphic Variants. *DNA 2022, Vol. 2, Pages 279-301* **2022**, *2* (4), 279–301. DIO. 10.3390/DNA2040020.

(30) Kumar, A.; Reed, A. J.; Zahurancik, W. J.; Daskalova, S. M.; Hecht, S. M.; Suo, Z. Interlocking Activities of DNA Polymerase β in the Base Excision Repair Pathway.

Proceedings of the National Academy of Sciences **2022**, *119* (10). DIO. 10.1073/pnas.2118940119.

(31) Sakmar, T. P.; Franke, R. R.; Khorana, H. G. Glutamic Acid-113 Serves as the Retinylidene Schiff Base Counterion in Bovine Rhodopsin. *Proc Natl Acad Sci U S A* **1989**, *86* (21). DIO. 10.1073/pnas.86.21.8309.

(32) Tang, J.; Zhao, W.; Hendricks, N. G.; Zhao, L. High-Resolution Mapping of Amino Acid Residues in DNA-Protein Cross-Links Enabled by Ribonucleotide-Containing DNA. *Anal Chem* **2021**, *93* (39), 13398–13406. DIO. 10.1021/ACS.ANALCHEM.1C03481.

(33) D.A. Case; I.Y. Ben-Shalom; S.R. Brozell; D.S. Cerutti; T.E. Cheatham; III, V. W. D. C.; T.A. Darden; R.E. Duke; D. Ghoreishi; M.K. Gilson; H. Gohlke; A.W. Goetz; D. Greene; R Harris; N. Homeyer; S. Izadi; A. Kovalenko; T. Kurtzman; T.S. Lee; S. LeGrand; P. Li; C. Lin; J. Liu; T. Luchko; R. Luo; D.J. Mermelstein; K.M. Merz; Y. Miao; G. Monard; C. Nguyen; H. Nguyen; I. Omelyan; A. Onufriev; F. Pan; R. Qi; D.R. Roe; A. Roitberg; C. Sagui; S. Schott-Verdugo; J. Shen; C.L. Simmerling; J. Smith; R. Salomon-Ferrer; J. Swails; R.C. Walker; J. Wang; H. Wei; R.M. Wolf; X. Wu; L. Xiao; D.M. York; P.A. Kollman. *AMBER 2018*; 2018.

(34) Maier, J. A.; Martinez, C.; Kasavajhala, K.; Wickstrom, L.; Hauser, K. E.; Simmerling, C. Ff14SB: Improving the Accuracy of Protein Side Chain and Backbone Parameters from Ff99SB. *J Chem Theory Comput* **2015**, *11* (8). DIO. 10.1021/acs.jctc.5b00255.

(35) Ivani, I.; Dans, P. D.; Noy, A.; Pérez, A.; Faustino, I.; Hospital, A.; Walther, J.; Andrio, P.; Goñi, R.; Balaceanu, A.; Portella, G.; Battistini, F.; Gelpí, J. L.; González, C.; Vendruscolo, M.; Laughton, C. A.; Harris, S. A.; Case, D. A.; Orozco, M. Parmbsc1: A Refined Force Field for DNA Simulations. *Nat Methods* **2015**, *13* (1). DIO. 10.1038/nmeth.3658.

(36) Wang, J.; Wolf, R. M.; Caldwell, J. W.; Kollman, P. A.; Case, D. A. Development and Testing of a General Amber Force Field. *J Comput Chem* **2004**, *25* (9). DIO. 10.1002/jcc.20035.

(37) Sagui, C.; Pedersen, L. G.; Darden, T. A. Towards an Accurate Representation of Electrostatics in Classical Force Fields: Efficient Implementation of Multipolar Interactions in Biomolecular Simulations. *Journal of Chemical Physics* **2004**, *120* (1). DIO. 10.1063/1.1630791.

(38) Ryckaert, J. P.; Ciccotti, G.; Berendsen, H. J. C. Numerical Integration of the Cartesian Equations of Motion of a System with Constraints: Molecular Dynamics of n-Alkanes. *J Comput Phys* **1977**, *23* (3). DIO. 10.1016/0021-9991(77)90098-5.

(39) Roe, D. R.; Cheatham, T. E. PTRAJ and CPPTRAJ: Software for Processing and Analysis of Molecular Dynamics Trajectory Data. *J Chem Theory Comput* **2013**, *9* (7). DIO. 10.1021/ct400341p.

(40) Humphrey, W.; Dalke, A.; Schulten, K. VMD: Visual Molecular Dynamics. *J Mol Graph* **1996**, *14* (1). DIO. 10.1016/0263-7855(96)00018-5.

(41) WL, D. The PyMOL Molecular Graphics System. *CCP4 Newsletter On Protein Crystallography* **2002**, *40* (1).

(42) Cuppari, A.; Fernández-Millán, P.; Battistini, F.; Tarrés-Solé, A.; Lyonnais, S.; Iruela, G.; Ruiz-López, E.; Enciso, Y.; Rubio-Cosials, A.; Prohens, R.; Pons, M.; Alfonso, C.; Tóth, K.; Rivas, G.; Orozco, M.; Solà, M. DNA Specificities Modulate the Binding of Human Transcription Factor A to Mitochondrial DNA Control Region. *Nucleic Acids Res* **2019**, *47* (12). DIO. 10.1093/nar/gkz406.

(43) Borch, R. F.; Bernstein, M. D.; Durst, H. D. The Cyanohydridoborate Anion as a Selective Reducing Agent. *J Am Chem Soc* **1971**, *93* (12). DIO. 10.1021/ja00741a013.

(44) Cordes, E. H.; Jencks, W. P. On the Mechanism of Schiff Base Formation and Hydrolysis. *J Am Chem Soc* **1962**, *84* (5). DIO. 10.1021/ja00864a031.

(45) Casey, J. R.; Grinstein, S.; Orlowski, J. Sensors and Regulators of Intracellular PH. *Nature Reviews Molecular Cell Biology*. 2010. DIO. 10.1038/nrm2820.

(46) Xu, W.; Zhao, W.; Morehouse, N.; Tree, M. O.; Zhao, L. Divalent Cations Alter the Rate-Limiting Step of PrimPol-Catalyzed DNA Elongation. *J Mol Biol* **2019**, *431* (4), 673–686. DIO. 10.1016/J.JMB.2019.01.002.

(47) Johnson, K. A.; Simpson, Z. B.; Blom, T. Global Kinetic Explorer: A New Computer Program for Dynamic Simulation and Fitting of Kinetic Data. *Anal Biochem* **2009**, *387* (1). DIO. 10.1016/j.ab.2008.12.024.

(48) Zhao, L.; Pence, M. G.; Eoff, R. L.; Yuan, S.; Fercu, C. A.; Guengerich, F. P. Elucidation of Kinetic Mechanisms of Human Translesion DNA Polymerase κ Using Tryptophan Mutants. *FEBS Journal* **2014**, *281* (19). DIO. 10.1111/febs.12947.

(49) King, G. A.; Hashemi Shabestari, M.; Taris, K. K. H.; Pandey, A. K.; Venkatesh, S.; Thilagavathi, J.; Singh, K.; Krishna Koppisetti, R.; Temiakov, D.; Roos, W. H.; Suzuki, C. K.; Wuite, G. J. L. Acetylation and Phosphorylation of Human TFAM Regulate TFAM-DNA Interactions via Contrasting Mechanisms. *Nucleic Acids Res* **2018**, *46* (7). DIO. 10.1093/nar/gky204.

(50) Johnson, K. A.; Simpson, Z. B.; Blom, T. FitSpace Explorer: An Algorithm to Evaluate Multidimensional Parameter Space in Fitting Kinetic Data. *Anal Biochem* **2009**, *387* (1). DIO. 10.1016/j.ab.2008.12.025.

(51) Cuniasse, P.; Fazakerley, G. V.; Guschlbauer, W.; Kaplan, B. E.; Sowers, L. C. The Abasic Site as a Challenge to DNA Polymerase. A Nuclear Magnetic Resonance Study of G, C and T Opposite a Model Abasic Site. *J Mol Biol* **1990**, *213* (2). DIO. 10.1016/S0022-2836(05)80192-5.

(52) Rachofsky, E. L.; Seibert, E.; Stivers, J. T.; Osman, R.; Ross, J. B. A. Conformation and Dynamics of Abasic Sites in DNA Investigated by Time-Resolved Fluorescence of 2-Aminopurine. *Biochemistry* **2001**, *40* (4). DIO. 10.1021/bi001665g.

(53) Bignon, E.; Claerbout, V. E. P.; Jiang, T.; Morell, C.; Gillet, N.; Dumont, E. Nucleosomal Embedding Reshapes the Dynamics of Abasic Sites. *Sci Rep* **2020**, *10* (1). DIO. 10.1038/s41598-020-73997-y.

(54) Rubio-Cosials, A.; Sidow, J. F.; Jiménez-Menéndez, N.; Fernández-Millán, P.; Montoya, J.; Jacobs, H. T.; Coll, M.; Bernadó, P.; Solà, M. Human Mitochondrial Transcription Factor A Induces a U-Turn Structure in the Light Strand Promoter. *Nat Struct Mol Biol* **2011**, *18* (11). DIO. 10.1038/nsmb.2160.

(55) Whitaker, A. M.; Freudenthal, B. D. APE1: A Skilled Nucleic Acid Surgeon. *DNA Repair*. 2018. DIO. 10.1016/j.dnarep.2018.08.012.

(56) Beard, W. A.; Horton, J. K.; Prasad, R.; Wilson, S. H. Eukaryotic Base Excision Repair: New Approaches Shine Light on Mechanism. *Annu Rev Biochem* **2019**, *88* (1), 137–162. DIO. 10.1146/annurev-biochem-013118-111315.

(57) Sczepanski, J. T.; Wong, R. S.; McKnight, J. N.; Bowman, G. D.; Greenberg, M. M. Rapid DNA-Protein Cross-Linking and Strand Scission by an Abasic Site in a Nucleosome Core Particle. *Proc Natl Acad Sci U S A* **2010**, *107* (52). DIO. 10.1073/pnas.1012860108.

(58) Zhou, C.; Sczepanski, J. T.; Greenberg, M. M. Mechanistic Studies on Histone Catalyzed Cleavage of Apyrimidinic/Apurinic Sites in Nucleosome Core Particles. *J Am Chem Soc* **2012**, *134* (40). DIO. 10.1021/ja306858m.

(59) Price, N. E.; Johnson, K. M.; Wang, J.; Fekry, M. I.; Wang, Y.; Gates, K. S. Interstrand DNA-DNA Cross-Link Formation between Adenine Residues and Abasic Sites in Duplex Dna. *J Am Chem Soc* **2014**, *136* (9). DIO. 10.1021/ja410969x.

(60) Catalano, M. J.; Liu, S.; Andersen, N.; Yang, Z.; Johnson, K. M.; Price, N. E.; Wang, Y.; Gates, K. S. Chemical Structure and Properties of Interstrand Cross-Links Formed by

Reaction of Guanine Residues with Abasic Sites in Duplex DNA. *J Am Chem Soc* **2015**, *137* (11). DIO. 10.1021/jacs.5b00669.

(61) Amin, S. B. M.; Islam, T.; Price, N. E.; Wallace, A.; Guo, X.; Gomina, A.; Heidari, M.; Johnson, K. M.; Lewis, C. D.; Yang, Z.; Gates, K. S. Effects of Local Sequence, Reaction Conditions, and Various Additives on the Formation and Stability of Interstrand Cross-Links Derived from the Reaction of an Abasic Site with an Adenine Residue in Duplex DNA. *ACS Omega* **2022**, *7* (41). DIO. 10.1021/acsomega.2c05736.

(62) Haldar, T.; Jha, J. S.; Yang, Z.; Nel, C.; Housh, K.; Cassidy, O. J.; Gates, K. S. Unexpected Complexity in the Products Arising from NaOH-, Heat-, Amine-, and Glycosylase-Induced Strand Cleavage at an Abasic Site in DNA. *Chem Res Toxicol* **2022**, *35* (2). DIO. 10.1021/acs.chemrestox.1c00409.

(63) Wei, X.; Wang, Z.; Hinson, C.; Yang, K. Human TDP1, APE1 and TREX1 Repair 3′-DNA–Peptide/Protein Cross-Links Arising from Abasic Sites in Vitro. *Nucleic Acids Res* **2022**, *50* (7), 3638–3657. DIO. 10.1093/NAR/GKAC185.

(64) Ji, S.; Shao, H.; Han, Q.; Seiler, C. L.; Tretyakova, N. Y. Reversible DNA–Protein Cross-Linking at Epigenetic DNA Marks. *Angewandte Chemie - International Edition* **2017**, *56* (45). DIO. 10.1002/anie.201708286.

(65) Zou, G.; Liu, C.; Zeng, W.; Yang, W.; Zhang, K.; Xie, Y.; Chen, C.; Zhou, X. Regulable Dna-Protein Interactions in Vitro and Vivo at Epigenetic Dna Marks. *CCS Chemistry* **2020**, *2* (2). DIO. 10.31635/ccschem.020.201900078.

(66) Yang, K.; Greenberg, M. M. Histone Tail Sequences Balance Their Role in Genetic Regulation and the Need To Protect DNA against Destruction in Nucleosome Core Particles Containing Abasic Sites. *ChemBioChem* **2019**, *20* (1). DIO. 10.1002/cbic.201800559.

(67) Slupphaug, G.; Mol, C. D.; Kavli, B.; Arvai, A. S.; Krokan, H. E.; Tainer, J. A. A Nucleotide-Flipping Mechanism from the Structure of Human Uracil-DNA Glycosylase Bound to DNA. *Nature* **1996**, *384* (6604). DIO. 10.1038/384087a0.

(68) Hollis, T.; Ichikawa, Y.; Ellenberger, T. DNA Bending and a Flip-out Mechanism for Base Excision by the Helix-Hairpin-Helix DNA Glycosylase, Escherichia Coli AlkA. *EMBO Journal* **2000**, *19* (4). DIO. 10.1093/emboj/19.4.758.

(69) Freudenthal, B. D.; Beard, W. A.; Cuneo, M. J.; Dyrkheeva, N. S.; Wilson, S. H. Capturing Snapshots of APE1 Processing DNA Damage. *Nat Struct Mol Biol* **2015**, *22* (11). DIO. 10.1038/nsmb.3105.

(70) Stivers, J. T. Site-Specific DNA Damage Recognition by Enzyme-Induced Base Flipping. *Prog Nucleic Acid Res Mol Biol* **2004**, *77*. DIO. 10.1016/S0079-6603(04)77002-6.

(71) Mullins, E. A.; Rodriguez, A. A.; Bradley, N. P.; Eichman, B. F. Emerging Roles of DNA Glycosylases and the Base Excision Repair Pathway. *Trends in Biochemical Sciences*. 2019. DIO. 10.1016/j.tibs.2019.04.006.

(72) Kozhukhar, N.; Spadafora, D.; Fayzulin, R.; Shokolenko, I. N.; Alexeyev, M. The Efficiency of the Translesion Synthesis across Abasic Sites by Mitochondrial DNA Polymerase Is Low in Mitochondria of 3T3 Cells. *Mitochondrial DNA Part A* **2016**, *27* (6), 4390–4396. DIO. 10.3109/19401736.2015.1089539.

Chapter 3: Mitochondrial transcription factor A (TFAM) has 5′-deoxyribose phosphate lyase activity in vitro

3.1 Introduction

Human mitochondrial DNA (mtDNA) is a circular DNA molecule with 16,569 base pairs. mtDNA encodes a set of RNAs and essential protein subunits in the oxidative phosphorylation system. mtDNA is susceptible to genotoxic agents and reactive metabolites and is maintained by DNA repair, mtDNA turnover, and mitochondrial dynamics[1-6]. The susceptibility to genotoxins, multicopy characteristics, and the signaling role of mtDNA in immune response and inflammation have led to the proposed role of mtDNA as a genotoxic stress sensor in cells[7, 8].

A major DNA repair pathway in mitochondria is base excision repair (BER)[9, 10]. A great deal has been learned about BER in the context of nuclear DNA damage and repair [11]. Although BER is considered a coordinated process, certain toxic repair intermediates can accumulate under enzyme deficiency and when the amount of DNA lesions overwhelms the repair capacity[11-13]. One of the repair intermediates is the 5'-deoxyribose phosphate (5'dRp) residue. 5'dRp is mutagenic in cells, resulting in primarily point mutations and deletions, similar to that of AP sites [14]. 5'dRp is sourced from AP endonuclease (APE1)-catalyzed cleavage 5' to the abasic (AP) site (Fig. 3.1A). 5'dRp is subject to spontaneous or enzymatic release. DNA polymerases β (pol β) and λ (pol λ) are the primary dRp lyases in BER in the nucleus[15-17]. In human mitochondria, the major mitochondrial DNA polymerase γ (pol γ) has dRp lyase activities[18]. In addition, pol β has

been shown to localize to mitochondria in certain tissues[19, 20], suggesting a potential role of pol β in dRp removal.

Although the cellular level of 5'dRp residues remains unknown due to the lack of specific detection methods, 5'dRp release is considered the rate-limiting step in BER [21-24]. The biological importance of 5'dRp removal is supported by phenotypes in cell lines and animal models with deficient dRp lyase activities. For instance, the dRp lyase activity of pol β is required to reverse methylating agent hypersensitivity in pol β-null mouse fibroblasts [25], and also contributes to temozolomide resistance in glioma cells [26, 27]. The conditional knock-in mice with a dRp lyase deficient pol β variant (L22P, a gastric cancer-associated variant) exhibit hyperproliferation, DNA double-strand breaks (DSBs), cytosolic DNA-mediated inflammation, and stomach tumors [28-30]. Moreover, live cell imaging studies have demonstrated that the dRp lyase domain of pol β is crucial for its recruitment to sites of DNA base damage and single-strand breaks after micro-irradiation [31]. Lastly, the critical role of the dRp-lyase activity of the DSB repair factor Ku in non-homologous end joining (NHEJ) corroborates the toxicity of 5'-dRp [32].

Steady-state kinetic analysis has demonstrated that the catalytic efficiency of pol γ is approximately 20-fold lower than that of pol β in dRp lyase reactions[18]. The relatively slow removal of dRp by pol γ and the tissue-specific mitochondrial localization of pol β motivated us to explore additional proteins with dRp lyase activities in mitochondria. Herein, we examined a major DNA-packaging protein in human mitochondria, mitochondrial transcription factor A (TFAM). TFAM is abundant enough to coat the entire mtDNA and binds specifically to promotor regions to activate mitochondrial

transcription[33]. In addition, TFAM has been shown to have AP lyase activities and participate in processing AP sites in vitro and in cultured cells to facilitate mtDNA turnover[34, 35]. Considering the common Schiff base chemistry-based mechanism of enzymatic AP lyase and dRp lyase reactions (Fig. 3.2B), we hypothesized that TFAM could act as a dRp lyase. Using DNA substrates containing a site-specific dRp residue, we demonstrate that TFAM has dRp lyase activity with a single-turnover rate comparable to that of pol β, albeit slower than pol λ. The lysine residues of TFAM mediate the reaction via Schiff base chemistry. Overall, these results hint at a potential role of TFAM in preventing the accumulation of toxic DNA repair intermediates.

3.2 Materials and Methods

Reagents

Unless specified otherwise, chemicals were from Sigma Aldrich (St. Louis, MO) or Fisher Scientific at the highest grade. MS grade trypsin was purchased from Fisher Scientific. E. coli BL21 (DE3) competent cells, uracil DNA glycosylase (UDG) (Cat. No M0280S), and nucleoside digestion mix (Cat. No M0649) were from New England Biolabs (Ipswich, MA). Oligodeoxynucleotides were synthesized and HPLC-purified by Integrated DNA Technologies (Coralville, IA). Polymerase β protein was expressed and purified as described[36]. Truncated polymerase λ (residues 245-575) protein was expressed and purified as reported[37].

Electrophoretic mobility shift assay

The assay was performed as previously described [38]. In short, the reaction solution contained 50 mM HEPES pH 7.4, 100 mM NaCl, 0.1 mg/mL BSA and 10 mM MgCl2, 1 μM DNA substrate (THF-containing duplex) and increasing TFAM concentrations. All reactions were prepared on ice and mixed with a loading buffer containing glycerol with bromophenol and xylene-cyanol.

Fluorescence polarization assay

The equilibrium dissociation constant of TFAM binding to DNA substrates was obtained using fluorescence polarization assays. Reaction buffer contained 50 mM HEPES pH 7.4, 100 mM NaCl, 0.1 mg/mL BSA and 10 mM MgCl2. THF-containing substrate S1' was 2 nM, and TFAM concentration varied from 0 nM to 400 nM. The data was fit to the Hill equation, Y = P*Xh/(Kdh + Xh), where the Y axis was the delta polarization (mP); the X axis was TFAM concentration (nM); h was the hill coefficient.

Preparation of 5'dRp-containing DNA substrates

DNA substrates containing a site-specific dRp residue were prepared through annealing three DNA oligomers, followed by enzymatic digestion. The dU-containing precursor substrates consist of a 19-nt label-free oligomer, a 16-nt oligomer with a 5′-phosphorylated deoxyuridineand a 3′-fluorescein (FAM), and a label-free 36-nt as the complementary strand. The molar ratio of 16-nt:19-nt:36-nt oligomers was 1:1:1.2. The oligomers were mixed at a final concentration of 8 μM in 10 mM HEPES, 50 mM NaCl, and 1 mM EDTA. The mixture was heated at 95°C for 10 min before cooling on ice. The heating and cooling cycle was repeated once to achieve the desired annealing yield. To

generate the 5'dRp-containing substrates, the 5'-phosphorylated deoxyuridine residue is enzymatically converted to 5'dRp using UDG. For every pmol of dU-containing DNA, 4 pmol of UDG was used for digestion at 37°C for 20 min to achieve complete conversion. 5'dRp substrates were prepared freshly prior to use due to the short half-life of the dRp group. To remove excess UDG, a 10 μL of UDG digestion reaction mixture was mixed with an equal volume of phenol-chloroform, followed by brief vortexing for a few seconds and centrifugation for 5 min at 20,000 g. The top layer contained the duplex DNA and was purified using a micro-Bio-Spin P6 column (Bio Rad). The column was conditioned using MES buffer (0.5 M, pH 6.5) before loading, and centrifuged for 5 min at 1000 g to remove excess buffer. DNA was eluted using centrifugation for 10 min at 1000 g. Additional MES buffer was added as needed to increase recovery yield. The volume of the eluent was reduced using SpeedVac without drying the sample. The 5'dRp substrates with and without UDG removal showed similar cleavage rates by pol β (Fig. 3.3).

5'dRp lyase reactions

Reactions contained 1 μM 5'dRp-DNA, 50 mM HEPES pH 7.4, 100 mM NaCl, 0.1 mg/mL BSA and 10 mM MgCl2, with or without 25 mM NaBH3CN, in the presence of varying concentrations of TFAM (or pol β, or pol λ). Samples were stored at −80 ◦C after quenching with 0.2 M NaBH4 until electrophoretic analysis. To analyze the DPC formation, a gradient of 10% SDS-glycine (top) and 16% TBE-urea 7 M (bottom) polyacrylamide gel electrophoresis (PAGE) was used. For analysis of the product formation (conversion of 5′dRp to 5′p) using denaturing PAGE, samples were mixed with

a 1.5 vol of the gel loading solution containing 95% (v/v) formamide and 50 mM EDTA are denatured and used for electrophoresis (19% polyacrylamide/bis-acrylamide (19:1), 7 M urea, 38 cm × 30 cm). Gel images were acquired on a Typhoon imager (Cytiva) and quantified using ImageQuant software (Cytiva). Data were graphed using GraphPad Prism (v8.0). The product percent yields as a function of time were fit to a single-exponential function with 100% set as the initial value.

Spontaneous decay of 5'dRp-DNA

1 μM of 5'dRp-DNA was incubated in 50 mM HEPES pH 7.4, 100 mM NaCl, 0.1 mg/mL BSA and 10 mM MgCl2 under 37 °C for varying times. Reaction aliquots were quenched with an equal volume of 0.2 M NaBH4, followed by rapid cooling on ice. Samples were stored at -80 °C until electrophoretic analysis.

Mass spectrometry analysis

Identification of modified amino acid residues in TFAM by mass spectrometry was carried out in 1 μM S1, 2 μM TFAM, 50 mM HEPES pH 7.4, 100 mM NaCl, 0.1 mg/mL BSA and 10 mM MgCl2 in the presence of 25 mM NaBH3CN. The reactions were allowed for 10 min, and products were digested by trypsin in 100 mM Tris-HCl pH 8.0 and 20 mM CaCl2 at 37°C overnight. Samples were treated with nucleoside digestion mix, purified and analyzed by tandem mass spectrometry as described previously[39]. The data search was similar to the published procedures[39] with modifications. Specifically, the beginning residue to search (position 0) was phosphate, and the mass adduct for dRp adduct was 178.0031 m/z. No Michael addiction products or phosphorylated peptides were observed. The data analysis was performed with AP_CrosslinkFinder[39], followed by

manual verification of cross-linked residues and annotation of the MS/MS spectra. For pre-calibration fit peak assignment, MS1 tolerance was set at 8 ppm and MS2 tolerance was set at 200 ppm. Other settings were default. The semi-quantification of cross-linked peptides was based on the integrated peak areas in MS1 spectra.

3.3 Results

Half-life of dRp group and effects of biological thiol, polyamine, and MgCl2.

We prepared DNA substrates containing a site-specific dRp residue through annealing three DNA oligomers (Fig. 3.1B and Fig. 3.4). One of the oligomers contains a 5'-phosphorylated deoxyuridine and a 3'-fluorescein (FAM). The 5'-phosphorylated deoxyuridine residue is used as a precursor to generate 5'dRp via enzymatic cleavage of dU by UDG. 3'-FAM is to follow the dRp lyase reactions in gel electrophoresis. Upon annealing three oligomers and enzymatic digestion by UDG, the nicked DNA substrates containing a 5'dRp residue (S1, S2, and S3 in Fig. 3.1B and Table 3.1) mimic the BER intermediates upon endonucleolytic incision by APE1 at AP sites. Under physiological pH and salt conditions, 5'dRp substrates containing different base pairs 5' to the dRp residue have a half-life of 3 to 4 h (Table 3.2), similar to reported values[40]. Notably, the half-life of the dRp group is about 3-fold longer in the presence of MgCl2 (250 min vs. 86 min without MgCl2, Table 3.2). Therefore, we chose to include MgCl2 in subsequent dRp lyase reactions.

In mitochondrial matrix, the glutathione (GSH) and biological polyamines (e. g, spermine and spermidine) are present in millimolar concentrations[41, 42]. Considering

the the destabilizing effects of spermine on AP sites[43] and the formation of GSH conjugates with certain AP derivatives[35, 44], we examined the half-life of 5'dRp in the presence of GSH or spermine. Whereas the half-life of 5'dRp was largely unaffected by the presence of GSH, spermine led to a dramatic reduction in half-life with all three substrates (Table 3.3 and Figure 3.4), suggesting that 5'dRp is unlikely to accumulate to a significant extent in the presence of spermine. Nonetheless, the interaction of spermine with nucleic acids is modulated by ionic strength [45] and sequence context [46]. Although it is unclear to what extent polyamines are associated with mitochondrial nucleoids, isolated bacterial nucleoids have been shown to have polyamines bound [45]. The effect of polyamines on 5'dRp in mitochondrial nucleoids in vivo remains to be investigated. Interestingly, unlike a previous report [40], no DNA interstrand cross-links were observed with these substrates under conditions similar to those of reported. The discrepancy may result from the different sequence contexts beyond the neighboring nucleotides in the two studies.

TFAM has dRp lyase activity.

To test the dRp lyase activity of TFAM, S1 was mixed with varying concentrations of TFAM. The product yield increased in a TFAM concentration-dependent manner (Figs. 3.1C and 3.1D). Similar experiments were carried out with pol β and pol λ. Of the three proteins, product formation saturated at the lowest protein/DNA ratio (2:1) with pol λ and 1 μM S1. TFAM and pol β required a higher protein/DNA ratio of 10:1 to reach a saturated product yield. The overall yield of the product was highest for pol λ (nearly 100%), followed by TFAM (approximately 50%), and pol β (around 40%).

Based on the observed protein/DNA ratios, we conducted single turnover experiments to characterize the maximal dRp excision rates with three proteins (Table 3.4). The fastest single turnover rate was observed with pol λ. TFAM and pol β showed similar turnover rates, which were approximately 50-fold lower than that of pol λ. Compared to the half-life of 5'dRp in the naked DNA substrate, enzymatic removal of 5'dRp by pol λ resulted in 3 orders of magnitude of reduction in half-life under single turnover conditions. Whereas TFAM and pol β reduced the half-life of 5'dRp by approximately 40-fold. Similarly, comparable reaction rates were observed with substrates S2 and S3 under single turnover conditions in TFAM-mediated dRp lyase reactions (Table 3.4). Together, these data demonstrate that TFAM can serve as a catalyst to facilitate the cleavage of 5'dRp in a nicked substrate. The single turnover rate with TFAM is comparable to that of a prototypical dRp lyase (pol β) in BER, although the rate was slower than that of pol λ.

Formation of Schiff base intermediates in TFAM-catalyzed dRp lyase reactions

To probe the reaction mechanism, we carried out dRp lyase reactions with TFAM in the presence of NaBH3CN (Fig. 3.2A). NaBH3CN is expected to trap any Schiff base intermediates (Fig. 3.2B) via reductive amination and potentially produce DNA-protein (TFAM) cross-links (DPC). Indeed, gel electrophoretic analysis confirmed the formation of DPC, supporting the involvement of TFAM in the reaction. The intensity of DPC peaked at earlier times and then disappeared, consistent with the reversible characteristics of Schiff base intermediates. Notably, DPC was also observed in reactions without NaBH3CN, and the patterns of the DPC intensity change and the overall yield were similar regardless of the presence of NaBH3CN. These results suggest that β-elimination

and subsequent steps are much faster than the Schiff base formation. In addition, reaction products subsequent to the β-elimination step cannot be observed in gels due to the loss of FAM label on the 3' DNA fragment (Fig. 3.2B). Although an alternative explanation could be that DPC does not involve imine, the mass spectrometry data argue otherwise (vide infra). The overall yield of DPC was much lower compared to the DPC formation in TFAM-mediated AP lyase reactions, hinting at the transient nature of the DPC intermediate in TFAM-mediated dRp lyase reactions.

To identify the amino acid residues of TFAM involved in the reaction and to provide direct evidence for Schiff base intermediates, we analyzed the reaction products in the presence of NaBH3CN using tandem mass spectrometry (Figs. 3.2C and 3.2D). A dRp modification of TFAM, indicative a covalent interact of TFAM with dRp, was observed with two lysine residues, i.e., K96 and K136 (Figs. 3.2C and 3.2D). K96 and K136 contained a mass adduct of 178.0031, consistent with Schiff base formation followed by β-elimination (Fig. 3.2B). Based on the integrated peak areas of the precursor ions, the peptide containing K96 was slightly more abundant (57%) than the one containing K136 (43%). This can be explained by the location of K96 in the high mobility group 1 (HMG1) domains in TFAM, which has an overall higher DNA-binding affinity compared to HMG2. It is important to note that TFAM is not enzyme with a defined active site and that alternative protein conformation may exist and affect the local interactions with dRp residues. The involvement of multiple lysine residues could be attributed to alternative binding conformations compared to the reported crystal structures of TFAM:DNA complexes [47], when a higher than saturated concentration of TFAM was

present. We reason that the "catalytic" lysine residues could differ based on the conformation and occupancy of TFAM bound to DNA molecules. The difference in lysine residues in dRp lyase reactions compared to those involved in AP lyase reactions [35] can be explained by the different number of TFAM molecules associated with the DNA substrate. We determined two TFAM molecules bound to S1 under our experimental conditions based on gel mobility shift and fluorescence polarization data (Fig. 3.5). Nonetheless, considering the high abundance of lysine residues in TFAM (15%), these data do not exclude the possible participation of other lysine residues in dRp lyase reactions under alternative conditions and in cells. The mass spectrometry data corroborate the overall low yield of DPC in gel electrophoretic analysis and support the formation of Schiff base intermediates in TFAM-catalyzed dRp lyase reactions.

3.4 Discussion

In conclusion, our results demonstrate the novel dRp lyase activity of TFAM in vitro. Albeit not an enzyme, TFAM shows a dRp-lyase rate comparable to pol β under excess of proteins. The catalytic effect is analogous to what has been observed for histone in nucleosome core particles [48, 49]. Considering that TFAM is abundant enough to cover the entire mtDNA and low stoichiometry of many DNA lesions, the single-turnover experiments likely provide a reasonable estimation of the turnover rate of TFAM to catalyze dRp release. The high abundance of TFAM in mitochondrial nucleoids argues for its higher frequency of encountering 5'dRp residues compared to pol γ or pol β in cells, suggesting a potential role of TFAM as a noncanonical dRp lyase complementing

pol γ or pol β. Pol λ has not been found to localize to mitochondria. Collectively, the observed dRp lyase activity of TFAM suggests a new role of TFAM in mtDNA repair. Considering the abundance of TFAM in mitochondrial nucleoids, 5'dRp residues are unlikely to accumulate to a significant extent in mtDNA. Nonetheless, the formation of TFAM-dRp adduct in vivo and the impact of such modifications on TFAM functions remain to be investigated.

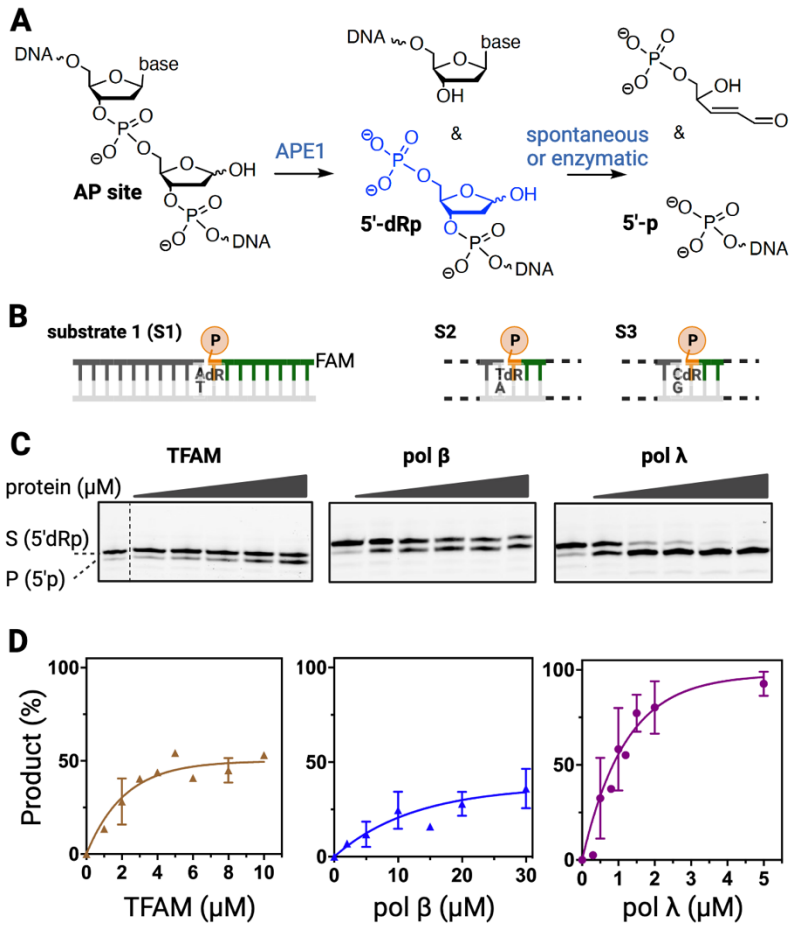

Figure 3.1. dRp lyase reactions via spontaneous decay or protein catalysis. (**A**) Formation of 5'dRp and 5'p residues. (**B**) Carton illustration of DNA substrates; sequence shown in Table 3.1. (**C**) Representative gel image for dRp lyase with varying concentrations of proteins. Reactions contain 1 μM DNA and were allow for 20 min reactions. TFAM was from 0 μM to 10 μM; pol β was from 0 μM to 30 μM; pol λ was from 0 μM to 5 μM. (**D**) Percent yield of product formation with time. Data were average values. Errors indicated the range of data for TFAM (n=2) or S.E. for pol β and pol λ (n=3). All reaction conditions were incubated in 50 mM HEPES pH 7.4, 100 mM NaCl, 0.1 mg/mL BSA and 10 mM MgCl2 at 37°C. Reactions were quenched with 0.2 M $NaBH_4$.

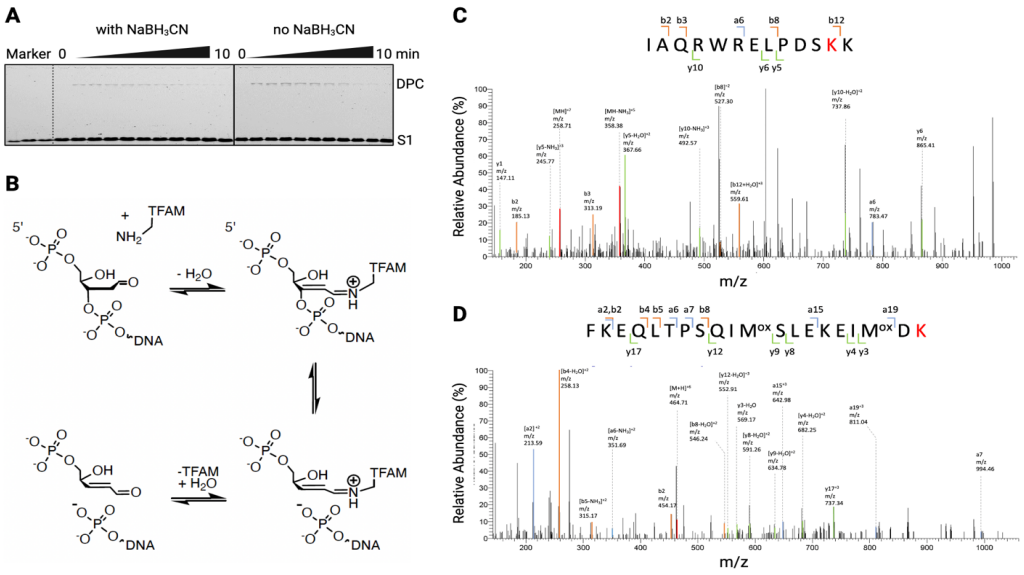

Figure 3.2. Mechanism of TFAM-catalyzed dRp lyase reactions. (**A**) Representative gel image demonstrating the formation of DNA-protein (TFAM) cross-links (DPCs). Reactions contained 1 µM DNA and 2 µM TFAM was incubated for 10 min with or without NaBH3CN. Products were separated on a stacking PAGE with the top layer containing 10% Tris-glycine polyacrylamide gel with 10% SDS and the bottom layer containing 16% TBE 7 M Urea. The running buffer was 0.5X SDS-Glycine and 0.5X TBE. Reactions were carried out in 50 mM HEPES pH 7.4, 100 mM NaCl, 0.1 mg/mL BSA and 10mM MgCl2 at 37°C, quenched with 0.2 M NaBH4. (**B**) Proposed mechanism of lysine catalyzed dRp lyase reactions. (**C**) and (**D**) are tandem mass spectrometry spectra of peptides with a dRp modification at K96 and K136, respectively. MOX indicates an oxidized methionine with a mass adduct of 15.9949.

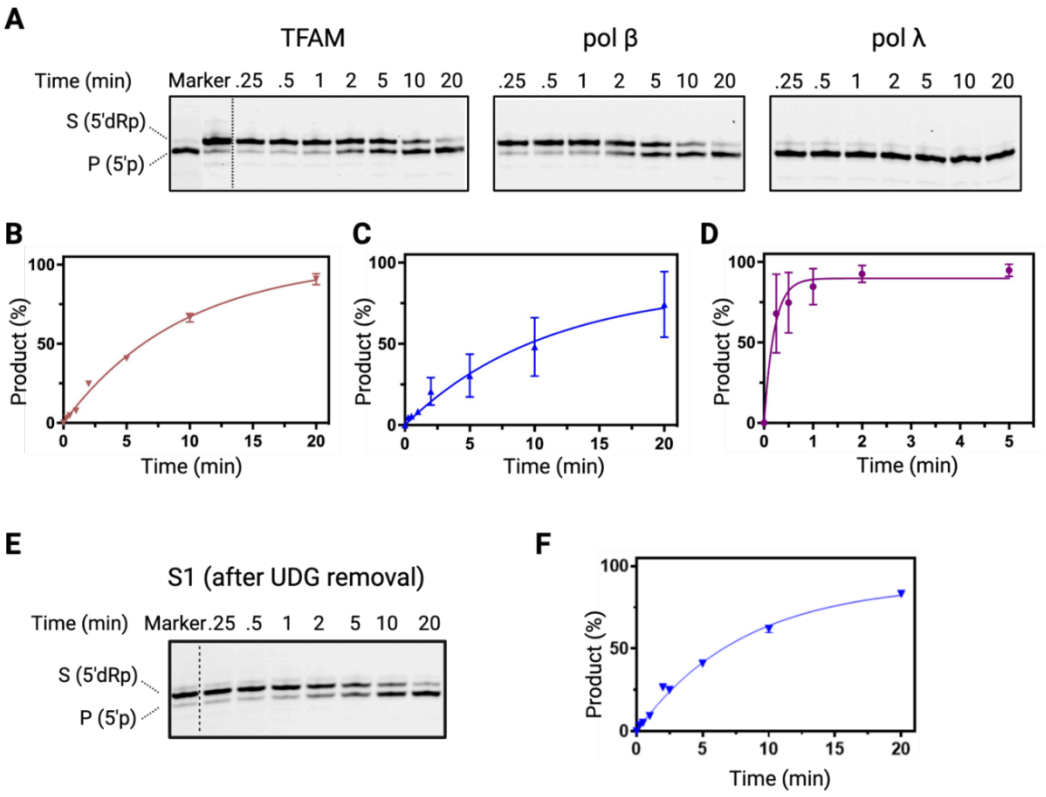

Figure 3.3. Comparison of rates of 5'dRp lyase reactions under single-turnover conditions. (**A**) Representative denaturing gel images for 5'dRp lyase reaction products. Reactions contained 10 µM TFAM, 10 µM pol β, or 2 µM of pol λ in the presence of 1 µM S1. (**B**), (**C**) and (**D**) Fitting product percent yields to an exponential equation gave reaction rates. Data are average values. Error bars represent S.E. (n=4). (**E**) Representative denaturing gel image for 5'dRp lyase reaction with 10 µM pol β and 1 µM S1 after the removal of excess UDG. (F) Fitting product percent yields to an exponential equation gave reaction rates. The lyase rate was 0.11 ± 0.03 min^{-1} and half-life was 6.4 ± 1.7 min, comparable to the parameters obtained with S1 without removing excess UDG (Table 1). Data are average values. Error bars represent S.E. (n=3).

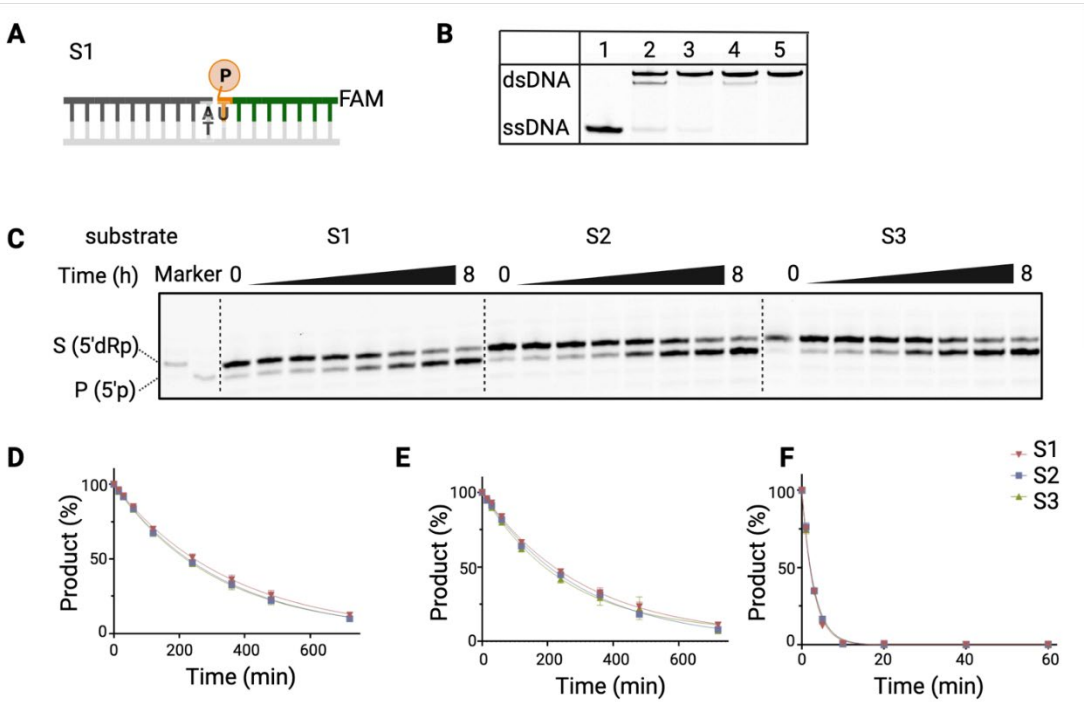

Figure 3.4. (**A**) Cartoon illustration of DNA substrate S1 composed of three oligomers. Reactions follow the conversion of 16-mer oligomer (green) with a 5'p, a deoxyuridine (precursor of AP sites), and 3'FAM label. (**B**) Representative native gel image demonstrating the optimized annealing of S1 precursor (dU). Lane 1: FAM-labeled 16-mer oligomer; Lanes 2 through 5: oligomers mixed at different molar ratios to optimized the yield of double-stranded substrate. Molar ratios for 16-mer:19-mer:36-mer oligomers are 1:1:1 in lane 2, 1:1:1.2 in lane 3, 1:1.1:1.2 in lane 4, and 1:1:1.3 in lane 5. (**C**) Representative gel images of DNA spontaneous decay with three substrates. Representative plot for DNA spontaneous decay under **(D)** 50 mM HEPES pH 7.4, 100 mM NaCl, 0.1 mg/mL BSA and 10 mM $MgCl_2$, **(E)** conditions under (D) with 10 mM GSH, and (**F**) conditions under (D) with 1 mM spermine. Plots were average data from 2 independent experiments; errors represent the range of data.

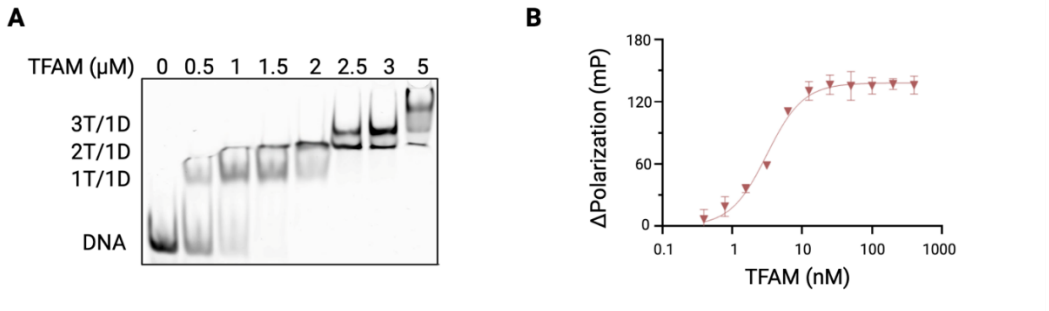

Figure 3.5. TFAM binding to substrate S1'. (**A**) Gel mobility shift assay demonstrates that there can be two TFAM molecules bound to DNA in the presence of 1 μM S1' and 2 μM TFAM (mass spectrometry reaction conditions). (**B**) Fluorescence polarization assay of TFAM binding to S1'. Data were fit to the Hill equation to yield a $K_{d,DNA}$ of 3.1 ± 0.1 nM and a Hill coefficient of 1.7 ± 0.3. The Hill coefficient indicates positive cooperativity of TFAM bound to S1'. Data are average values; errors are S.E. (n=3).

Table 3.1. Sequence of DNA substrates. Each substrate contains three oligomers annealed before the cleavage of the deoxyuridine-containing precursor using UDG to generate a 5'dRp residue. The nicked substrates mimic the repair intermediate upon APE1 cleavage of AP sites. Substrate S1' was used for DNA-binding analysis (Figure 3.5). X indicates a stabilized tetrahydrofuran (THF) analogue.

Substrate	Sequence
S1	5'- GCGGTATGCACTTTTAACA|dRpTCACCCCCCAACTAAC-FAM
	3'- CGCCATACGTGAAAATTG**T**——AAGTGGGGGGTTGATTG
S2	5'- GCGGTATGCACTTTTAAC**T**|dRpTCACCCCCCAACTAAC-FAM
	3'- CGCCATACGTGAAAATTG**A**——AAGTGGGGGGTTGATTG
S3	5'- GCGGTATGCACTTTTAAC**C**|dRpTCACCCCCCAACTAAC-FAM
	3'- CGCCATACGTGAAAATTG**G**——AAGTGGGGGGTTGATTG
S1'	5'- GCGGTATGCACTTTTAACA| pXTCACCCCCCAACTAAC-FAM
	3'- CGCCATACGTGAAAATTG**T**——AAGTGGGGGGTTGATTG

Table 3.2. Effects of Mg^{2+} on the spontaneous decay of the dRp group with DNA substrate S1. The rate of disappearance (k_{dis}) was obtained by fitting the product yield to an exponential equation. Data with 10 mM $MgCl_2$ represent average values from two independent experiments with errors indicating the range of data. Data obtained in the absence of $MgCl_2$ are average values from three independent experiments with errors indicating standard deviations.

	Conditions	**$MgCl_2$**	**k_{dis} (10^{-3} min^{-1})**	**$t_{1/2}$ (min)**
S1	spontaneous	+	2.7 ± 0.2	250 ± 23
	10 mM GSH	+	3.2 ± 0.1	220 ± 8
	1 mM spermine	+	360 ± 3	1.9 ± 0.02
S1	spontaneous	-	8.6 ± 2.3	86 ± 26
	10 mM GSH	-	2.9 ± 0.3	240 ± 27
	1 mM spermine	-	714 ± 2.8	0.97 ± 0.003

Table 3.3. Spontaneous decay of dRp group in DNA substrates and the effect of GSH and spermine. The rate of disappearance (k_{dis}) of the dRp group, was obtained by fitting the product yield to an exponential equation. Data represent average values from two independent experiments. Errors are range of data.

	Conditions	k_{dis} **(10^{-3} min^{-1})**	$t_{1/2}$ **(min)**
S1	spontaneous	2.7 ± 0.2	250 ± 23
	10 mM GSH	3.2 ± 0.1	220 ± 8
	1 mM spermine	360 ± 3	1.9 ± 0.02
S2	spontaneous	3.1 ± 0.2	230 ± 14
	10 mM GSH	3.4 ± 0.03	204 ± 2
	1 mM spermine	340 ± 9	2.1 ± 0.1
S3	spontaneous	3.1 ± 0.1	220 ± 5
	10 mM GSH	3.8 ± 0.4	180 ± 15
	1 mM spermine	340 ± 18	2.0 ± 0.1

Table 3.4. Effect of protein on the half-life of the dRp group. The rate of dRp lyase (klyase) was obtained under single-turnover conditions with 10 μM TFAM, 10 μM pol β, or 2 μM of pol λ in the presence of 1 μM S1. Representative gel images are shown in Fig.3.3.

Protein	Rate and half-life		free DNA $t_{1/2}$ (min)	fold reduction in $t_{1/2}$ relative to free DNA
	k_{lyase} (min^{-1})	$t_{1/2}$ (dRp group, min)		
TFAM	0.10 ± 0.01	6.9 ± 0.9		37
pol β	0.13 ± 0.04	5.8 ± 2.7	250 ± 23	44
pol λ	6.5 ± 0.5	0.2 ± 0.1		1270

Table 3.5. Rates of TFAM-mediated dRp lyase reactions with DNA substrates S1, S2, S3, compared to the half-life of dRp in free DNA. The rate of dRp lyase (k_{lyase}) was obtained under single-turnover conditions with 10 μM TFAM in the presence of 1 μM S1, S2 or S3. Data with S1 were average values with standard deviations (n=4). Data with S2 and S3 were average values with the range of data (n=2). Representative gel images are shown in Fig. S2.

Protein	Rate and half-life		free DNA $t_{1/2}$ (min)	fold reduction in $t_{1/2}$ relative to free DNA
	k_{lyase} (min^{-1})	$t_{1/2}$ (dRp group, min)		
S1	0.10 ± 0.01	6.9 ± 0.9	250 ± 23	36
S2	0.11 ± 0.002	6.3 ± 0.1	230 ± 14	37
S3	0.12 ± 0.01	6.0 ± 0.7	220 ± 5	37

References

(1) Alexeyev, M.; Shokolenko, I.; Wilson, G.; LeDoux, S. The Maintenance of Mitochondrial DNA Integrity--Critical Analysis and Update. *Cold Spring Harb Perspect Biol* 2013, *5* (5). DIO. 10.1101/CSHPERSPECT.A012641.

(2) Shokolenko, I. N.; Alexeyev, M. F. Mitochondrial DNA: A Disposable Genome? *Biochimica et Biophysica Acta - Molecular Basis of Disease*. 2015. DIO. 10.1016/j.bbadis.2015.05.016.

(3) Zhao, L. Mitochondrial DNA Degradation: A Quality Control Measure for Mitochondrial Genome Maintenance and Stress Response. *Enzymes* 2019, *45*, 311–341. DIO. 10.1016/BS.ENZ.2019.08.004.

(4) Scheibye-Knudsen, M.; Fang, E. F.; Croteau, D. L.; Wilson, D. M.; Bohr, V. A. Protecting the Mitochondrial Powerhouse. *Trends in Cell Biology*. 2015. DIO. 10.1016/j.tcb.2014.11.002.

(5) Gustafsson, C. M.; Falkenberg, M.; Larsson, N. G. Maintenance and Expression of Mammalian Mitochondrial DNA. *Annu Rev Biochem* 2016, *85*. DIO. 10.1146/annurev-biochem-060815-014402.

(6) Zhao, L.; Sumberaz, P. Mitochondrial DNA Damage: Prevalence, Biological Consequence, and Emerging Pathways. *Chemical Research in Toxicology*. American Chemical Society October 19, 2020, pp 2491–2502. DIO. 10.1021/acs.chemrestox.0c00083.

(7) Wu, Z.; Sainz, A. G.; Shadel, G. S. Mitochondrial DNA: Cellular Genotoxic Stress Sentinel. *Trends Biochem Sci* 2021, *46* (10), 812–821. DIO. 10.1016/j.tibs.2021.05.004.

(8) Newman, L. E.; Shadel, G. S. Mitochondrial DNA Release in Innate Immune Signaling. *Annual Review of Biochemistry*. 2023. DIO. 10.1146/annurev-biochem-032620-104401.

(9) Prakash, A.; Doublié, S. Base Excision Repair in the Mitochondria. *J Cell Biochem* 2015, *116* (8), 1490–1499. DIO. 10.1002/jcb.25103.

(10) Alencar, R. R.; Batalha, C. M. P. F.; Freire, T. S.; de Souza-Pinto, N. C. Enzymology of Mitochondrial DNA Repair. In *Enzymes*; 2019; Vol. 45. DIO. 10.1016/bs.enz.2019.06.002.

(11) Beard, W. A.; Horton, J. K.; Prasad, R.; Wilson, S. H. Eukaryotic Base Excision Repair: New Approaches Shine Light on Mechanism. *Annu Rev Biochem* 2019, *88* (1), 137–162. DIO. 10.1146/annurev-biochem-013118-111315.

(12) Andres, S. N.; Schellenberg, M. J.; Wallace, B. D.; Tumbale, P.; Scott Williams, R. Recognition and Repair of Chemically Heterogeneous Structures at DNA Ends. *Environ Mol Mutagen* 2015, *56* (1). DIO. 10.1002/em.21892.

(13) Whitaker, A. M.; Schaich, M. A.; Smith, M. S.; Flynn, T. S.; Freudenthal, B. D. Base Excision Repair of Oxidative DNA Damage: From Mechanism to Disease. *Frontiers in Bioscience - Landmark* 2017, *22* (9). DIO. 10.2741/4555.

(14) Simonelli, V.; Narciso, L.; Dogliotti, E.; Fortini, P. Base Excision Repair Intermediates Are Mutagenic in Mammalian Cells. *Nucleic Acids Res* 2005, *33* (14). DIO. 10.1093/nar/gki749.

(15) García-Díaz, M.; Bebenek, K.; Kunkel, T. A.; Blanco, L. Identification of an Intrinsic 5′-Deoxyribose-5-Phosphate Lyase Activity in Human DNA Polymerase λ: A Possible Role in Base Excision Repair. *Journal of Biological Chemistry* 2001, *276* (37), 34659–34663. DIO. 10.1074/JBC.M106336200.

(16) Price, A.; Lindahl, T. Enzymatic Release of 5'-Terminal Deoxyribose Phosphate Residues from Damaged DNA in Human Cells. *Biochemistry* 1991, *30* (35), 8631–8637. DIO. 10.1021/bi00099a020.

(17) Matsumoto, Y.; Kim, K. Excision of Deoxyribose Phosphate Residues by DNA Polymerase β during DNA Repair. *Science (1979)* 1995, *269* (5224). DIO. 10.1126/science.7624801.

(18) Longley, M. J.; Prasad, R.; Srivastava, D. K.; Wilson, S. H.; Copeland, W. C. Identification of 5′-Deoxyribose Phosphate Lyase Activity in Human DNA Polymerase γ and Its Role in Mitochondrial Base Excision Repair in Vitro. *Proc Natl Acad Sci U S A* 1998, *95* (21), 12244–12248. DIO. 10.1073/pnas.95.21.12244.

(19) Sykora, P.; Kanno, S.; Akbari, M.; Kulikowicz, T.; Baptiste, B. A.; Leandro, G. S.; Lu, H.; Tian, J.; May, A.; Becker, K. A.; Croteau, D. L.; Wilson, D. M.; Sobol, R. W.; Yasui, A.; Bohr, V. A. DNA Polymerase Beta Participates in Mitochondrial DNA Repair. *Mol Cell Biol* 2017, *37* (16), 237–254. DIO. 10.1128/MCB.00237-17.

(20) Prasad, R.; Çağlayan, M.; Dai, D. P.; Nadalutti, C. A.; Zhao, M. L.; Gassman, N. R.; Janoshazi, A. K.; Stefanick, D. F.; Horton, J. K.; Krasich, R.; Longley, M. J.; Copeland, W. C.; Griffith, J. D.; Wilson, S. H. DNA Polymerase β: A Missing Link of the Base Excision Repair Machinery in Mammalian Mitochondria. *DNA Repair (Amst)* 2017, *60* (October), 77–88. DIO. 10.1016/j.dnarep.2017.10.011.

(21) Prasad, R.; Beard, W. A.; Strauss, P. R.; Wilson, S. H. Human DNA Polymerase β Deoxyribose Phosphate Lyase: Substrate Specificity and Catalytic Mechanism. *Journal of Biological Chemistry* 1998, *273* (24), 15263–15270. DIO. 10.1074/jbc.273.24.15263.

(22) Srivastava, D. K.; Vande Berg, B. J.; Prasad, R.; Molina, J. T.; Beard, W. A.; Tomkinson, A. E.; Wilson, S. H. Mammalian Abasic Site Base Excision Repair: Identification of the Reaction Sequence and Rate-Determining Steps. *Journal of Biological Chemistry* 1998, *273* (33), 21203–21209. DIO. 10.1074/jbc.273.33.21203.

(23) Wang, Z.; Wu, X.; Friedberg, E. C. Molecular Mechanism of Base Excision Repair of Uracil-Containing DNA in Yeast Cell-Free Extracts. *Journal of Biological Chemistry* 1997, *272* (38), 24064–24071. DIO. 10.1074/jbc.272.38.24064.

(24) Kumar, A.; Reed, A. J.; Zahurancik, W. J.; Daskalova, S. M.; Hecht, S. M.; Suo, Z. Interlocking Activities of DNA Polymerase β in the Base Excision Repair Pathway. *Proceedings of the National Academy of Sciences* 2022, *119* (10). DIO. 10.1073/pnas.2118940119.

(25) Sobol, R. W.; Prasad, R.; Evenski, A.; Baker, A.; Yang, X. P.; Horton, J. K.; Wilson, S. H. The Lyase Activity of the DNA Repair Protein β-Polymerase Protects from DNA-Damage-Induced Cytotoxicity. *Nature 2000 405:6788* 2000, *405* (6788), 807–810. DIO. 10.1038/35015598.

(26) Trivedi, R. N.; Almeida, K. H.; Fornsaglio, J. L.; Schamus, S.; Sobol, R. W. The Role of Base Excision Repair in the Sensitivity and Resistance to Temozolomide-Mediated Cell Death. *Cancer Res* 2005, *65* (14). DIO. 10.1158/0008-5472.CAN-05-0715.

(27) Tang, J. B.; Svilar, D.; Trivedi, R. N.; Wang, X. H.; Goellner, E. M.; Moore, B.; Hamilton, R. L.; Banze, L. A.; Brown, A. R.; Sobol, R. W. N-Methylpurine DNA Glycosylase and DNA Polymerase β Modulate BER Inhibitor Potentiation of Glioma Cells to Temozolomide. *Neuro Oncol* 2011, *13* (5). DIO. 10.1093/neuonc/nor011.

(28) Dalal, S.; Chikova, A.; Jaeger, J.; Sweasy, J. B. The Leu22Pro Tumor-Associated Variant of DNA Polymerase Beta Is DRP Lyase Deficient. *Nucleic Acids Res* 2008, *36* (2). DIO. 10.1093/nar/gkm1053.

(29) Zhao, S.; Klattenho, A. W.; Thakur, M.; Sebastian, M.; Kidane, D. Mutation in Dna Polymerase Beta Causes Spontaneous Chromosomal Instability and Inflammation-Associated Carcinogenesis in Mice. *Cancers (Basel)* 2019, *11* (8). DIO. 10.3390/cancers11081160.

(30) Zhao, S.; Goewey Ruiz, J. A.; Sebastian, M.; Kidane, D. Defective DNA Polymerase Beta Invoke a Cytosolic DNA Mediated Inflammatory Response. *Front Immunol* 2022, *13*. DIO. 10.3389/fimmu.2022.1039009.

(31) Lan, L.; Nakajima, S.; Oohata, Y.; Takao, M.; Okano, S.; Masutani, M.; Wilson, S. H.; Yasui, A. In Situ Analysis of Repair Processes for Oxidative DNA Damage in

Mammalian Cells. *Proc Natl Acad Sci U S A* 2004, *101* (38). DIO. 10.1073/pnas.0406048101.

(32) Roberts, S. A.; Strande, N.; Burkhalter, M. D.; Strom, C.; Havener, J. M.; Hasty, P.; Ramsden, D. A. Ku Is a 5'dRP/AP Lyase That Excises Nucleotide Damage near Broken Ends. *Nature* 2010, *464* (7292), 1214. DIO. 10.1038/NATURE08926.

(33) Oliver, J.; Torrens-Mas, M.; Kozhukhar, N.; Alexeyev, M. F. 35 Years of TFAM Research: Old Protein, New Puzzles. *Biology 2023, Vol. 12, Page 823* 2023, *12* (6), 823. DIO. 10.3390/BIOLOGY12060823.

(34) Xu, W.; Boyd, R. M.; Tree, M. O.; Samkari, F.; Zhao, L. Mitochondrial Transcription Factor A Promotes DNA Strand Cleavage at Abasic Sites. *Proceedings of the National Academy of Sciences* 2019, *116* (36), 17792–17799. DIO. 10.1073/pnas.1911252116.

(35) Xu, W.; Tang, J.; Zhao, L. DNA–Protein Cross-Links between Abasic DNA Damage and Mitochondrial Transcription Factor A (TFAM). *Nucleic Acids Res* 2023, *51* (1), 41–53. DIO. 10.1093/nar/gkac1214.

(36) Fairlamb, M. S.; Spies, M.; Washington, M. T.; Freudenthal, B. D. Visualizing the Coordination of Apurinic/Apyrimidinic Endonuclease (APE1) and DNA Polymerase β during Base Excision Repair. *Journal of Biological Chemistry* 2023, *299* (5). DIO. 10.1016/j.jbc.2023.104636.

(37) Fiala, K. A.; Abdel-Gawad, W.; Suo, Z. Pre-Steady-State Kinetic Studies of the Fidelity and Mechanism of Polymerization Catalyzed by Truncated Human DNA Polymerase λ. *Biochemistry* 2004, *43* (21). DIO. 10.1021/bi049975c.

(38) Zhao, W.; Xu, W.; Tang, J.; Kaushik, S.; Chang, C.-E. A.; Zhao, L. Key Amino Acid Residues of Mitochondrial Transcription Factor A Synergize with Abasic (AP) Site Dynamics To Facilitate AP-Lyase Reactions. *ACS Chem Biol* 2023, *18* (5), 1168–1179. DIO. 10.1021/acschembio.3c00047.

(39) Tang, J.; Zhao, W.; Hendricks, N. G.; Zhao, L. High-Resolution Mapping of Amino Acid Residues in DNA-Protein Cross-Links Enabled by Ribonucleotide-Containing DNA. *Anal Chem* 2021, *93* (39), 13398–13406. DIO. 10.1021/ACS.ANALCHEM.1C03481.

(40) Admiraal, S. J.; O'Brien, P. J. Reactivity and Cross-Linking of 5′-Terminal Abasic Sites within DNA. *Chem Res Toxicol* 2017, *30* (6), 1317–1326. DIO. 10.1021/acs.chemrestox.7b00057.

(41) Marí, M.; Morales, A.; Colell, A.; García-Ruiz, C.; Fernández-Checa, J. C. Mitochondrial Glutathione, a Key Survival Antioxidant. *Antioxidants and Redox Signaling*. 2009. DIO. 10.1089/ars.2009.2695.

(42) Hoshino, K.; Momiyama, E.; Yoshida, K.; Nishimura, K.; Sakai, S.; Toida, T.; Kashiwagi, K.; Igarashi, K. Polyamine Transport by Mammalian Cells and Mitochondria: Role of Antizyme and Glycosaminoglycans. *Journal of Biological Chemistry* 2005, *280* (52). DIO. 10.1074/jbc.M505445200.

(43) Haldar, T.; Jha, J. S.; Yang, Z.; Nel, C.; Housh, K.; Cassidy, O. J.; Gates, K. S. Unexpected Complexity in the Products Arising from NaOH-, Heat-, Amine-, and Glycosylase-Induced Strand Cleavage at an Abasic Site in DNA. *Chem Res Toxicol* 2022, *35* (2). DIO. 10.1021/acs.chemrestox.1c00409.

(44) Jha, J. S.; Yin, J.; Haldar, T.; Yang, Z.; Wang, Y.; Gates, K. S. Reconsidering the Chemical Nature of Strand Breaks Derived from Abasic Sites in Cellular DNA: Evidence for 3′-Glutathionylation. *J Am Chem Soc* 2022, *144* (23). DIO. 10.1021/jacs.2c02703.

(45) Rubin, R. L. Spermidine Deoxyribonucleic Acid Interaction in Vitro and in Escherichia Coli. *J Bacteriol* 1977, *129* (2). DIO. 10.1128/jb.129.2.916-925.1977.

(46) Perepelytsya, S.; Uličný, J.; Laaksonen, A.; Mocci, F. Pattern Preferences of DNA Nucleotide Motifs by Polyamines Putrescine2+, Spermidine3+ and Spermine4+. *Nucleic Acids Res* 2019, *47* (12). DIO. 10.1093/NAR/GKZ434.

(47) Rubio-Cosials, A.; Sidow, J. F.; Jiménez-Menéndez, N.; Fernández-Millán, P.; Montoya, J.; Jacobs, H. T.; Coll, M.; Bernadó, P.; Solà, M. Human Mitochondrial Transcription Factor A Induces a U-Turn Structure in the Light Strand Promoter. *Nat Struct Mol Biol* 2011, *18* (11). DIO. 10.1038/nsmb.2160.

(48) Rodriguez, Y.; Howard, M. J.; Cuneo, M. J.; Prasad, R.; Wilson, S. H. Unencumbered Pol β Lyase Activity in Nucleosome Core Particles. *Nucleic Acids Res* 2017, *45* (15). DIO. 10.1093/nar/gkx593.

(49) Ren, M.; Shang, M.; Wang, H.; Xi, Z.; Zhou, C. Histones Participate in Base Excision Repair of 8-OxodGuo by Transiently Cross-Linking with Active Repair Intermediates in Nucleosome Core Particles. *Nucleic Acids Res* 2021, *49* (1). DIO. 10.1093/nar/gkaa1153.

Chapter 4: Mass Spectrometry Detection of TFAM DPC

4.1 Introduction

Transcription Factor A, Mitochondrial (TFAM) is essential for maintaining the structural and functional integrity of mitochondrial DNA (mtDNA). TFAM binds to mtDNA, organizing it into nucleoids that protect the DNA from damage while ensuring efficient replication and transcription. This role is important not only for maintaining mitochondrial function, but also for the regulation of gene expression necessary for mitochondrial operations[1]. Moreover, TFAM is vital for the repair and ongoing maintenance of mtDNA, highlighting its importance in sustaining mitochondrial health and preventing cellular aging and disease[2,3].

DNA-protein complexes (DPCs) are crucial cellular structures that play key roles in DNA replication, transcription, and repair. When proteins covalently bind to DNA, these complexes can significantly impact cellular processes, potentially obstructing replication forks and transcription machinery. This obstruction can lead to genomic instability and cellular dysfunction. More critically, DPCs involving Transcription Factor A, Mitochondrial (TFAM) have been associated with significant cellular signaling pathways, such as the cGAS pathway[4,5], suggesting a profound role in immune response and cellular stress mechanisms.

Recent studies in our laboratory have identified TFAM-associated DPCs within mitochondria, with these complexes exhibiting a notable half-life of approximately 40 hours[6,7]. This persistence indicates a substantial impact on mitochondrial function,

particularly affecting transcription due to prolonged blockages. However, current methods for detecting these complexes have been limited to assessing AP sites or measuring relative DPC fold-changes through ELISA, which do not provide direct, molecular-level insights into the abundance and nature of TFAM DPCs.

To address these limitations, this project focused on developing a mass spectrometry-based method tailored for analyzing TFAM interactions with AP-containing λ DNA, which can be adopted for analyzing cellular mtDNA in the future. This innovative approach seeks to streamline the extraction and quantification of TFAM DPCs using the λ DNA as a proxy for mtDNA. Thus far, I have made progress in optimizing the generation of TFAM DPCs with defined mass adducts, simplifying the mass spectrometry search process. Additionally, I have refined the TFAM DPC extraction method *in vitro* using λ and validated the successful extraction and enrichment of TFAM DPCs using ELISA. The developed sample preparation protocols and data analysis tools will move the project toward the identification of the cross-linked amino acid residues in TFAM DPCs in cellular samples.

4.2 Materials and Methods

Preparation of TFAM DPC using 38mer synthetic oligo

DNA substrates (Table 4.1) containing a site-specific dU residue was prepared through UDG digestion, followed by the annealing DNA oligos like previous studies.[7,8] The 5'FAM-labeled 38mer oligomers were mixed at a final concentration of 8 μM in 10 mM HEPES, 50 mM NaCl, and 1 mM EDTA. To generate the intact TFAM DPC, 4 μM

of N-term-His TFAM was incubated with 1 μM AP-DNA in buffer containing 50 mM HEPES pH 7.4, 100 mM NaCl and 0.1 mg/mL BSA. After 24 hours of reaction at 37 °C, sample was quenched with 0.2 M $NaBH_4$ and stored in -20°C until analysis.

To analyze the DPC formation, a gradient of 4% native (top) and 10% SDS-glycine (bottom) polyacrylamide gel electrophoresis (PAGE), or a 10% SDS-glycine (top) and 19% TBE-Urea PAGE was used. Gel images were acquired on a Typhoon imager (Cytiva) and quantified using ImageQuant software (Cytiva). Data were graphed using GraphPad Prism (v8.0). The product percent yields as a function of time were fit to a single-exponential function with 100% set as the initial value.

Preparation of TFAM DPC using λ DNA

λ DNA-TFAM DPC was generated by incubating purified His-tagged TFAM with AP-containing λ DNA. Intact λ DNA 500ng was treated with 0.1 M phosphate buffer at pH 2.5 for 1 hour at 37 ◦C to generate AP site[9]. Sample was neutralized with carbonated buffer when reaction complete. His-TFAM was added to AP-containing λ DNA with 2 times excess at molar ratio range in a reaction buffer containing HEPES 50mM, NaCl 100mM, and BSA 0.1mg/mL. Sample was incubated at 37°C for 24 hours then quenched with 0.2 M NaBH4 and stored in -20◦C until analysis. The DPC was visualized with a gradient of 4% native (top) and 10% SDS-glycine (bottom) polyacrylamide gel electrophoresis (PAGE). DNA was visualized with cyber gold stain prior to protein staining.

DPC extraction using λ DNA

DPC using λ DNA was extracted with Zymo DNA clean-up column as previously described[10] with slight modification. Briefly, DPC sample 10 μL was added with 1% SDS prior to adding 70 μL DNA binding buffer. Sample was loaded onto the column and centrifuge at 16000g for 1min. The flow-through was added back to the column for a total of 3 times. Then the column was washed with 200 μL washing solution, centrifuge at 16000g for 1min, the eluted washing buffer was added back to the column for a total of 3 times. The DPC containing sample was eluted with 20 μL elution buffer containing 20mM HEPES, 1mM EDTA, 0.1% SDS. Incubate the column at room temperature for 3min, then centrifuge at 16000g for 1min. Re-load the eluent back to the column to increase yield. The DNA concentration was tested using Qubit 4 Fluorometer.

Quantification of DPC by ELISA

The quantification of λ -DNA DPC with ELISA based method was described previously with slight modification[10]. DPC sample was added with 0.1% SDS and diluted to 0.5 ng/μl with the 1×DNA coating solution. To each well of a tissue culture microplate, 60 μl of the diluted DNA solution and 90 μl of DNA coating solution were added. The plate was incubated at room temperature overnight. The solution was aspirated, and the wells were washed with 1× TBST solution 5 times. The blocking was performed with 3% BSA in 1× TBST at room temperature for 1 h. For His-tagged TFAM, Rabbit anti-His antibody (Novus, NBP1-46791) was used with 1/500 dilution at 4°C overnight. For wtTFAM, Rabbit anti-human TFAM antibody (Sino Biological Ink, HD12OC1229) was used with 1/500 dilution at 4°C overnight. After washing with 1×

TBST, the wells were incubated in 1/1000 dilution of Goat Anti-Rabbit IgG-HRP at room temperature for 1 h. The luminescence was obtained from 150 µl of the substrate with a Synergy H1 plate reader. The change fold of the luminescence was normalized to the intensity from 80bp DNA and DPC sample.

Generation of Uniformed DPC Adduct for Mass Spectrometry

To generate a uniformed DPC adduct, we treat Tyrosyl-DNA Phosphodiesterase 1 (TDP1) and AP Endonuclease (APE1) to the intact DPC sample. We analyzed both TDP1 and APE1 for their nuclease activity, where we added increasing amount of TDP1 and APE1 as noted (Fig. 4.1) and incubate at 37°C for various time points. Due to TFAM has a size of 24kDa, which potentially blocks the TDP1 from effectively cleaving the phosphate group, Trypsin digestion was performed prior to TDP1 digestion. For Trypsin digestion, every 1µg of TFAM, add 0.2µg of Trypsin, incubate at 37 °C overnight. After that, the sample was incubated at 65°C to deactivate Trypsin, and TDP1 was added at 1uM DPC: 2uM TDP1 ratio, incubate at 37 °C for 4 hours to cleave the 5'end of AP-DNA.

Mass Spectrum Analysis of TFAM Crosslinks

Identification of modified amino acid residues in TFAM by mass spectrometry was carried out similar as before[8] with slight modifications. DPC sample was digested by Trypsin then TDP1 as described above, then using a P6-spin column to for sample desalt, and finally adding nucleoside digestion mix, purified and analyzed by tandem mass spectrometry as described previously [8]. The data search was done by Frag Pipe and analyzed by GNPS2. The addition of using TDP1 allowed us to see a uniformed mass

adduct of 118.0630 m/z on TFAM peptide. The fragment mass tolerance was set at 20 PPM, while other settings were set as default. The semi-quantification of cross-linked peptides was based on the integrated peak areas in MS1 spectrum.

4.3 Results

Uniformed TFAM DPC analysis and generation using synthetic DNA oligomer.

In this experiment, we used a 38-mer synthetic DNA oligo labeled with 5'FAM, which incorporates the native mitochondrial LSP sequence. To introduce an abasic (AP) site, we enzymatically cleaved a deoxyuridine (dU) base using Uracil-DNA Glycosylase (UDG). Following this modification, we incubated the DNA with his-tagged Transcription Factor A, Mitochondrial (TFAM), overnight to form a DNA-protein complex (DPC). DPC was confirmed using a gradient gel, where it contains 4% native solution on the top layer, ensuring large complex to enter the gel; bottom portion contains TBE-Urea (7M) to effectively separate DNA. Interestingly, we identified a DNA secondary structure formed after incubation, possibly due to the high GC content of the oligo itself resulting in the formation of a G4 structure. The identification of gel band was further verified using Coomassie bule protein staining, proving bands containing protein were all clustered in the top native gel portion.

Using 37mer synthetic substrate and purified His-TFAM, first we want to obtain the intact TFAM-AP-DNA complex (intact DPC). After 24-hour incubation, the sample was treated with $NaBH_4$ to reduce the Schiff-base product. the intact DPC band shows on the native gel portion (Fig. 4.1A). An increasing amount of TDP1 and APE1 were added

to the sample, aiming to cleave the 5'end, resulting in the disappearance of intact DPC band and increasing amount of 20mer band. However, both TDP1 and APE1 failed to convert all intact DPC, where with increasing amount of TDP1, there a trend with decreasing amount of DPC band, however APE1 did not seems to process this DPC well even with increasing amount.

To proceed with TDP1 approach, we increased TPD1 concentration to 10 μM and 20 μM. At this high concentration, although TDP1 successfully converted 97% of intact DPC, with TFAM only 2~4μM the resulting sample would contain too much TDP1 and may interfere with mass spectrometry if not removed properly. To overcome this challenge, the TFAM-DNA complex was treated with Trypsin. This enzymatic digestion was necessary because intact TFAM, with a molecular weight of 25 kDa, was found to inhibit the activity of Tyrosyl-DNA Phosphodiesterase 1 (TDP1). By digesting TFAM into smaller peptides, we enabled TDP1 to access and cleave the 5' end of the oligomer. This cleavage by TDP1 resulted in the formation of a free hydroxyl (OH) group at the 5' end of the DNA within the DPC (Fig 4.2).

The successful generation of a uniform TFAM DPC adduct marks a crucial first step for in-cellular studies, providing a solid foundation for subsequent analyses. With precisely defined reaction conditions, enzyme-to-protein ratios, and total reaction times, we have gained deeper insights into the biochemical interactions within the DPC. Moreover, this knowledge has enhanced our understanding of how structural changes in TFAM influence the efficiency of the enzymatic cleavage process, paving the way for further exploration of mitochondrial DNA maintenance mechanisms.

DPC extraction using His-TFAM and λ DNA

Although TFAM shows preference binding sites for the light strand promoter (LSP) region[13], its binding sites across the entirety of mtDNA are not specific. Therefore, using synthetic oligonucleotides to study TFAM's binding patterns might not accurately reflect its natural behavior at the physiological level. To address this, we are utilizing lambda DNA as a more representative model to mimic the TFAM-AP DNA binding interactions within a cellular context.

To generate AP sites on λ DNA, we employed acid hydrolysis, the AP sites formation was confirmed by our group using ARP assay. We then incubated His-tagged TFAM with AP-λ DNA, and the formation of intact DPCs was confirmed through sequential staining with cyber gold for DNA and Coomassie blue for proteins (Fig. 4.3A). The extracted DPC sample showed smearing bands on the higher molecular weight position upon cyber gold DNA staining; protein staining showed that the majority of 25kDa free His-TFAM were removed. However, since the His-TFAM cross-linking with ununiformed sized nucleotides, the DPC band appeared to be a smear and hard to visualize. We then measured the dsDNA concentration using Qubit and confirmed that extracted DPC sample does contain dsDNA (Fig. 4.3B). Overall, although we observed the disappearance of free TFAM after extraction, and detected λ DNA signal within the extracted DPC fraction, more direct evidence was needed to confirm the successful extraction of the complex containing His-TFAM.

Confirmation of DPC extraction using ELISA

An ELISA-based approach for analyzing TFAM DPC was adopted building from a prior study[12]. Since gel-based method is not suitable to detect low concentration DPC, an alternative approach needs to be investigated. Using ELISA-based method with DNA coating on the plate and specific antibody for protein recognition, the increased luminescent intensity indicates the presence of target protein bound to DNA and recognized by the primary and secondary antibody. Notably, the 80bp DPC showed extremely low signal, whereas the λ DNA DPC displayed a significantly higher signal (Fig. 4.4A). This discrepancy could be due to either low coating efficiency of the 80 bp substrate; or the human TFAM antibody was not functioning properly, since both DPC samples were using the same secondary antibody. After normalizing the luminescent intensity against the control, data was plotted, revealing a generally linear relationship between the sample concentration and signal intensity (Fig. 4.4B). The ELISA result evidently proved that our refined extraction method is effective in isolating TFAM-bound DPCs.

***In-Vitro* Mass Spectrometry Analysis**

To investigate whether the length of a DNA oligomer influences the binding position of TFAM, we performed mass spectrometry analysis using Frag Pipe and GNPS2 on a 38-mer oligonucleotide. Our analysis revealed that the major crosslinking sites are the N-terminal cysteine at position 49 (C49), which showed a peak area of 68.5%, and lysine 69 (K69) within the HMG1 domain, which displayed a peak area of 31.5% (Table 4.2). These findings align well with earlier studies[9,10,14] , which used a

shorter 22-mer oligonucleotide and identified cysteine as the predominant crosslinking site without the use of chemical trapping agents. Additionally, the HMG1 domain has been previously reported to possess a strong binding affinity towards double-stranded DNA.

Given the position of the abasic (AP) site on this 38-mer oligonucleotide, we noted that K69 is in close proximity to the AP site, corroborating the mass spectrometry results. This proximity supports the hypothesis that the length and sequence context of the oligonucleotide can influence TFAM's binding specificity and interaction dynamics, providing valuable insights into the structural aspects of TFAM's interaction with mitochondrial DNA. This study not only confirms previous findings but also expands our understanding of the molecular interactions between TFAM and DNA, which is critical for devising strategies to regulate mitochondrial function and address mitochondrial disorders.

4.5 Discussion

This study contributed to the development of a mass spectrometry-based method tailored for identifying cross-linked amino acids of TFAM DPCs using recombinant TFAM and λ DNA. While TFAM shows preferential binding to the light strand promoter (LSP) region of mtDNA, its interaction across the entirety of mtDNA lacks specificity. To provide a more accurate representation of TFAM's behavior under physiological conditions, we have employed λ (Lambda) DNA. This model, derived from bacteriophage lambda and approximately 48,502 base pairs long, better mimics the

TFAM-AP DNA binding interactions within a cellular setting. The specificity and precision of our mass spectrometry method now allow for detailed examination of these interactions, highlighting the dynamic interplay between TFAM and mitochondrial DNA under physiological conditions.

Moreover, our laboratory has observed significant insights into the role of glutathione (GSH) in competing with TFAM at apurinic/apyrimidinic (AP) sites [6]. Notably, without GSH inhibition, the increase of TFAM-DPC under stress conditions is not significant. This underscores the pivotal role of GSH in competing with TFAM for binding at apurinic/apyrimidinic (AP) sites. Intriguingly, GSH binds to the AP site at the 3' phosphoglycolate (3'pUA) structure only after TFAM is released from the already-formed Schiff-base complex. The formation of GSH DPCs depends on the release of TFAM, with GSH forming a more stable thiol adduct than TFAM. This dynamic is noteworthy, as it may provide another point of explanation with observations that in the cytosol, TFAM interacts with the autophagy-related protein LC3[12]. It is speculated that TFAM may initially bind to fragmented mtDNA, inducing a U-shaped configuration that promotes the recruitment of the cGAS dimer, thereby activating the immune response pathway[13]. However, when GSH binds to the 3'pUA structure following TFAM's release, the now free TFAM is likely to interact with LC3, triggering the autolysosomal pathway. This observation suggests a sophisticated balance between mitochondrial damage responses and cellular homeostatic mechanisms.

Adopting this novel mass spectrometry method for cellular studies enhances our ability to not only study the molecular interactions within mitochondria but also to

compare DPC levels between TFAM and GSH. This method can potentially be modified to detect other DPCs in the future, enhancing our understanding of DPCs in mtDNA stability and function.

Overall, this study has successfully optimized several key steps for a mass spectrometry-based method for analyzing DNA-protein interactions between TFAM and λ DNA. This development is significant as it sets a foundational methodological framework that can potentially be applied to cellular studies involving mitochondrial DNA in the future. While the current research has focused on refining techniques for detecting and analyzing TFAM interactions with λ DNA, it paves the way for future explorations into more complex dynamics, such as interactions between TFAM and glutathione at AP sites within mitochondrial contexts. These applications, along with the quantitative analysis of TFAM-DPC levels and comparative studies with other proteins, remain prospective areas for further investigation. By establishing a robust method for studying TFAM interactions, this research contributes a valuable tool for future studies that aim to deepen our understanding of protein-DNA interactions within cells. The novel insights gained from the chemistry behind the crosslinking sites will elucidate the mechanisms of mtDNA repair and protection. This innovative method opens new avenues for detecting other molecules that form stable crosslinks with AP-DNA in mitochondria, potentially contributing to mtDNA maintenance and shedding light on their critical roles in mitochondrial health and stability.

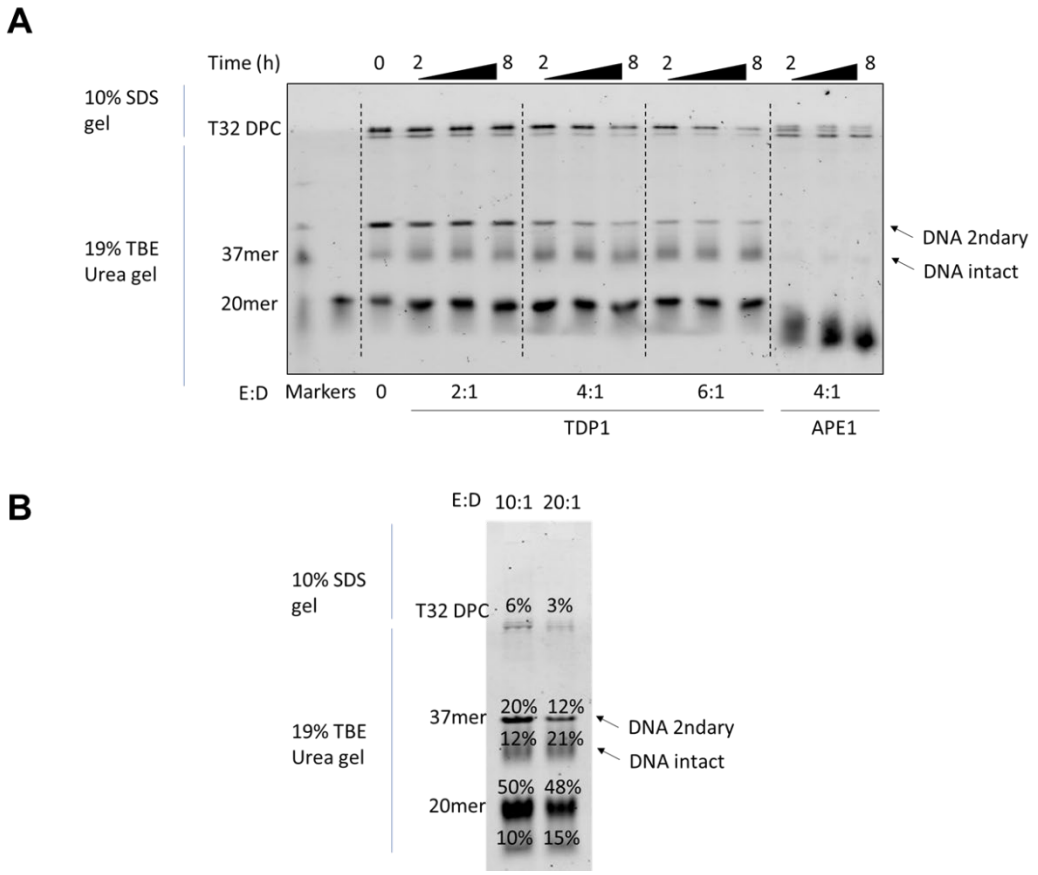

Figure 4.1. DPC formation using synthetic substrate and purified TFAM. (**A**) Representative denaturing gel image for DPC formation. Reaction contains 1 μM substrate and 4 μM of TFAM with incubation at 37°C for 24 hours. The intact DPC products were resulting at the top portion of gel because of the larger size. After that, TDP1 and APE1 were added with increasing amount and with incubation at 37°C for various time points. With increasing concentration of TDP1, DPC were digested (**B**) down to 3%; while APE1 failed to digest DPC sample.

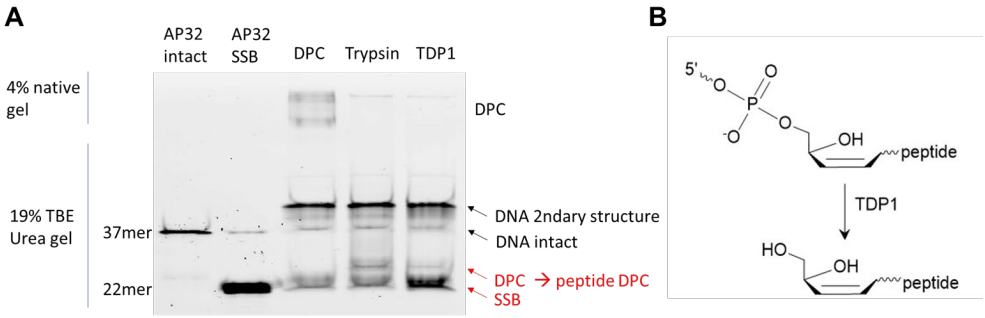

Figure 4.2. Representative gel image (**A**) to visualize 5'FAM labeled AP-DNA, DPC and DPC formation after enzymatic digestion. DPC bands appeared to be at the 4% native portion of the gel and migrated lower to peptide DPC position after Trypsin digestion. After TDP1 digestion, the peptide DPC converted into SSB form, indicating a successful TDP1 cleavage presented by (**B**).

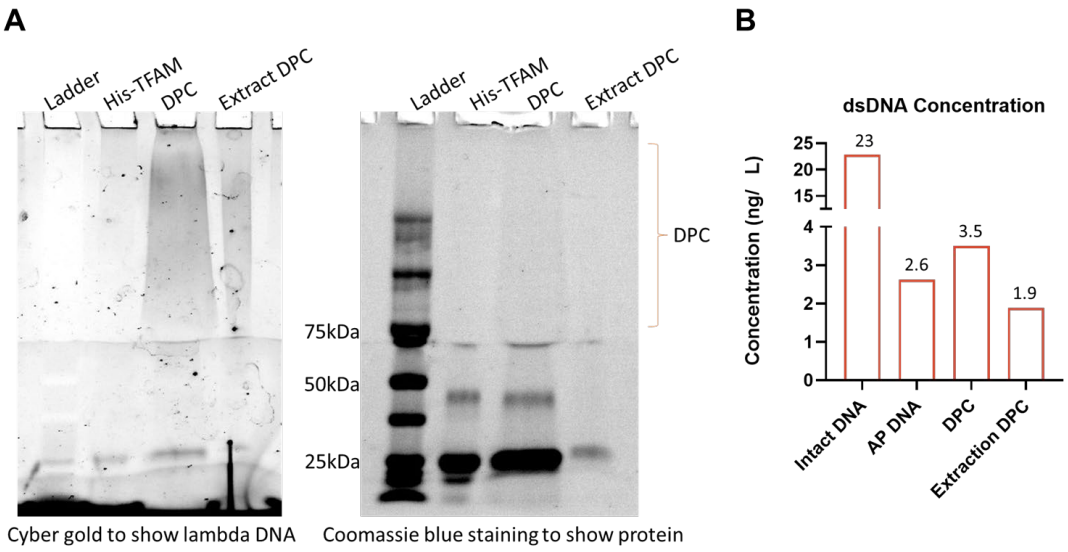

Figure 4.3. Extraction of λ DNA and His-TFAM DPC. Representative gel image of DPC extraction (**A**), with cyber gold staining for DNA and Coomassie blue staining for protein. Qubit high sensitivity dsDNA quantification plot (**B**) for samples: 1) Intact λ DNA, 2) AP λ DNA, 3) DPC sample, 4) DPC after extraction.

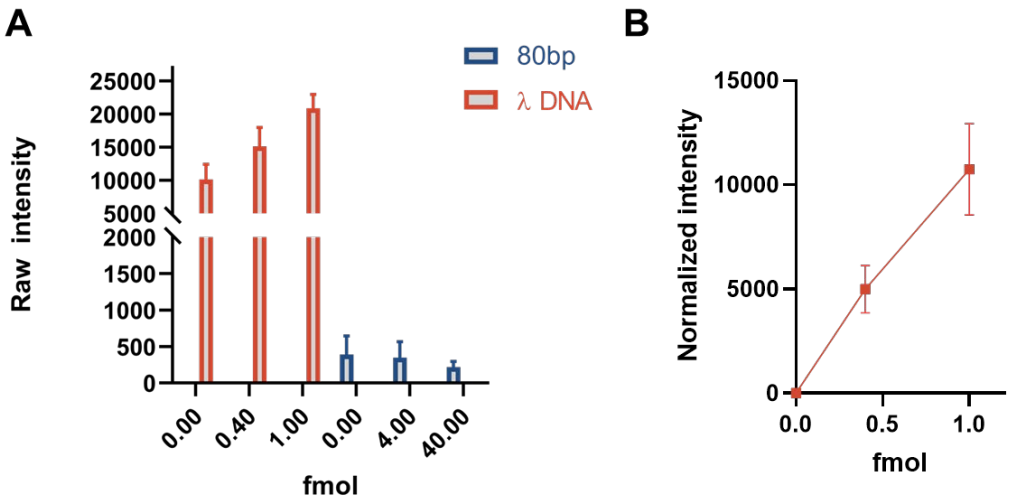

Figure 4.4. His-TFAM was detected using ELISA with DNA coating reagent. 80bp AP containing synthesized substrate or λ DNA was incubated with wtTFAM for 24hours, followed by DPC extraction as previously described. The extracted DPC concentration were measured using NanoDrop under nucleic acid mode for the DNA concentration and estimated the molar concentration by their size. λ DNA were more effectively coated onto the plate than the 80bp standard (**A**). Extracting the luminescent signal for λ DNA-DPC (**B**), with input 0 fmol, 0.4 fmol and 1.0 fmol, the duplicated data (each with 2 technical replicate) shows an increasing trend, providing the successful extraction of DPC.

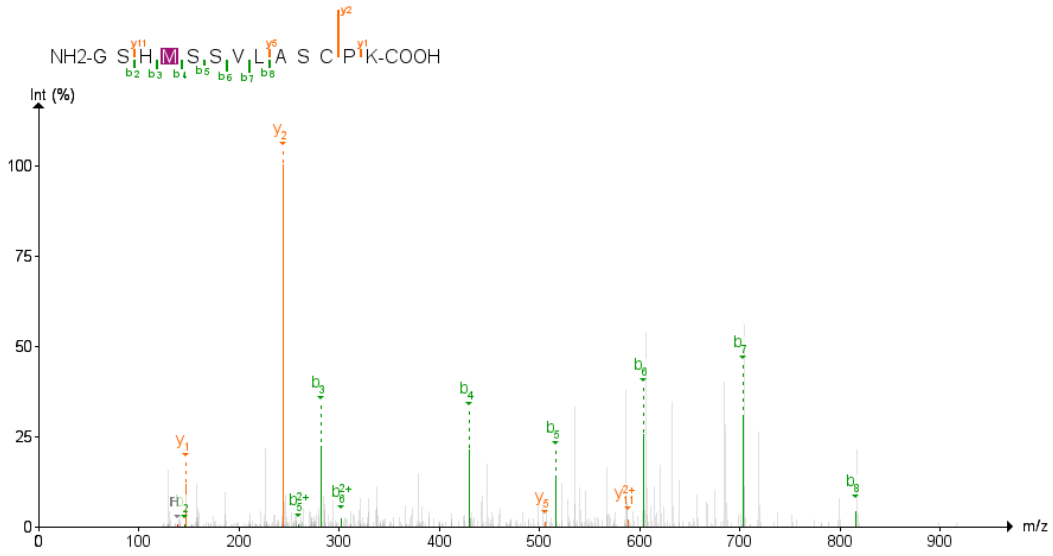

Figure 4.2. Representative MS2 analysis for DPC analysis. The purple highlighted M indicating an oxidation of M with mass adduct of 16. The 118 m/z mass adduct was at C, indicating a covalent crosslink at C position.

Table 4.1. Sequence of DNA substrate.

Substrate	Sequence
Synthetic oligo	5'FAM- GCGGTATGCACTTTTAACAdUTCACCCCCCAACTAAC 3'- CGCCATACGTGAAAATTGT—AAGTGGGGGGTTGATTG

Table 4.2. Observed peptides from reaction of TFAM with synthetic AP-DNA. Residues in red are residues covalently linked to AP site.

m/z	Charge	Crosslinked residue	Crosslinked peptide	mass adduct	Peak area	%
572.9771	3	K69	EQLPIFKAQNPDAK	118.0630	73300314	31.47
479.8955	3	C49	GSHM^{+16}SSVLASCPK	118.0630	159640136	68.53

References

(1) Kukat, C.; Wurm, C. A.; Spåhr, H.; Falkenberg, M.; Larsson, N. G.; Jakobs, S. Super-Resolution Microscopy Reveals That Mammalian Mitochondrial Nucleoids Have a Uniform Size and Frequently Contain a Single Copy of MtDNA. *Proc Natl Acad Sci U S A* 2011, *108* (33). DIO. 10.1073/pnas.1109263108.

(2) Gustafsson, C. M.; Falkenberg, M.; Larsson, N. G. Maintenance and Expression of Mammalian Mitochondrial DNA. *Annu Rev Biochem* 2016, *85*. DIO. 10.1146/annurev-biochem-060815-014402.

(3) Falkenberg, M.; Larsson, N. G.; Gustafsson, C. M. DNA Replication and Transcription in Mammalian Mitochondria. *Annual Review of Biochemistry*. 2007. DIO. 10.1146/annurev.biochem.76.060305.152028.

(4) Maekawa, H.; Inoue, T.; Ouchi, H.; Jao, T. M.; Inoue, R.; Nishi, H.; Fujii, R.; Ishidate, F.; Tanaka, T.; Tanaka, Y.; Hirokawa, N.; Nangaku, M.; Inagi, R. Mitochondrial Damage Causes Inflammation via CGAS-STING Signaling in Acute Kidney Injury. *Cell Rep* 2019, *29* (5). DIO. 10.1016/j.celrep.2019.09.050.

(5) Lu, T.; Zhang, Z.; Bi, Z.; Lan, T.; Zeng, H.; Liu, Y.; Mo, F.; Yang, J.; Chen, S.; He, X.; Hong, W.; Zhang, Z.; Pi, R.; Ren, W.; Tian, X.; Wei, Y.; Luo, M.; Wei, X. TFAM Deficiency in Dendritic Cells Leads to Mitochondrial Dysfunction and Enhanced Antitumor Immunity through CGAS-STING Pathway. *J Immunother Cancer* 2023, *11* (3). DIO. 10.1136/jitc-2022-005430.

(6) Xu, W.; Tang, J.; Zhao, L. DNA–Protein Cross-Links between Abasic DNA Damage and Mitochondrial Transcription Factor A (TFAM). *Nucleic Acids Res* 2023, *51* (1), 41–53. DIO. 10.1093/nar/gkac1214.

(7) Zhao, W.; Xu, W.; Tang, J.; Kaushik, S.; Chang, C.-E. A.; Zhao, L. Key Amino Acid Residues of Mitochondrial Transcription Factor A Synergize with Abasic (AP) Site Dynamics To Facilitate AP-Lyase Reactions. *ACS Chem Biol* 2023, *18* (5), 1168–1179. DIO. 10.1021/acschembio.3c00047.

(8) Zhao, W.; Hussen, A. S.; Freudenthal, B. D.; Suo, Z.; Zhao, L. Mitochondrial Transcription Factor A (TFAM) Has 5′-Deoxyribose Phosphate Lyase Activity in Vitro. *DNA Repair (Amst)* 2024, *137*, 103666. DIO. 10.1016/j.dnarep.2024.103666.

(9) Kojima, N.; Sugino, M.; Mikami, A.; Ohtsuka, E.; Komatsu, Y. Generation of an Abasic Site in an Oligonucleotide by Using Acid-Labile 1-Deaza-2′-Deoxyguanosine and Its Application to Postsynthetic Modification. *Org Lett* 2005, *7* (4). DIO. 10.1021/ol0474498.

(10) Xu, W.; Zhao, L. An Enzyme-Linked Immunosorbent Assay for the Detection of Mitochondrial DNA–Protein Cross-Links from Mammalian Cells. *DNA* 2022, *2* (4), 264–278. DIO. 10.3390/dna2040019.

(11) Cuppari, A.; Fernández-Millán, P.; Battistini, F.; Tarrés-Solé, A.; Lyonnais, S.; Iruela, G.; Ruiz-López, E.; Enciso, Y.; Rubio-Cosials, A.; Prohens, R.; Pons, M.; Alfonso, C.; Tóth, K.; Rivas, G.; Orozco, M.; Solà, M. DNA Specificities Modulate the Binding of Human Transcription Factor A to Mitochondrial DNA Control Region. *Nucleic Acids Res* 2019, *47* (12), 6519–6537. DIO. 10.1093/nar/gkz406.

(12) Liu, H.; Zhen, C.; Xie, J.; Luo, Z.; Zeng, L.; Zhao, G.; Lu, S.; Zhuang, H.; Fan, H.; Li, X.; Liu, Z.; Lin, S.; Jiang, H.; Chen, Y.; Cheng, J.; Cao, Z.; Dai, K.; Shi, J.; Wang, Z.; Hu, Y.; Meng, T.; Zhou, C.; Han, Z.; Huang, H.; Zhou, Q.; He, P.; Feng, D. TFAM Is an Autophagy Receptor That Limits Inflammation by Binding to Cytoplasmic Mitochondrial DNA. *Nat Cell Biol* 2024. DIO. 10.1038/s41556-024-01419-6.

(13) Andreeva, L.; Hiller, B.; Kostrewa, D.; Lässig, C.; De Oliveira Mann, C. C.; Jan Drexler, D.; Maiser, A.; Gaidt, M.; Leonhardt, H.; Hornung, V.; Hopfner, K. P. CGAS Senses Long and HMGB/TFAM-Bound U-Turn DNA by Forming Protein-DNA Ladders. *Nature* 2017, *549* (7672), 394–398. DIO. 10.1038/nature23890.